THESIS

Spiking neurons and device synchronization for spintronic neuromorphic computing

Cycle XXXVI

Dissertation with the aim of achieving a doctoral degree in Fundamental Physics at the Department of Mathematical and Computer Sciences, Physical Sciences and Earth Sciences, and at the Department of Science and Technology

of University of Messina and the Lebanese University

Coordinator:

Signature _____

Supervisors:

Prof. Giovanni Finocchio

Signature _____

Prof. Abbas Hamadeh

Signature

Ph.D student: Dr. Rayan Moukhader

Signature

Abstract

The main goal of this thesis is the achievement of further understanding on various hot topics related to Spintronics and neuromorphic computing.

Spintronics, also known as spin electronics, differs from traditional electronics in that, in addition to charge state, electron spins are used as a further degree of freedom. The connection between electron charge and spin admits changing the electronic transport by spins, and, on the contrary, to alter the magnetic properties by electron charges. Thus, nowadays, spin is fundamental for some of our technologies due to their interesting properties: nanometer dimension, low energy consumption, non-volatility, high scalability, and large speed.

Various spin textures and devices have emerged and were deeply studied for the evolution of spintronic applications. Here we can mention the magnetic skyrmions and vortices where both exhibit intriguing and novel phenomena due to their topologically non-trivial spin textures, making them attractive for applications in spintronic devices. Moreover, the transformation of these 2D solitons into the 3D space, results in 3D magnetic solitons specifically known as “hopfions”. Recent studies concerning the dynamics of hopfions showed its promise in the field of magnetic data storage, topological photonics, and novel magnetic materials for spintronics applications.

Alternatively, the non-volatility, high speed, and power efficiency of magnetic tunnel junctions, makes them primarily used as key components in magnetic memory applications. While both skyrmions and MTJs are important in spintronics, they serve different purposes and operate based on different principles. Skyrmions are topologically stable magnetic textures with potential applications in various spintronic devices, while MTJs are structures used primarily in magnetic memory and sensing applications.

On the other hand, Neuromorphic computing has emerged as an alternative for conventional computing based on Von-Neumann architecture that suffers from various bottlenecks. Neuromorphic computing is meant to efficiently deal with the massive amount of data and computations in ubiquitous automobiles and portable edge devices. Such systems are based on a set of artificial neural networks (ANNs) with the most bio-realistic third generation neural network known as, spiking neural network (SNN). Spiking Neural Networks are highly power-efficient and have competitive capabilities to deal with numerous cognitive tasks. Spintronic based neuromorphic computing is an emerging field, holding promises for future technology.

The main contributions of this thesis to the first topic have been about the different chiral spin textures characterized by a non-uniform distribution of the magnetization, including skyrmions and vortices. They have found a widespread range of applications because they can be easily nucleated, moved, and shifted by spin polarized current. The center of our attraction is the dynamics of these textures driven by Dzyaloshinskii-Moriya Interaction (DMI). We carried out a theoretical study based on micromagnetic simulations, in absence of thermal fluctuations. Our results show that under the influence of linear DMI gradients, Néel and Bloch-type skyrmions and radial vortex exhibit motion with finite skyrmion Hall

angle, while the circular vortex undergoes expulsion dynamics. We provided a deeper and crucial understanding of the stability and gradient-driven dynamics of magnetic solitons and paved the way for the design of alternative low-power sources of magnetization manipulation in the emerging field of 2d materials.

The second topic was about magnetic tunnel junction (MTJ) neuron, where MTJ is considered as a major spintronic device, composed of two ferromagnets separated by an insulating material. The designed MTJ neuron performs firing for spiking neural networks without the need of any resetting procedure. We leverage two physics, magnetism, and thermal effects, to obtain a bio-realistic spiking behavior equivalent to the Huxley-Hodgkin model of the neuron. Numerical simulations using experimental-based parameters demonstrate firing frequency in the MHz to GHz range under constant input at room temperature.

Acknowledgment

The work of the thesis was carried out between the University of Messina (Dept. of Mathematical and Computer Sciences, Physical Sciences and Earth Sciences) and the Lebanese University (University of Science and Technology). The acknowledgements go to everyone who has contributed in some way to the development of this work. I begin by thanking them for their warm welcome and for granting me the chance to prepare my thesis in very good condition.

I am so happy to have been a member of the Engineering Department, I send my great thanks to Prof. Bruno Azzerboni, director of the department, who has welcomed me warmly in his team. I would like to thank brightly my supervisor Prof. Giovanni Finocchio professor at University of Messina for his time he devoted to me, guidance, valuable advice, criticism, patience, encouragement when necessary, sharing with me his scientific experience, insight throughout the research and help whenever I consult him. I would also like to thank him for offering me the chance to integrate into the research domain in a pleasant atmosphere. I would especially like to thank him for his human qualities. He is such an excellent person, supervisor, and professor.

My special thanks go to the co-supervisors Dr. Riccardo Tomasello and Dr. Davi Rodrigues who were also responsible about my thesis work. They both struggled with me during this study, and were so patient, supportive, helpful, and friendly in giving me all the information that allowed me to do my job. Dr. Tomasello has helped me a lot in the domain of skyrmions and he has immense knowledge about this field. Moreover, Dr. Rodrigues provided me with insightful discussions and suggestions about the research concerning MTJ based neuromorphic device. He was the primary resource for getting my questions answered through my PhD journey.

I would like to express my deepest gratitude and thanks to all the petaspin team for their motivation, enthusiasm and immense knowledge. Their support has been invaluable on both academic and personal level, for which I am extremely grateful.

As for my supervisor in the Lebanese University, Prof. Abbass Hamedeh, I would like to express my deep respect and sincere gratitude. He offered his unreserved help and guidance throughout my graduate studies. He guided me through tough times and was always with me to check on my research progress. He had always trusted and encouraged me. Thank you for putting

me on the successful track and providing all the support at all levels. Also, I would like to express my warmest gratitude to him for suggesting this topic to me.

I thank them all for their patience, guidance, untiring work, involvement, and support from the initial to the final level which enabled me to develop a good understanding and realization of the subject. From deep in my heart, I'd like to say: "Thank you so much".

To all the doctors who helped get me to where I am today, thank you. Thanks to all my doctors to whom I owe what I have reached today.

Another great merit goes back to my family, my father looking proudly at me from heaven, my mother, my brothers Hassan and Hussein, and my husband Mohammad whom without their support and prayers I would not have achieved this great rank. I owe you my presence and achievements. Thanking you would not express the enormous amount of gratitude that I have towards you. I have experienced the most beautiful moments, memories that will stay engraved in my mind and my heart as ever I last. These moments, whether easy or hard, have taught me great lessons that will always push me forward through my social as well as practical life.

It was a remarkable journey where I have experienced the most beautiful moments, memories that will stay engraved in my mind and my heart as ever I last. These moments, whether easy or hard, have taught me great lessons that will always push me forward through my social as well as practical life.

Finally, the words of thanks are always difficult to express and remain helpless of describing my gratitude to all those people.

TABLE OF CONTENTS

Abstract 2

Acknowledgment 4

Table of Contents 6

List Of Abbreviations 10

List Of Symbols 12

List Of Figures 15

List Of Tables 22

Chapter 1: Introduction 23

1.1 Thesis Overview 24

Chapter 2: Fundemantuls of Micromagnetism 26

2.1 Introduction to Micromagnetism 27

2.1.1 Exchange Energy 28

2.1.2 Uniaxial Anisotropy Energy 29

2.1.3 Magnetostatic Energy 29

2.1.4 Zeman Energy 29

2.1.5 Thermal Energy 30

2.2 Equilibrium and Dynamical Equations 30

2.2.1 Dynamical equation 31

2.2.2 Spin-Transfer Torque 32

2.2.3 Voltage Controlled Magnetocrystalline Anisotropy 35

2.3 Spin-Orbit Interactions 35

2.3.1 Spin-Hall Effect 35

2.3.2 Dzyaloshinskii-Moriya Interaction (DMI) 36

2.4 Numerical Micromagnetism 38

2.4.1 Software Packages 39

Chapter 3:Magnetic Skyrmions 41

3.1 Introduction to Magnetic Skyrmions 42

3.1.1 Skyrmion Based Technology 43

3.2 Skyrmion Properties & Stabilization 45

3.2.1 Topology and Skyrmion Number 45

3.2.2 Skyrmion Configuration 45
3.2.3 Approaches for Skyrmion Stabilization 48
3.3 Manipulation of Magnetic Skyrmions Under DMI Gradient 48
3.3.1 Modeling and Sampling 48
3.3.2 Stability Results 51
3.3.3 Dynamics Results 52
3.4 From Skyrmions to Hopfions 53
3.4.1 Introduction to Hopfions 54
3.4.2 Topology and Hopf Number 56
3.4.3 Modeling and Sampling 56
3.4.4 Dynamics Results 58
3.5 Conclusion 60
Chapter 4:Magnetic Vortices 61
4.1 Introduction to Magnetic Vortices 62
4.2 Manipulation of Magnetic Vortices Under DMI Gradient 63
4.2.1 Modelling and Sampling 63
4.2.2 Stability Results 64
4.2.3 Dynamics Results 65
4.2.4 Experimental Generation of DMI Gradients 69
4.3 Conclusion 70
Chapter 5:Magnetic Tunnel Junction 71
5.1 Introduction to Magnetic Tunnel Junctions 72
5.2 MTJ Parameters 73
5.2.1 Tunneling Magnetoresistance 74
5.2.2 Switching Current Ic 76
5.2.3 Thermal Stability 77
5.3 MTJ Switching Approaches 78
5.3.1 Field Induced Magnetic Switching (FIMS) 78
5.3.2 Thermally Assisted Switching 79
5.3.3 Spin Transfer Torque (STT) Switching 80
5.3.4 Spin Hall Effect (SHE) Switching 81
5.4 MTJ Based Devices 81
5.4.1 Magnetoresistive Random Access Memory 81

5.4.2 MTJ Based Spin Logic 82
5.4.3 MTJ Based Neuromorphic Computing 83
5.5 Conclusion 85
Chapter 6: Neuromorphic Computing and Spiking Neural Network 86
6.1 The principles of neuromorphic computing 87
6.1.1 Early Networks and Development. 88
6.1.2 Neural Network Architecture 89
6.2 Spiking Neural Network 90
6.3 Dynamics of a Biological Neuron 92
6.4 Models of Single Neurons 94
6.4.1 Leaky Integrate-and-Fire Model 94
6.4.2 Hodgkin-Huxley Model 97
6.5 Neural Coding 101
6.5.1 Rate vs Temporal Coding 101
6.5.2 Population Coding 103
6.6 Noise in Spiking Neuron Models 103
6.7 Supervised and Unsupervised Learning in SNN 104
6.7.1 Supervised Learning 104
6.7.2 Unsupervised Learning 105
6.8 Synaptic Plasticity 107
6.8.1 Mathematical Formulation of Hebb's Rule 107
6.8.2 Spike-Time Dependent Plasticity 108
Chapter 7:MTJ-Based Synapse 111
7.1 Introduction 112
7.2 Device and Model 113
7.2.1 Device Properties 113
7.2.2 Micromagnetic Model 116
7.3 Results 117
7.3.1 Resistance and Temperature Relation 117
7.3.2 Current-Controlled Frequency 118
7.3.3 Emulating LIF Neuron 119
7.4 Analogy between H-H & LLG Models 120
7.5 Variation of Current 123

7.6 Designing an Unsupervised SNN 123
7.7 Summary 124
Chapter 8:Journal Articles 126
8.1 Published Articles 126
8.2 Submitted Articles 126
List of References 128

List Of Abbreviations

CMOS	Complementary Metal transistors Oxide Semiconductor
MTJ	Magnetic Tunnel Junction
STT	Spin Transfer Torque
DMI	Dzyaloshinskii–Moriya Interaction
SNN	Spiking Neural Network
LL	Landau-Lifshitz
LLG	Landau-Lifshitz-Gilbert
IP	In-Plane
OOP	Out-Of-Plane
VCMA	Voltage Controlled Magnetocrystalline Anisotropy;
SOT	Spin-Orbit Torque
SOC	Spin-Orbit Coupling
SHE	Spin-Hall Effect
AHE	Anomalous Hall Effect
HM	Heavy Metal
FM	Ferromagnet
b-DMI	Bulk Dzyaloshinskii-Moriya Interaction;
i-DMI	Interfacial Dzyaloshinskii-Moriya Interaction;
BC	Boundary Conditions
SAF	synthetic antiferromagnet
CW	Clockwise
CCW	Counterclockwise
RKKY	Ruderman-Kittel-Kasuya-Yosida
IC	Integrated circuit

FL	Ferromagnetic Layer
PL	Pinned Layer
P	Parallel
AP	Anti-Parallel
MRAM	Magnetic Random-Access Memory
TMR	Tunnel Magnetoresistance
FIMS	Field Induced Magnetic Switching
TAS	Thermally Assisted Switching
ANN	Artificial Neural Network
STDP	Spike Time Dependent Plasticity
LIF	Leaky Integrate and Fire
HH	Hodgkin Huxley
RBF	Radial Basis Function
BP	Back-Propagation
LTP	Long-Term Potentiation
LTD	Tong-Term Depression
PMA	Perpendicular Magnetic Anisotropy

List Of Symbols

$\mathbf{r}$	Position Vector
$\mathbf{M}$	Magnetization
M_s	Saturation Magnetization
μ_i	Magnetic Momenta
$\mathbf{m}$	Normalized Magnetization Vector
E_{ij}	Exchange Energy
J_{ij}	Exchange Integral
m_x	x-component of the normalized magnetization
m_y	y-component of the normalized magnetization
m_z	z-component of the normalized magnetization
A	Exchange Constant
u_k	Unit vector of the magnetization easy axis
$\mathbf{H}_m$	Magnetostatic field
μ_0	Vacuum permeability
N_x	x-axis shape-dependent demagnetizing factor
N_y	y-axis shape-dependent demagnetizing factor
N_z	z-axis shape-dependent demagnetizing factor
ε_{ext}	External magnetic field energy density
H_{ext}	External magnetic field
ε_{tot}	Total energy density of a ferromagnetic body
$\mathbf{H_{eff}}$	Effective field
h_{eff}	Normalized effective field
γ	Gyromagnetic ratio
α	Gilbert damping
g	Landé factor
e	Electron charge
m_e	Electron Mass
μ_B	Bohr magneton
τ_{oop}	STT in OOP device
j_{FE-oop}	Perpendicular current density
t_{FL}	Thickness of free layer
$\varepsilon\ (\mathrm{m}, \mathrm{m_p})$	Polarization Function
$\varepsilon_{MTJ}(\mathrm{m}, \mathrm{m_p})$	Polarization function for MTJ
η	Spin polarization factor of oop device
q(V)	Out-of-plane torque
τ_{IP}^{a}	Adiabatic torque for IP device
τ_{IP}^{na}	Non-adiabatic torque for IP device
P	Spin polarization factor of IP device
$J_{FE\text{-}ip}$	Current density of IP device
β	Non-adiabatic parameters
J_c	Charge current
τ_{SHE}	SHE torque
θ_{SH}	Spin-Hall angle

j_{HM}	Charge current density through a HM
j_s	Spin current
r_{ij}	Distance between two spins
ε_{bDMI}	Bulk DMI energy density
ε_{iDMI}	Interfacial DMI energy density
D	DMI constant
h_{bDMI}	Dimensionless bulk DMI field
h_{iDMI}	Dimensionless interfacial DMI field
ξ	DMI characteristic length
$\mathbf{n}$	Normal unit vector
N_{sk}	Skyrmion Number
$\mathbf{f}$	Azimuthal angle
R	Radial Distance
w	Skyrmion's vorticity
g	Skyrmion Helicity
$h_{ex,i}^{inter}$	RKKY interaction
A^{ex}	Exchange coupling factor
t_{NM}	Non-magnetic layer thickness
t_{FM}	Ferromagnetic layer thickness
K_u	Uniaxial Anisotropy constant
m(x|X(t),Y(t))	Magnetization of skyrmion core
X(t)	Position of the soliton core along x
Y(t)	Position of the soliton core along y
V(t)	Velocity of the skyrmion
$\overleftrightarrow{G}$	Gyrotropic tensor
$\overleftrightarrow{D}$	Viscoity tensor
Q	Topological Charge
ε_{ijk}	Antisymmetric tensor
E	Total Energy
D_c	Critical DMI constant
p	Polarity
c	Chirality
d	Diameter
$\mathbf{h}_{bound}$	Effective field due to boundary effects
TMR	Tunnel magnetoresistance ratio
R_{AP}	Electrical resistance in the anti-parallel state
R_P	Electric resistance in the parallel state
P_i	Spin polarization of i-th ferromagnetic layer
I_{c0}	Critical switching current
k_B	Boltzmann constant
T	Temperature
Δ	Thermal stability factor
V	MTJ cell volume
I(t)	Current in RC circuit
I_R	Current through resistor
I_C	Current through capacitor

$u(t)$	Membrane potential of a neuron
u_{rest}	Resting potential
τ_m	Time constant
I_{ext}	External pulse through a neuron
E_{Na}, E_K, E_L	Reversal potentials of Na, K, and L ion channels

List of Figures

Chapter 2

Figure 2.1 Scales in micromagnetism. (a) Atomic scale representation of individual magnetic moments m_I. (b) Micromagnetic scale representation of the magnetization vector M defining as the sum of all magnetic moments m_I inside the volume dV : $M = \frac{1}{dV} \sum_{I=1}^{N} m_I$. 29

Figure 2.2 Schematic representation of the magnetization M in light red according the LLGS equation. (a) Precession term: The magnetization M processes around the effective field H_{eff} following a circular trajectory of constant energy without damping effect. (b) Precession, and damping: The damping causes dissipation of the energy, and consequently the magnetization spirals back to the static equilibrium position. (c) Precession, damping and Spin-Transfer Torque: The STT acts as a source of energy which fully compensates for the damping. Therefore, energy is conserved, and the magnetization processes. 33

Figure 2.3 A simplified illustration of spin transfer torque process, FM_1 and FM_2 refers to ferromagnetic film with magnetization M_1 and M_2 respectively. The thick magnetic layer is used to produce a polarized electric current which in turn produces torque on M_2. 33

Figure 2.4 Schematic picture of the FM/HM bilayer, the charge current (J_C) entering the heavy metal induces the Spin Hall Effect (SHE), the opposite spin accumulations generate transverse spin current (J_S) on the FM/HM interface. 37

Figure 2.5 Sketch of Bulk DMI, and Interfacial DMI. The resulting bulk and interfacial DMI vector point perpendicular to the triangle consists of two magnetic atoms and an atom with large SOC [53]. 38

Chapter 3

Figure 3.1 Four different scenarios for the design of a skyrmion racetrack memory. (A), Néel skyrmion motion driven by the STT. (B), Néel skyrmion motion driven by the SHE. (C), Bloch skyrmion motion driven by the STT. (D), Bloch skyrmion motion driven by the SHE. The four insets show the spatial distribution of the Néel and Bloch skyrmion, where the background colors refer to the z-component of the magnetization (blue negative, red positive), while the arrows are related to the in-plane components of the magnetization. The current flows along the x-direction. The skyrmion moves along the x-direction in the scenarios A, C, and D and along the y-direction in the scenario B. 43

Figure 3.2 a) Schematic drawing of skyrmion-based artificial synapse, illustrating, Néel skyrmions in thin films mapped onto spheres and are shown in three-dimensional space. The red and blue colored arrows represent magnetic moments pointing +z and -z directions within skyrmions,

respectively. The synaptic weights are proportional to the number of skyrmions, which is modulated by the electric current-controlled accumulation and dissipation of them. (b), The measured Hall resistivity change and calculated skyrmion number as a function of injected pulse number. Note that red and blue symbols and colored areas correspond to resistivity changes during potentiation and depression, respectively. Green symbols are used to indicate the number of skyrmions. Enclosed electrical pulses indicate the direction of charge current pulse, opposite to the direction of electron flow. Error bars denote the standard deviation of the resistivity measurements at each state. (c), Sequential STXM images showing skyrmion populations after injecting unipolar current pulses along the track, during potentiation and depression, respectively, and each image number, #1-#16, corresponds to each resistivity state indicated in (b). 44

Figure 3.3 Illustration of magnetic skyrmions described by the skyrmion number N_{SK}, vorticity and helicity. The arrow denotes the spin direction while the color denotes the out-of-plane spin value, where red is out of plane, white is IP and blue is into the plane. Adapted from [121]. 47

Figure 3.4 Magnetization distribution of a (a) Bloch skyrmion, (b) Néel skyrmion. The color bar denotes the out-of-plane magnetization component m_z: red positive, white zero, and blue negative. 48

Figure 3.5 3D sketch of the 100 nm × 100 nm square sampled SAF multilayer under investigation, where it is composed of two ferromagnets (upper FM & lower FM) separated by a non-magnetic layer. On the left snapshots representing examples of the spatial distribution of the magnetization for SAF Néel and Bloch skyrmions in the upper and lower FMs respectively.. 49

Figure 3.6 Equilibrium configurations of the magnetization of the 2D CrI_3 material as a function of DMI constant |D| at zero external field with the initial configuration being (a) Néel skyrmion, and (b) Bloch skyrmion. The colors refer to the z-component of magnetization (blue negative, red positive). 51

Figure 3.7 Micromagnetic simulations results of the (a) Néel skyrmion trajectory under a linear iDMI gradient ($0.59\ mJ/m^2 \leq D \leq 0.78\ mJ/m^2$, see **Table 3.1**), and (b) Bloch skyrmion trajectory under a linear bDMI gradient ($0.60\ mJ/m^2 \leq D \leq 0.77\ mJ/m^2$ directed along the positive x-direction as shown in green arrow in a single CrI3 layer as a function of different damping coefficients. (c) – (d) Top and bottom layer of the SAF CrI_3, respectively, where the straight trajectory of the skyrmion is also indicated. The color bar denotes the out-of-plane magnetization component m_z: red positive, white zero, and blue negative. 53

Figure 3.8 Transition from a (a) skyrmion in the x-y plane to a (b) hopfion in the x-y-z space by transforming the magnetization configuration from a

localized spin texture with a circular core (skyrmion) to a twisted, three-dimensional structure with a central vortex-like core (hopfion). 55
Figure 3.9 Illustration of hopfion with different Hopf number, H=1, H=2, H=3. 56
Figure 3.10 Illustration of the 360 nm × 64 nm rectangular strip stack composed of two capping layers characterized by high PMA each with thickness T_{PMA}, sandwiching a FeGe layer with thickness T_{FeGe}. On the left snapshots representing examples of the spatial distribution of the uniform magnetization in the external layers and a Néel hopfion state in bulk. ... 57
Figure 3.11 (a) Trajectory of Néel hopfion driven by STT during a period of 50 ns, along the x-y plane (upper panel) and the x-z plane (lower panel). (b) Current density J dependence of the longitudinal velocity $\mathbf{v_x}$ of the Néel hopfion. The red circles are numerical results for STT-driven motion. The solid line is theoretical prediction. 60
Figure 3.12 (a) Micromagnetic simulations results of the equilibrium configurations of the magnetization as a function of |D|. (b) Trajectory of Néel hopfion driven by DMI gradient for 50 ns, along the x-y plane (upper panel) and the x-z plane (lower panel). (c) Velocity $\mathbf{v_x}$ of the Néel hopfion under the influence of DMI constant (D (J/m^2)).Numerical results (red circles), coincides with theoretical predictions (black line). 61

Chapter 4

Figure 4.1 Spatial distribution of magnetization for different types of vortices with positive (top) and negative (bottom) polarities. (a) Counterclockwise (CCW) circular vortex. (b) Clockwise (CW) circular vortex. (c) Radial vortex. A color scale linked to the out-of-plane component of the magnetization is also shown (red positive, blue negative). 63
Figure 4.2 Micromagnetic simulations results of the equilibrium configurations of the magnetization as a function of |D| in (a) – (f) CoFeB and (g)-(l) CrI_3 rectangular strips. 65
Figure 4.3 Micromagnetic simulations results of radial vortex trajectories under a linear iDMI gradient. In (a) and (b), a single 1500 nm × 250 nm FM rectangular sample under the effect of different damping coefficients in CoFeB and CrI_3, respectively, (c) and (d) in top layers and (e) and (f) in the bottom layers of the SAF composed of CoFeB and CrI_3, respectively..... 66
Figure 4.4 Motion of the radial vortex core in an iDMI gradient as obtained from the Thiele's equation. We considered here the Thiele description given by **Eqs. (3.6-3.7)**, for rescaled units for a qualitative description to be compared with the micromagnetic simulations in **Fig. 4.3(a)** away from the border. In (a)-(b), we show the motion for different values of rescaled Gilbert damping and iDMI gradient, respectively. We considered a_G and c_D as renormalized values for numerical simulations for a qualitative comparison. 68

FIGURE 4.5 MICROMAGNETIC SIMULATIONS RESULTS OF THE TIME EVOLUTION OF THE SPATIAL DISTRIBUTION OF THE MAGNETIZATION FOR A CIRCULAR VORTEX UNDER THE INFLUENCE OF THE LINEAR IDMI GRADIENT IN A COFEB CIRCULAR SAMPLE. 69

CHAPTER 5

FIGURE 5.1 (A), (B) FRONT VIEW OF MTJ SWITCHING FROM P STATE TO AP STATE, AND VICE VERSA FOR IMTJ AND PMTJ, RESPECTIVELY. (C) AN ENERGY BARRIER E_B SEPARATES P AND AP STATES OF PMTJ, WHERE THE BARRIER HEIGHT DECIDES THE STABILITY OF STABLE STATES OF PMTJ. 73

FIGURE 5 2 TMR RATIO PLOTTED AT ROOM TEMPERATURE FOR VARIOUS MTJ STRUCTURES DEVELOPED USING BOTH ALO_X AND MGO BARRIER WITH A DIFFERENT FL AND PL. SIGNIFICANT GROWTH CAN BE OBSERVED IN THE TMR RATIO OF MGO-BASED MTJ (RED CIRCLES) COMPARED TO ALO_X (BLUE SQUARES) DURING THE YEAR 2001 TO 2008 [186]. 75

FIGURE 5.3 BAND DIAGRAMS FOR UP AND DOWN SPINS WHEN MTJ IS IN (A) PARALLEL CONFIGURATION AND IN (B) ANTI-PARALLEL CONFIGURATION, TO ILLUSTRATE EFFECT OF TUNNELING MAGNETORESISTANCE. 76

FIGURE 5.4 VARIATION OF THERMAL STABILITY (Δ) FOR AN MTJ FOR THREE DIFFERENT THICKNESSES OF MGO BARRIER, (A) VERSUS TEMPERATURE (K), MAGNETIC ANISOTROPY (J/M^3),AND MTJ SIZE (M^3)..... 77

FIGURE 5.5 ILLUSTRATION TO UNDERSTAND THE FIMS SWITCHING MECHANISM IN IMTJ, SITUATED BETWEEN DL AND BL, RESPECTIVELY. 78

FIGURE 5.6 ILLUSTRATION OF TAS SWITCHING MECHANISM IN PMTJ, WHICH IS PRESENT BETWEEN TWO ANTIFERROMAGNETIC LAYERS NAMED AF_1 AND AF_2. 79

FIGURE 5.7 STT SWITCHING MECHANISM OF AN MTJ DEMONSTRATES TWO DIFFERENT STATES P AND AP. 80

FIGURE 5.8 COMPARISON OF MEMORY CELL ARCHITECTURE BETWEEN (A) CONVENTIONAL FIELD SWITCHING MRAM, AND (B) SPIN TRANSFER TORQUE MRAM..... 82

FIGURE 5.9 FULL SCHEMATIC OF SPIN-MTJ-BASED NON-VOLATILE FLIP-FLOP. 83

FIGURE 5.10 (A) STOCHASTIC SPIKING NEURAL NETWORK USED FOR DIGIT RECOGNITION. INPUT SPIKE TRAINS ARE RECEIVED BY ALL THE STOCHASTIC NEURONS (CONNECTIONS SHOWN FOR ONLY ONE NEURON). THE INHIBITORY NEURON PREVENTS THE NEURONS FROM SPIKING IN CASE AN EXCITATORY NEURON SPIKES. (B) CORRESPONDING IMPLEMENTATION IN A CROSSBAR ARRAY FASHION. PROGRAMMABLE RESISTIVE SYNAPSES ARE PRESENT AT EACH CROSS-POINT. INPUT VOLTAGES ARE APPLIED AT EACH ROW AND THE NEURONS RECEIVE INPUT SYNAPTIC CURRENT WHICH IS THE WEIGHTED SUMMATION OF THE INPUT VOLTAGES. (C) A NETWORK OF 9 EXCITATORY NEURONS WERE USED FOR THE RECOGNITION PURPOSE. THE SYNAPSE WEIGHTS WERE RANDOMLY INITIALIZED. 784 INPUT NEURONS (28 X 28 IMAGES) ARE RATE ENCODED BY ENSURING THAT THE SPIKE FREQUENCY IS DIRECTLY PROPORTIONAL TO THE PIXEL INTENSITY. AFTER LEARNING THE NEURONS RESPOND SELECTIVELY TO EACH INPUT IMAGE. (D) FOR TESTING THE BEHAVIOR OF THE NETWORK AFTER LEARNING HAS BEEN ACCOMPLISHED, STDP AND HOMEOSTASIS WERE TURNED OFF. THE NEURON STOCHASTICALLY SPIKES

THE MAXIMUM FOR THE CLASS WHICH IT HAS LEARNT WHILE THE OTHERS REMAIN MOSTLY SILENT. A COMMON LATERAL INHIBITORY SIGNAL DURING TESTING RESULTS IN SPARSE SPIKING EVENTS. 84

FIGURE 5.11 STM AND LTM TRANSITION EXHIBITED IN A 34 × 43 MTJ MEMORY ARRAY. THE INPUT STIMULUS WAS A BINARY IMAGE OF THE PURDUE UNIVERSITY LOGO WHERE A SET OF 5 PULSES (EACH OF MAGNITUDE 100μA AND 1NS IN DURATION) WAS APPLIED FOR EACH ON PIXEL. WHILE THE ARRAY TRANSITIONED TO LTM PROGRESSIVELY FOR FREQUENT STIMULATIONS AT AN INTERVAL OF T = 2.5NS, IT "FORGOT" THE INPUT PATTERN FOR STIMULATION FOR A TIME INTERVAL OF T = 7.5NS [22]. 85

CHAPTER 6

FIGURE 6.1 COMPARISON BETWEEN (A) VON-NEUMANN AND (B) NEURAL NETWORK COMPUTING ARCHITECTURES. 87

FIGURE 6.2 SCHEMATIC REPRESENTATION OF A PERCEPTRON. IT TAKES A WEIGHTED SUM OF INPUT AND RETURNS '0' IF THE RESULT IS BELOW THRESHOLD AND '1' OTHERWISE... 89

FIGURE 6.3 SCHEMATIC REPRESENTATION OF THE NEURAL NETWORK'S ARCHITECTURES. (A) A SINGLE HIDDEN LAYER NEURAL NETWORK. (B) A FOUR-LAYER NETWORK WITH TWO HIDDEN LAYERS. 90

FIGURE 6.4 (A) THE SYNAPSES ARE PRESENT AT THE JUNCTION OF AXONAL TERMINAL AND DENDRITES OF THE BIOLOGICAL NEURONS. SOME OF THE KNOWN NEUROTRANSMITTER SIGNALING MECHANISMS ARE ILLUSTRATED [216]. (B) APPROXIMATE PLOT OF A TYPICAL ACTION POTENTIAL SHOWS ITS VARIOUS PHASES. THE MEMBRANE POTENTIAL STARTS OUT AT APPROXIMATELY −70 MV AT TIME ZERO. A STIMULUS IS APPLIED AT TIME = 1 MS, WHICH RAISES THE MEMBRANE POTENTIAL ABOVE −55 MV (THE THRESHOLD POTENTIAL). AFTER THE STIMULUS IS APPLIED, THE MEMBRANE POTENTIAL RAPIDLY RISES TO A PEAK POTENTIAL OF +40 MV AT TIME = 2 MS. JUST AS QUICKLY, THE POTENTIAL THEN DROPS AND OVERSHOOTS TO −90 MV AT TIME = 3 MS, AND FINALLY THE RESTING POTENTIAL OF −70 MV IS REESTABLISHED AT TIME = 5 MS. 93

FIGURE 6.5 SCHEMATIC DIAGRAM OF THE INTEGRATE-AND-FIRE MODEL. THE BASIC CIRCUIT IS THE MODULE INSIDE THE DASHED CIRCLE ON THE RIGHT-HAND SIDE. A CURRENT I(T) CHARGE THE RC CIRCUIT. THE VOLTAGE U(T) ACROSS THE CAPACITANCE (POINTS) IS COMPARED TO A THRESHOLD Θ. IF U(T) = Θ AT TIME TI(F) AN OUTPUT PULSE Δ(T − TI(F)) IS GENERATED. LEFT PART: A PRESYNAPTIC SPIKE Δ (T − TJ(F)) IS LOW-PASS FILTERED AT THE SYNAPSE AND GENERATES AN INPUT CURRENT PULSE A (T − TJ(F)) [218]. 95

FIGURE 6.6 MEMBRANE POTENTIAL OF A LIF NEURON AT (A) CONSTANT CURRENT $I \leq 0.5 mA/cm2$, WHERE NO SPIKES ARE FIRED. (B) FOR INCREASING CURRENT THE NUMBER OF FIRED SPIKES INCREASE, AS (A) SHOWS 7 SPIKES FOR $I = 0.7$ MA/CM2, AND 24 SPIKES FOR $I = 1.5$ MA/CM2. 96

FIGURE 6.7 (A) THE MEMBRANE POTENTIAL VERSUS TIME UNDER THE INFLUENCE OF AN INCREASING CURRENT $0 \leq I \leq 3$ MA/CM2. (B) THE VARIATION OF THE INTERSPIKE INTERVAL BETWEEN CONSECUTIVE ACTION POTENTIALS AS FUNCTION OF CURRENT AND STIMULUS TIME. 97

FIGURE 6.8 SCHEMATIC DIAGRAM FOR THE HODGKIN-HUXLEY MODEL [218]. 97

FIGURE 6 9 (A) THREE DIFFERENT PULSES ARE CONSIDERED FOR A SIMULATION TIME OF 50 NS, VARIATION OF ACTION POTENTIAL, GATING VARIABLES N, M AND H , AND CONDUCTANCE FOR (B) CONSTANT CURRENT I =10 MA/CM2, (C) RECTANGULAR PULSE BETWEEN 10 MS < T < 30 MS, (C) AND FOR AN INCREASING CURRENT WITH SLOPE OF 0.5. 100

FIGURE 6.10 (A) FOUR SPIKES EMITTED BY H-H NEURON AT CONSTANT CURRENT. THESE SPIKES ARE ENCODED BASED ON TWO PARADIGMS, (B) RATE CODING AND, (C) TEMPORAL CODING. 102

FIGURE 6.11 (A) A NOISY PULSE CURRENT IS INJECTED INTO, (B) A LIF NEURON FIRING A NOISY SPIKE WITH A DELAYED FIRING TIME. (C) A H-H NEURON SHOWS A LITTLE DISTURBANCE IN THE REFRACTORY PERIOD OF THE ACTION POTENTIAL. 104

FIGURE 6.12 UNSUPERVISED LEARNING RULE IN SNN PROPOSED IN [231] 106

FIGURE 6.13 ARCHITECTURE OF THE DIEHEL & COOK NETWORK [235]. 107

FIGURE 6.14 REPRESENTATION OF THE SPIKE-TIMING-DEPENDENT PLASTICITY (STDP) LEARNING RULE. THE STRENGTH OF THE CONNECTION (SYNAPTIC WEIGHT) IS ADJUSTED BASED ON THE TIMING OF PRE- AND POST-SYNAPTIC SPIKES. FOR $\Delta T > 0$, ΔW IS POSITIVE, INDICATING AN INCREASE IN SYNAPTIC WEIGHT, WHEREAS, FOR $\Delta T < 0$, ΔW IS NEGATIVE, INDICATING A DECREASE IN SYNAPTIC WEIGHT..... 109

CHAPTER 7

FIGURE 7.1 AN MTJ IMPLEMENTATION OF BIO-REALISTIC FIRING BEHAVIOR. (A) ON THE LEFT WE SHOW A SKETCH OF THE DEVICE CONCEPT OF THE PROPOSED MTJ SYNAPTIC DEVICE AND ON THE RIGHT A SKETCH OF A BIOLOGICAL NEURON. BOTH RECEIVE THE INPUT IN TERMS OF CURRENTS AND PRODUCE AN OUTPUT IN TERMS OF VOLTAGE VARIATION. IN THE SPINTRONIC DEVICE, THE POTENTIAL VARIATION IS DUE TO CHANGES IN RESISTANCE PRODUCED BY THE INPUT CURRENT AND THERMAL EFFECTS. IN THE NEURON, THE POTENTIAL VARIATION IS DUE TO THE SODIUM (NA^+), POTASSIUM (K^+), AND LEAKAGE CURRENTS. (B) AND (C) COMPARE THE RESISTANCE VARIATION OF THE PROPOSED MTJ DEVICE WITH THE POTENTIAL SPIKING IN A BIOLOGICAL NEURON ACCORDING TO THE HUXLEY-HODGKIN MODEL. IN (B) FROM TOP TO BOTTOM WE SHOW: THE SPIKES IN THE RESISTANCE THROUGH THE DEVICE; THE DYNAMICS OF THE MAGNETIZATION COMPONENTS; THE TEMPERATURE VARIATION OF THE DEVICE. (C) AN EXAMPLE OF A NUMERICAL SIMULATION OF THE DYNAMICS OF A H-H NEURON. IT CAN BE OBSERVED 6 THAT THE BEHAVIOR OF A SHARP FIRING SIGNAL FOLLOWED BY A REFRACTORY PERIOD IS A COMMON FEATURE IN BOTH MODELS..... 114

FIGURE 7.2 (A) AND (B) SHOW THE DEPENDENCE OF THE AVERAGE NORMALIZED RESISTANCE AND TEMPERATURE AS A FUNCTION OF THE APPLIED CURRENT DENSITY, RESPECTIVELY. ON (A) WE IDENTIFY THREE REGIONS WHERE: (I) THE MAGNETIZATION IS STRONGLY BIASED TOWARDS THE EASY AXIS IN THE FREE LAYER (NPMA), (II) THERE IS AN AUTO-OSCILLATION AROUND THE EASY-AXIS OF THE FREE LAYER (NPMA), (III) THE MAGNETIZATION IS STRONGLY BIASED TOWARDS THE DIRECTION OF THE MAGNETIZATION IN THE POLARIZER (P). 118

FIGURE 7.3 (A) FREQUENCY OF NEURON FIRING AS A FUNCTION OF THE APPLIED CURRENT DENSITY. (B) AND (C) SHOW THE TIME DOMAIN BEHAVIOR OF THE RESISTANCE (TOP),

MAGNETIZATION COMPONENTS AND TEMPERATURE (BOTTOM) FOR LOW ($2 \times 1010 A/m^2$) AND HIGH ($2.4 \times 1010 A/m^2$) CURRENT DENSITY RESPECTIVELY. 119

FIGURE 7.4 (A) DIFFERENCE BETWEEN THE H-H MODEL AND THE LIF MODEL. IN THE LIF MODEL, WE CONSIDER PULSES OF AMPLITUDE ΔI AND PERIOD ΔT. (B) EVOLUTION OF THE DEVICE PROPERTIES UNDER THE PRESENCE OF CURRENT PULSES. FROM TOP TO BOTTOM PANELS, WE SHOW THE NORMALIZED RESISTANCE, THE EVOLUTION OF THE MAGNETIZATION COMPONENTS, THE PROFILE OF THE APPLIED CURRENT AND THE TEMPERATURE OF THE DEVICE. (C) SHOWS THE TIME BETWEEN THE FIRST PULSE AND THE FIRST SYNAPSE. DIFFERENT COLORS REPRESENT DIFFERENT PULSE SIZES, WHILE THE X-AXIS REPRESENT THE LOWEST CURRENT VALUE IN THE PULSE. TO INCLUDE THERMAL INDUCED STOCHASTICITY, WE SIMULATED EACH PULSE AMPLITUDE AND SIZE FIVE TIMES. (D) THE TIME OF THE FIRST SYNAPSE FOR A CONSTANT CURRENT..... 120

FIGURE 7.5 BEHAVIOR OF MAGNETIZATION DYNAMICS FOR DIFFERENT CURRENTS AND INCLUDING THE FIELDLIKE TORQUE. MATERIAL PARAMETERS ARE THOSE GIVEN IN **TABLE 7.2**. 122

FIGURE 7.6 AN EXAMPLE OF SNN BUILT WITH THE PROPOSED MTJ DEVICE. (A) SHOWS THE BEHAVIOR OF AN SNN WITH 4 NEURONS. THE CURRENT OF THE TWO INPUT NEURONS IS SET AS CONSTANTS. FOR EACH MTJ WE SHOW THE BEHAVIOR OF THE RESISTANCE (UPPER PANEL) AND THE INPUT CURRENT (LOWER PANEL). THE INPUT CURRENTS OF THE OUTPUT NEURONS ARE GENERATED ACCORDING TO EQ. 11, WITH THE RESPECTIVE WEIGHTS W_{MN} SHOWN. (B) SHOWS THE TWO SETS CONSIDERED FOR VERIFYING THE LEARNING PROCESS AND (C) SHOWS A SKETCH OF THE FEED-FORWARD ALL-CONNECTED SNN. EACH PIXEL IS ASSOCIATED WITH A SINGLE INPUT NEURON. (D) SHOWS THE EVOLUTION OF THE WEIGHT MATRIX. STARTING FROM A RANDOM DISTRIBUTION OF WEIGHTS, AFTER THE TRAINING PROCESS, EACH FIGURE CAN BE REPRESENTED BY A SINGLE OUTPUT NEURON WHICH HAS THE HIGHEST FREQUENCY. 124

List of Tables

TABLE 3.1 MICROMAGNETIC PARAMETERS OF COFEB AND CrI_3 USED FOR SIMULATING NÉEL AND BLOCH SKYRMIONS, FOR BOTH SQUARE AND CIRCULAR GEOMETRIES..... 50

TABLE 4.1 MICROMAGNETIC PARAMETERS OF COFEB [128] AND CrI_3 USED FOR SIMULATING RADIAL AND CIRCULAR VORTICES [129]. THE VALUE OF THE ANISOTROPY OF CrI_3 CAN BE TUNED AS SHOWN IN FIG. 1(C) OF REF. [162]..... 64

TABLE 6.1 COMPARISON OF THE SNN AND OTHER MACHINE LEARNING TECHNIQUES [206]. 92

TABLE 6.2 THE PARAMETERS OF THE HODGKIN-HUXLEY EQUATIONS. THE MEMBRANE CAPACITY IS $C = 1\mu F/cm^2$. THE VOLTAGE SCALE IS SHIFTED SO THAT THE RESTING POTENTIAL VANISHES. 99

TABLE 6.3 APPLICATIONS OF SPIKING NEURAL NETWORKS TRAINED BY STDP BASED ON DIFFERENT NEURAL CODING PARADIGMS AND DATA SETS..... 110

TABLE 7.1 A COMPARISON BETWEEN H-H MODEL AND THE SINGLE MTJ DEVICE. THE PERFORMANCE OF THE SINGLE MTJ DEVICE IS BASED ON EXPERIMENTAL RESULTS [250]. 113

TABLE 7.2 (A) MAGNETIC AND (B) GEOMETRIC AND THERMAL PARAMETERS USED IN THE MACROSPIN SIMULATIONS AT ROOM TEMPERATURE ($T = 300$ K). 117

Chapter 1 Introduction

This is the era of big data, where dealing with computers every day is a must. Recent advances in artificial intelligence (AI) have demonstrated unprecedented success in machine learning, enabling us to perform complicated tasks from vision to natural language and thus transforming the way we work and live. The algorithms behind are based on deep neural networks and are implemented by supercomputers. However, modern computers, which are based on the physical separation of the processing unit and the data storage unit, suffer from high energy consumption transiting data information between the storage and the processor, and the end of Moore's law [1].

Here comes the importance of an alternative computing paradigm known as 'Neuromorphic computing' that will allow computers to carry out complex operations faster, in an energy efficient manner, with fewer delays than conventional von-Neumann architectures. Neuromorphic chips mimic human brains with interconnected artificial neurons and synapses, thus allowing us to manufacture supercomputers that may at some point function better than our brains. In such chips, we must follow up with two processes. A bottom-up process where we should investigate a physical device that mimics biological neurons and synapses. In addition, a top-down process will be important to develop brain-inspired computing models to provide algorithm-level matching device physics.

Such artificial neural networks leak the reliability in mimicking biological neural networks, and this is analyzed in the way they transfer information as a static binary input, in addition to the used learning procedure and their power efficiency. Here comes the role of the third-generation neural networks known as spiking neural networks (SNNs), which are the type of networks that best mimic our brains.

Current neuromorphic systems, such as IBM's TrueNorth [2] and Intel's Loihi [3] exploit conventional complementary metal-oxide-semiconductor (CMOS) technology and relies mostly on architecture improvements to increase the neural network's efficiency. Implementation of different materials and devices, nonetheless, will allow for a better integration of the necessary neuromorphic properties directly at the material/device level by leveraging their non-linear functional response [4]. Compact task-oriented devices can substitute complex CMOS circuits to increase scalability and energy-efficiency. Memristors, for example, have gathered great attention due to their potential ability to mimic the spiking behavior as well as synaptic plasticity [5–9].

In this regard, the field of spintronics nanodevices, which exploit both the magnetic and electrical properties of electrons, have emerged to bring various exciting characteristics making them promising candidates characterized by low energy dissipation, non-volatility, high speed, reduced sizes and capable of naturally mimicking the spiking neurons [10,11]

and synapses [12–15] in neuromorphic systems. Magnetic textures, such as domain walls, Bloch and Néel types skyrmions, and radial and circular vortices are particularly intriguing as neuromorphic components because they can support different functionalities due to their rich physical mechanisms. To realize innovative spintronic devices, it is necessary to be able to write, manipulate, and read back data by means of nucleating, propagating, and detecting magnetic solitons. Driven by different means, solitons showed appealing applications in the fields of racetrack memories [16–18], as well as in neuromorphic computing devices [19–21]. Away from magnetic solitons, magnetic tunnel junctions (MTJs) were widely studied for synapse plasticity and firing applications [22,23].

My thesis is composed into two parts, firstly we study the concepts underpinning magnetic solitons, describe our results on their nucleation, propagation, and detection, and offer some perspectives for future research in this vibrant field. The second part focuses on building a spiking neural network based on spin-transfer torque magnetic tunnel junction (STT-MTJ) device, which showed success in mimicking the firing behavior of biological entities.

1.1 Thesis Overview

This thesis is structured as follows:

Chapter 2 shows the several aspects concerning Micromagnetics, to provide the fundamental background necessary to read the results of this thesis. First a short introduction on the micromagnetic formalism and the torques acting onto the magnetization vector of a ferromagnetic material have been presented.

In chapter 3, we present a comprehensive study using numerical and analytical methods of the stability and motion of Bloch and Néel skyrmions under the influence of Dzyaloshinskii–Moriya interaction (DMI) gradients. Our results show that under the influence of linear DMI gradients, Néel and Bloch-type skyrmions exhibit motion with finite skyrmion Hall angle. We also introduced the transformation of skyrmions into the 3D space to form “hopfions”, and we presented a brief study for their dynamics. This work provides a deeper and crucial understanding of the stability and gradient-driven dynamics of magnetic solitons and paves the way for the design of alternative low-power sources of magnetization manipulation in the emerging field of 2d materials.

Later in chapter 4, we study the stability and motion of radial and circular vortices under the influence of DMI gradients. Our results show that radial vortices exhibit motion with finite skyrmion Hall angle, however circular vortices undergo explosion dynamics.

In chapter 5, we will introduce magnetic tunnel junctions, their working principles, and the different switching paradigms. Moreover, the different MTJ parameters, and some MTJ based applications will be discussed.

Chapter 6 deals with the different aspects of neuromorphic computing and spiking neural networks, their real-life applications, the different neuronal models, and the learning procedure of such models.

Chapter 7, a detailed comparison between Hodgkin-Huxley neuron model and STT-MTJ will be provided. Then STT-MTJ synapse will be designed and implemented as the base in a spiking neural network (SNN).

Finally in Chapter 8, we will add the list of publications.

Chapter 2

Fundamentals of Micromagnetism

The computer was born to solve problems that did not exist before

Bill Gates

"The Landau-Lifshitz-Gilbert (LLG) equation is a fascinating nonlinear evolution equation both from mathematical and physical points of view. It is related to the dynamics of several important physical systems such as ferromagnets vortex filaments, moving space curves, etc. and has intimate connections with many of the well-known integrable soliton equations, including nonlinear Schrödinger and sine-Gordon equations. It can model multiple dynamical structures including spin waves, elliptic function waves, solitons, dromions, vortices, spatio-temporal patterns, and chaos, etc. depending on the physical and spin dimensions and the nature of interactions.

–Muthusamy Lakshmanan"

This chapter covers the fundamentals concerning micromagnetism. It is divided into four Sections. Primarily, a brief introduction of the micromagnetic formalism (section 2.1), the torques acting onto the magnetization vector of a ferromagnetic material will be discussed in section 2.2, section 2.3 will deal with the key concepts of Spin-Orbitronic and finally section 2.4 will discuss numerical Micromagnetism.

2.1 Introduction to Micromagnetism

The aim of micromagnetism is calculation of magnetic states and their dynamics for a given ferromagnetic system at a mesoscopic level [24–26]. The key assumption of micromagnetism is that the spin direction changes only by a small angle from one lattice point to the next [27]. The direction angles of the spins can be approximated by a continuous position vector **r**. Then the state of a ferromagnet can be described by the continuous vector field, the magnetization **M**(r) which is the magnetic moment per unit volume *dV* and has a modulus M_s constant in time (M_s is the saturation magnetization of the material) (See **Fig. 2.1**). The direction of **M** varies continuously with the coordinates x, y, and z. Particularly, the size of the volume must be chosen large enough to contain sufficient number **n** of magnetic momenta μ_i; on the other side, small enough to allow for the magnetization to easily change between each volume element.

The magnetization of a magnetic material with n atoms per unit volume is:

$$\mathbf{M}(\mathbf{r}, t) = \frac{\sum_{i=1}^{n} \boldsymbol{\mu}_i}{dV} \qquad (2.1)$$

The magnetization vector can be expressed in terms of the unit vector $\mathbf{m}(\mathbf{r},t) = \mathbf{M}(\mathbf{r},t)/M_s$. In 1935, the Landau–Lifshitz equation, named for Lev Landau, Evgeny Lifshitz, was set to describe the precessional motion of magnetization **M** in a solid.

The various forms of the equation are commonly used in micromagnetics to model the effects of a magnetic field on ferromagnetic materials. In particular, the fundamental energetic contributions, known as standard micromagnetic energies play an important role in the equilibrium configurations of the magnetization **M**.

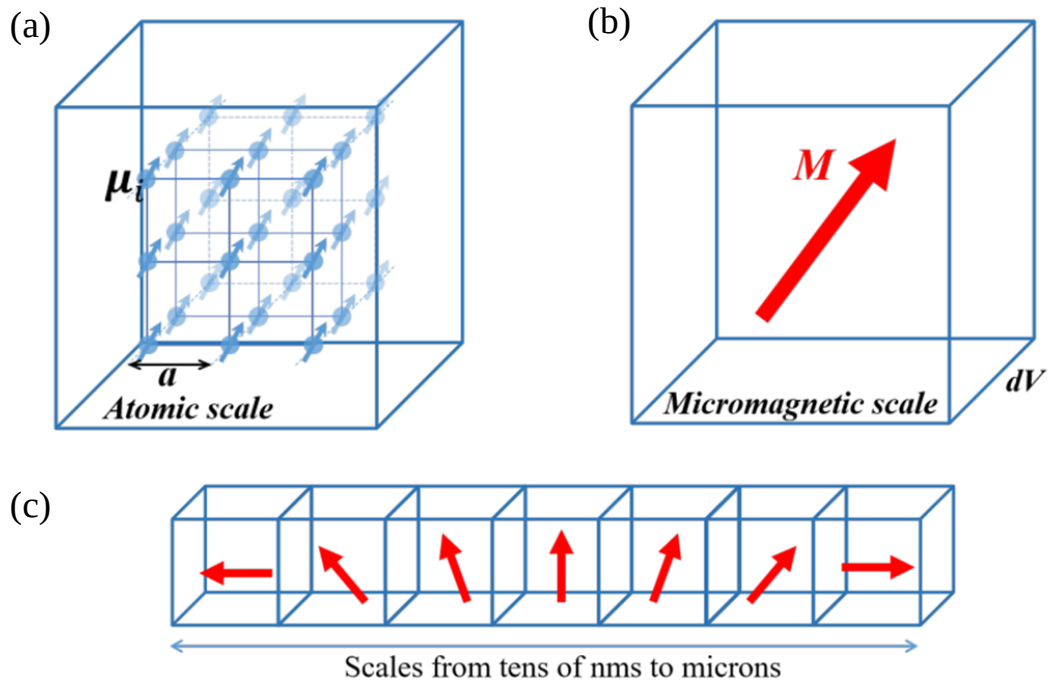

Figure 2.1 Scales in micromagnetism. (a) Atomic scale representation of individual magnetic moments μ_i. (b) Micromagnetic scale representation of the magnetization vector M defining as the sum of all magnetic moments μ_i inside the volume dV : $M = \frac{\sum_{i=1}^{n} \mu_i}{dV}$.

2.1.1 Exchange Energy

The exchange energy is of quantum mechanical nature. The energy of two ferromagnetic electrons depends on the relative orientation of their spins. When the two spins are parallel, the energy is lower than the energy of the antiparallel state. Qualitatively this behavior can be explained by the Pauli exclusion principle and the electrostatic Coulomb interaction.

The exchange energy, E_{ij}, between two localized spins is [28] :

$$E_{ij} = -2J_{ij}S_iS_j \quad (2.2)$$

Where J_{ij} is the exchange integral between atoms i and j, and $\hbar J_j$ is the angular momentum of the spin at atom i.

Expanding and rearranging, the volume energy density related to the exchange is,

$$\varepsilon_{ex} = A[(\nabla m_x)^2 + (\nabla m_y)^2 + (\nabla m_z)^2] \quad (2.3)$$

In **Eq. (2.3)** m_x, m_y, and m_z are the components of the magnetization direction in x, y, and z, respectively, and A is the exchange constant (J/m).

2.1.2 Uniaxial Anisotropy Energy

The anisotropy energy arises in crystalline lattices, the energy is lower for magnetization parallel to certain crystallographic directions: these are labelled easy axes of magnetization, against hard axes of magnetization [24,29]. The volume energy density an ε_{an} related to the uniaxial anisotropy is:

$$\varepsilon_{an} = k_1 \sin^2\theta + k_2 \sin^4\theta + k_3 \sin^6\theta \qquad (2.4)$$

where k_1, k_2, k_3 are uniaxial anisotropy constants expressed in J/m^3 and θ is the angle between the magnetization direction and the easy axis. Mostly, only the first term is considered, leading to:

$$\varepsilon_{an} = k_1[1 - (\mathbf{m} \cdot \mathbf{u}_k)^2] \qquad (2.5)$$

being u_k the unit vector of the easy axis. For $k_1 > 0$ ($k_1 < 0$) the axis is called easy (hard) axis since the magnetic moments will prefer to orient collinear (perpendicular) to it to reduce the anisotropy energy.

2.1.3 Magnetostatic Energy

The magnetostatic energy is associated to the interactions between the magnetic dipoles inside the material [24]. The magnetic field related to this energy is called demagnetizing field $\mathbf{H}_m$ (or dipole field inside the material). The magnetostatic energy of a uniformly magnetized ferromagnetic material of magnetization M is defined according to [30] by:

$$\varepsilon_m = \frac{-1}{2}\mu_0 \mathbf{M} \cdot \mathbf{H}_m \qquad (2.6)$$

The factor $\frac{1}{2}$ is introduced to avoid counting twice the interaction between couples of magnetic moments. The magnetostatic energy relies upon the geometrical properties of the ferromagnet as:

$$\mathbf{H}_m = -M_s(N_x m_x \hat{x} + N_y m_y \hat{y} + N_z m_z \hat{z}) \qquad (2.7)$$

where N_x, N_y, N_z are the shape-dependent demagnetizing factors along the *x*, *y*, *z* directions, respectively. For a sphere, the three demagnetizing factors are equal, $N_x = N_y = N_z = \frac{1}{3}$(for symmetry reasons) and there is no favored direction that minimizes the magnetostatic energy. For an infinitely long cylinder along the z direction $N_z = 0$ while $N_x = N_y = 1$, hence the magnetization favors lying along the axis of the cylinder.

2.1.4 Zeman Energy

Zeeman energy corresponds to the interaction between magnetization and the external magnetic field $\mathbf{H}_{ext}$. Its energy density ε_{ext} can be written as [24,29]:

$$\varepsilon_{ext} = -\mu_0 \mathbf{M} \cdot \mathbf{H}_{\text{ext}} \quad (2.8)$$

2.1.5 Thermal Energy

Temperature effect is usually included by adding a random noise thermal field $\mathbf{H}_{th}$ to the dynamic equation, which is thus converted into a stochastic one. In 1963, Brown showed that statistical properties correctly reproduce the equilibrium thermodynamics by applying this procedure to single domain particles. In micromagnetic simulations, the thermal random field $\mathbf{H}_{th}$ can be added to the effective field $\mathbf{H}_{eff}$ acting on the magnetization of each discretized cell:

$$\mathbf{H}_{eff} \rightarrow \mathbf{H}_{eff} + \mathbf{H}_{th} \quad (2.9)$$

The Cartesian components of $\mathbf{H}_{th}$ are independent Gaussian distributed random numbers with the following statistical properties:

$$\langle \mathbf{H}_{th,\alpha,i}(t) \rangle = 0 \quad (2.10)$$

$$\langle \mathbf{H}_{th,\alpha,i}(t) \mathbf{H}_{th,\beta,j}(t') \rangle = 2\mathrm{D}\delta_{ij}\delta_{\alpha\beta}\delta(t-t') \quad (2.11)$$

where i and j are the indexes of the cells, α, β = x, y, z indicates the Cartesian components of the field, and the brackets represent time statistical averages. The first δ_{ij} implies that the fluctuating term of different cells are independent from each other, the second one, $\delta_{\alpha\beta}$, means that the three Cartesian terms are independent from each other, the last term $\delta(t - t')$, indicates that the noise is uncorrelated in time. The coefficient D is obtained to satisfy Maxwell-Boltzmann statistics when thermodynamic equilibrium is reached, which leads to:

$$D = \frac{\alpha k_B T}{(1+\alpha^2)\gamma \mu_0 M_s V}, \quad (2.12)$$

where k_B is the Boltzmann constant, T the temperature and V is the volume of each individual cell. In the micromagnetic formalism framework, the fluctuating thermal field $\mathbf{H}_{th,i}$ added at each cell i is therefore given by,

$$\mathbf{H}_{th,i} = \eta_i(t) \sqrt{\frac{\alpha k_B T}{(1+\alpha^2)\gamma \mu_0 M_s V \Delta t}}, \quad (2.13)$$

where $\eta_i(t)$ is a stochastic vector with zero-mean and standard normal distributed random components. Δt is the time step used in the micromagnetic simulations.

2.2 Equilibrium and Dynamical Equations

As the previous energetic contributions play an important role in the equilibrium configuration of the magnetization, each contribution supports different energetic minima, thus the final equilibrium state is obtained by the balance between them.

The total energy density of a ferromagnetic body is given as the summation of all the previous energies:

$$\varepsilon_{tot} = \varepsilon_{ex} + \varepsilon_{an} + \varepsilon_m + \varepsilon_{ext} = A[(\nabla m_x)^2 + (\nabla_{m_y})^2 + (\nabla m_z)^2] + k_1[1 - (\mathbf{m} \cdot \mathbf{u}_k)^2] - \frac{1}{2}\mu_0 \mathbf{M} \cdot \mathbf{H}_{\mathrm{m}} - \mu_0 \mathbf{M} \cdot \mathbf{H}_{\mathrm{ext}} \qquad (2.14)$$

Based on a variational calculus, the effective field [29] can be defined as the functional derivative of the total energy density:

$$\mathbf{H}_{\mathrm{eff}} = -\frac{1}{\mu_0 M_s}\frac{\delta \varepsilon_{tot}}{\delta \mathbf{m}} \qquad (2.15)$$

where the functional derivative is expressed by:

$$\frac{\delta}{\delta \mathbf{m}} = \frac{\partial}{\partial \mathbf{m}} - \nabla \cdot \frac{\partial}{\partial(\nabla \mathbf{m})} \qquad (2.16)$$

The total effective field will then be given by:

$$\mathbf{H}_{\mathrm{eff}} = \frac{2A}{\mu_0 M_s}(\nabla^2 \mathbf{m}) + \frac{2k_1}{\mu_0 M_s}(\mathbf{m} \cdot \mathbf{u_k})\mathbf{u_k} + \mathbf{H}_{\mathrm{m}} + \mathbf{H}_{\mathrm{ext}} \qquad (2.17)$$

2.2.1 Dynamical equation

The precessional dynamics of the magnetization in magnetic layers are governed by the Landau-Lifschitz (LL) equation which was introduced by Landau and Lifshitz in 1935 to predict the motion of a single spin in Hamiltonian formalism [31],

$$\frac{d\mathbf{M}}{dt} = -\mu_0 \gamma(\mathbf{M} \times \mathbf{H}_{\mathrm{eff}}) - \frac{\mu_0 \gamma \alpha}{M_s}\mathbf{M} \times (\mathbf{M} \times \mathbf{H}_{\mathrm{eff}}) \qquad (2.18)$$

Later in 1954, Gilbert modified the form of the equation to account for the damping using a phenomenological approach [32,33] , thus Landau-Lifshitz-Gilbert equation (LLG) is given by,

$$\frac{d\mathbf{M}}{dt} = -\mu_0 \gamma(\mathbf{M} \times \mathbf{H}_{\mathrm{eff}}) + \frac{\alpha}{M_s}(\mathbf{M} \times \frac{d\mathbf{M}}{dt}) \qquad (2.19)$$

where γ is the gyromagnetic ratio, expressed by: $\gamma = \frac{ge}{2m_e} = \frac{g\mu_B}{\hbar}$ in A.m^{-1}.s^{-1} being g the Landé factor [34] , e and m_e the charge and the mass of the electron, respectively, μ_B the Bohr magneton and $\hbar$ the Planck's constant. In addition, α is the damping term without dimensions, **M** the magnetization in A.m^{-1}, M_s the magnetization saturation in A.m^{-1}, and $\mathbf{H}_{\mathrm{eff}}$ the effective field in A.m^{-1}.

For $\mathbf{m} = \mathbf{M}/M_s$, $\tau = \gamma_0 M_s t$ being the dimensionless time and α being the Gilbert damping, the LLG equation can be written as,

$$\frac{d\mathbf{m}}{d\tau} = -(\mathbf{m} \times \mathbf{h}_{\text{eff}}) + \alpha_G(\mathbf{m} \times \frac{d\mathbf{m}}{d\tau}) \quad (2.20)$$

Where, $\mathbf{h}_{\text{eff}} = \mathbf{H}_{\text{eff}}/M_s$.

The first term of this equation is the precessional term. It designs the rotational movement of the magnetization vector around its equilibrium position (see **Fig. 2.2 (a)**). This rotation is caused by a perturbation of the magnetic field inside the material.

The second term of Landau-Lifschitz of the equation describes the damping. This term is purely phenomenological. In fact, the amplitude of the oscillations of a spin decreases over time to allow magnetization to join the equilibrium position (see **Fig. 2.2 (b)**). Without this term the magnetization would rotate indefinitely.

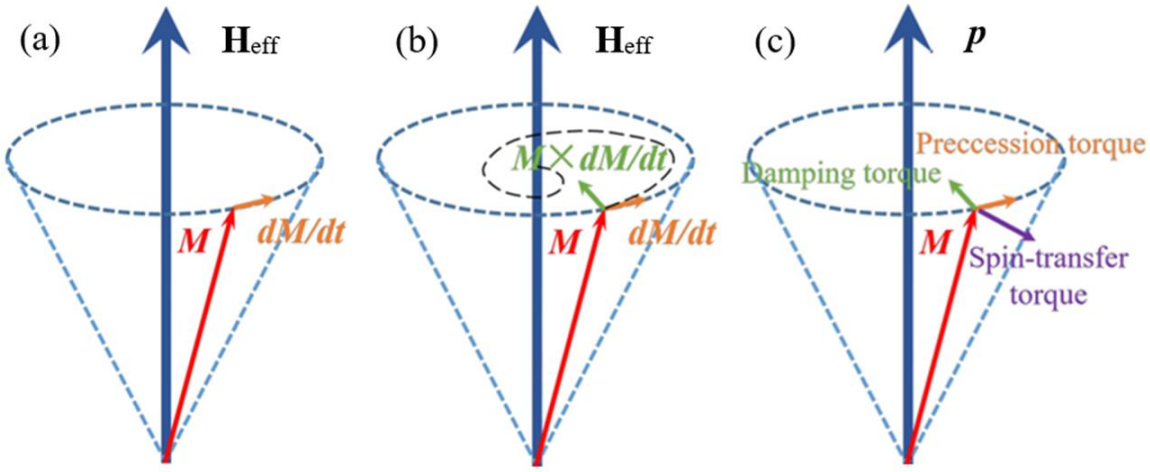

Figure 2.2 Schematic representation of the magnetization M in light red according the LLGS equation. (a) Precession term: The magnetization M processes around the effective field Heff following a circular trajectory of constant energy without damping effect. (b) Precession, and damping: The damping causes dissipation of the energy, and consequently the magnetization spirals back to the static equilibrium position. (c) Precession, damping and Spin-Transfer Torque: The STT acts as a source of energy which fully compensates for the damping. Therefore, energy is conserved, and the magnetization processes.

2.2.2 Spin-Transfer Torque

After the discovery of the STT by Slonczewski [35] and Berger [36] in 1996, another term was added to the LLG equation as shown in **Fig. 2.2 (c)**, accounting for the three aspects of the dynamics of the magnetization under current: Precession, Damping and STT.

Due to STT the electrons flowing through a magnetic layer are spin polarized along the magnetization of FM_1 (**Fig. 2.3**). When these spin-polarized electrons pass through another magnetic layer (FM_2), the polarization direction may have to change depending on the relative orientation of FM_1 and FM_2.

Part of the entering spins in the FM_1 are polarized in the same direction as M_1, generating the spin-polarized current, which will transfer a spin-torque onto the magnetization M_2 of the adjacent FM_2. Part of the entering spins is reflected with a polarization opposite to.

Two types of STT can be considered, the first one acts when the current flows perpendicularly to the plane of a multilayer that arises in out-of-plane (OOP) devices. The second one is exerted when the current flow is in-plane (IP) [36] that arises in IP devices.

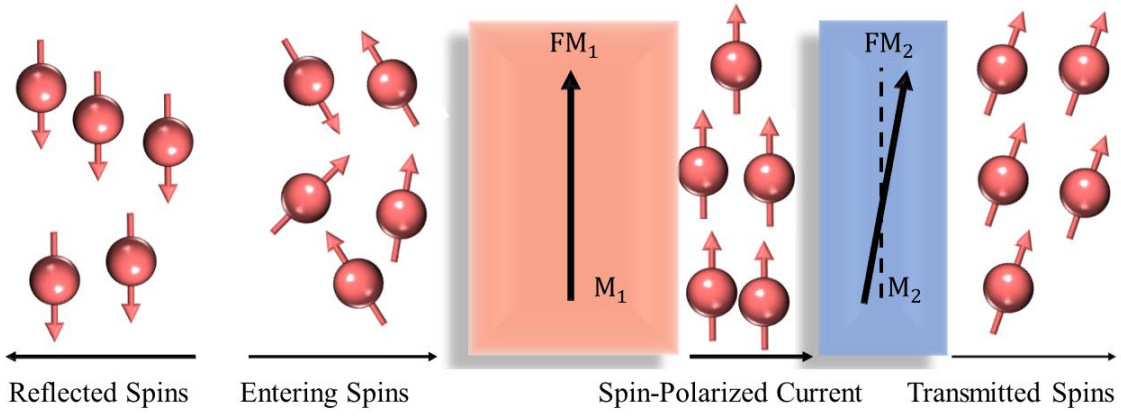

Figure 2.3 A simplified illustration of spin transfer torque process, FM_1 and FM_2 refers to ferromagnetic film with magnetization M_1 and M_2 respectively. The thick magnetic layer is used to produce a polarized electric current which in turn produces torque on M_2.

2.2.2.1 Out-Of-Plane (OOP) Devices

For understanding the behavior of spin transfer torque in OOP devices, the structure consists of two magnetic layers separated by a thin non-magnetic layer. Commonly, the device consists of a thick ferromagnet where the magnetization direction is fixed, to produce a spin-polarized current, and it is called pinned or fixed or reference layer or polarizer as well. The other ferromagnet is thinner to allow changes of its orientation and it is called free layer [37]. From a chemical point of view, the spacer layer can either be a spin valve (the spacer is an electrical conductor) or a magnetic tunnel junction (MTJ) (the

spacer is an electrical insulator). By passing an electrical current density $\mathbf{j_{FE\text{-}oop}}$ perpendicularly to the device through the pinned layer $\mathbf{m_p}$, one can produce a spin-polarized current and, thus it controls the magnetization $\mathbf{m}$ of the free layer, via STT $\boldsymbol{\tau_{oop}}$, which can be designed as an additional contribution to the LLG equation, as derived by Slonczewski [35]

$$\boldsymbol{\tau_{oop}} = \frac{g\mu_B \mathbf{j_{FE-oop}}}{\gamma_0 e M_S^2 t_{FL}} \varepsilon(\mathbf{m}, \mathbf{m_p})[m \times (\mathbf{m} \times \mathbf{m_p})] \qquad (2.21)$$

being t_{FL} the thickness of the free layer and $\varepsilon(\mathbf{m}, \mathbf{m_p})$ the polarization function, whose expression related to the relative orientation between the pinned and free layer magnetization.

For the case of magnetic tunnel junction (MTJ), the ε ($\mathbf{m}$, $\mathbf{m_p}$) expression becomes [38]:

$$\varepsilon_{MTJ}(\mathbf{m}, \mathbf{m_p}) = \frac{0.5\eta}{[1+\eta^2(\mathbf{m}\cdot\mathbf{m_p})]} \quad (2.22)$$

Now, it is worth noting that the Slonczewski torque acts as an anti-damping torque [39]. In fact, by looking at the damping torque in **Eqs. (2.18-2.19)**, with the STT expression, it is reasonable to note that they have a similar vector structure. Finally, the dimensionless ***Landau-Lifshitz-Gilbert-Slonczewski*** (LLGS) equation for an MTJ reads:

$$(1+\alpha^2)\frac{dm}{d\tau} = -(\mathbf{m} \times \mathbf{h_{eff}}) - \alpha(\boldsymbol{m} \times (\mathbf{m} \times \mathbf{h_{eff}})) + \frac{g\mu_B j_{FE-oop}}{\gamma_0 e M_S^2 t_{FL}} \varepsilon_{MTJ}(\mathbf{m}, \mathbf{m_p})[\mathbf{m} \times (\mathbf{m} \times \mathbf{m_p}) - q(V)(\mathbf{m} \times \mathbf{m_p})] \qquad (2.23)$$

where the dimensionless time step $d\tau = \gamma_0 M_s dt$ as been introduced and $q(V)(\mathbf{m} \times \mathbf{m_p})$ is the "out-of-plane" torque (an additional component of the STT term).

2.2.2.2 In-Plane (IP) Devices

An IP device can be visualized as a ferromagnetic wire that is characterized by a length much larger than its width, containing two different magnetic regions separated by DWs. By generating an electrical current density $\mathbf{j_{FE\text{-}ip}}$ through the strip, the current is naturally polarized and can produce a distortion motion of DWs (translation of the domains). More specifically, the electron spin is approximately parallel to the local magnetization and any modification in the spin direction induces a STT which shifts the DW along the wire length.

Here, we should distinguish between adiabatic τ_{IP}^{a} and non-adiabatic τ_{IP}^{na} STT given by,

$$\tau_{IP}^{a} = \frac{\mu_B P}{\gamma_0 e M_S^2}(\mathbf{j_{FE-ip}} \cdot \boldsymbol{\nabla})\mathbf{m}$$
$$\tau_{IP}^{na} = \frac{\mu_B P}{\gamma_0 e M_S^2}\boldsymbol{\beta}(\mathbf{j_{FE-ip}} \cdot \boldsymbol{\nabla})\mathbf{m} \qquad (2.24)$$

With P the spin polarization factor, which represents the number of spins polarized by the local magnetization, and β is the non-adiabatic parameter [40].

Considering adiabatic and no-adiabatic STT forms, LLG equation become,

$$\frac{d\mathbf{m}}{d\tau} = -(\mathbf{m} \times \mathbf{h_{eff}}) + \alpha_G \left(\mathbf{m} \times \frac{d\mathbf{m}}{d\tau}\right) + \frac{\mu_B P}{\gamma_0 e M_S^2}(\mathbf{j_{FE-ip}} \cdot \nabla)\mathbf{m} + \frac{\mu_B P}{\gamma_0 e M_S^2}\boldsymbol{\beta}(\mathbf{j_{FE-ip}} \cdot \nabla)\mathbf{m} \quad (2.25)$$

2.2.3 Voltage Controlled Magnetocrystalline Anisotropy

Voltage-controlled magnetic anisotropy (VCMA) is a technology that provides an energy-efficient approach to manipulate spintronic devices [41,42]. It has been proposed as an alternative writing mechanism that may solve limitations present in STT-MRAMs and enable higher bit density, as well as ultra-low power switching due to reduced ohmic dissipation [43]. The VCMA effect is induced by an accumulation of charge at the interface of ferromagnetic materials owing to an applied electric field [44].

2.3 Spin-Orbit Interactions

Spin-orbit interaction, describing the coupling between the orbital and spin degrees of freedom provides yet another avenue to control magnetism electrically. Angular momentum associated with the orbital degree of freedom provides yet another source which can be used to apply torque on the magnets. Thus, if a method can be devised to couple the orbital motion (which is controlled electrically) with the spin degrees of freedom, angular momentum can be exchanged with magnets electrically applying new kind of torques, referred to as the spin-orbit torques (SOT) [45]. This phenomenon led to a novel direction of Spintronics - that can be named spin-orbitronics [46–48].

The spin-orbit coupling (SOC) has two distinct origins: an intrinsic and extrinsic. The intrinsic effect is caused by spin-orbit coupling in the band structure of the semiconductor and survives in the limit of zero disorder, whereas the extrinsic effect is caused by spin-orbit coupling between Bloch electrons and impurities [49].

Both the extrinsic and intrinsic SOC are involved for the generation of spin-orbit associated phenomena, such as the anisotropic magnetoresistance (AMR), the spin-Hall effect (SHE), the anomalous Hall effect (AHE), and the Dzyaloshinskii-Moriya Interaction (DMI). In the following subparagraphs, the micromagnetic model of the SHE and DMI will be described.

2.3.1 Spin-Hall Effect

The spin Hall effect (SHE) is a transport phenomenon predicted by Russian physicists Mikhail I. Dyakonov and Vladimir I. Perel in 1971 [50,51]. It originates from the coupling of the charge and spin currents due to spin-orbit interaction where an ultrathin ferromagnetic layer is coupled to HM layer and the charge current flows through the HM as shown in **Fig. 2.4**.

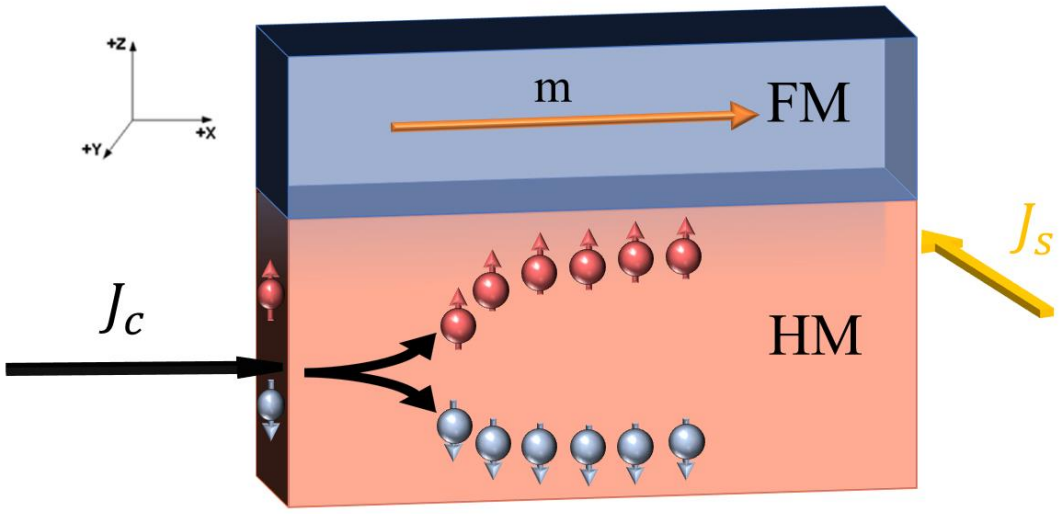

Figure 2.4 Schematic picture of the FM/HM bilayer, the charge current (Jc) entering the heavy metal induces the Spin Hall Effect (SHE), the opposite spin accumulations generate transverse spin current (Js) on the FM/HM interface.

A spin-current is generated from the charge current J_c because of the spin-dependent scattering in the HM, which create a spin accumulation of opposite sign at the upper and lower surface of the HM (the charge current is along the reference axis, the spin-polarization is along the y-axis as shown in **Fig. 2.4**). A vertical spin-current is generated and then absorbed by the FM, exerting a torque $\boldsymbol{\tau_{SHE}}$ on its magnetization that can be added as an additional term in **Eq. (2.20)**, which is given by the following relation:

$$\boldsymbol{\tau_{SHE}} = -\frac{g\mu_B\theta_{SH}}{2\gamma_0 e M_S^2 t_{FL}}\mathbf{m}\times\mathbf{m}(\hat{z}\times\boldsymbol{j}_{HM}) \qquad (2.26)$$

being θ_{SH} the spin-Hall angle, which represents the amount of charge current J_c converted into spin-current $j_s = \theta_{SH}J_{HM}$. $\hat{z}$ is the unit vector in the OOP direction.

2.3.2 Dzyaloshinskii-Moriya Interaction (DMI)

DMI is an antisymmetric exchange interaction that occurs at the interface between ferromagnetic (FM) and heavy metal (HM) layers. The HM atoms with the large spin–orbit coupling mediate the interaction between neighbor spins in the FM medium separated by a distance $\mathbf{r_{ij}}$, leading to their non-collinear alignment [52]. We can distinguish between two types of this interaction: the DMI in bulk material and at the interface of an ultrathin film (see **Fig. 2.5**). Bulk DMI (bDMI) originated from the indirect exchange mechanism between two spins (S_1 and S_2) with a large neighboring atom having large SOC, whereas

Interfacial DMI (iDMI) takes place at the interface between a ferromagnetic thin film (grey) and a metallic layer (blue) having large SOC [53].

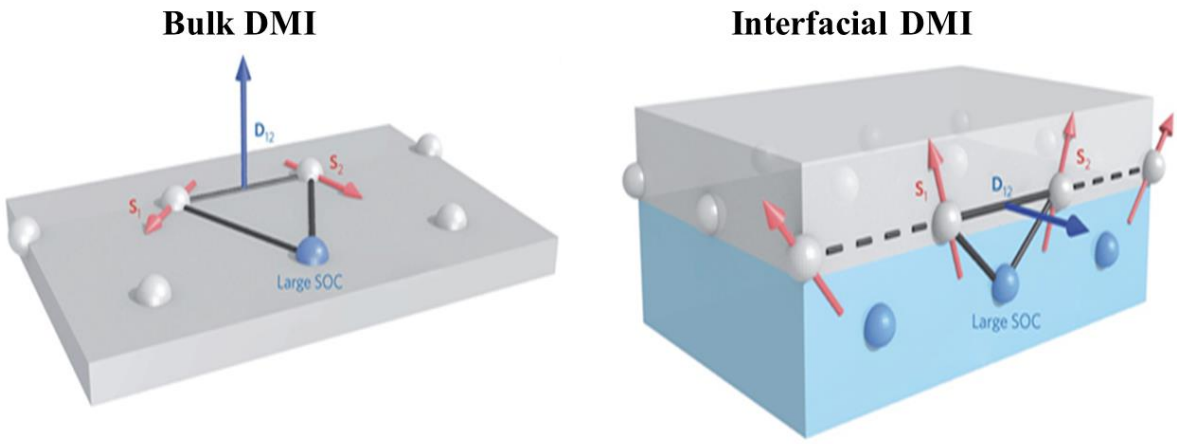

Figure 2.5 Sketch of Bulk DMI, and Interfacial DMI. The resulting bulk and interfacial DMI vector point perpendicular to the triangle consists of two magnetic atoms and an atom with large SOC [53] .

The energy density for the two types of DMI is expressed by the following way [54]:

$$\varepsilon_{bDMI} = D\mathbf{m} \cdot \nabla \times \mathbf{m} \quad (2.27)$$

$$\varepsilon_{iDMI} = D[m_z \nabla \cdot \mathbf{m} - (\mathbf{m}.\nabla)m_z] \quad (2.28)$$

D being the parameter considering the intensity of the DMI. Indeed, for the expression of ε_{iDMI},we assume $\frac{\partial \mathbf{m}}{\partial z} = 0$.

Afterwards, the expression of the dimensionless DMI fields:

$$h_{bDMI} = \frac{-1}{\mu_0 M_s}\frac{\delta \varepsilon_{bDMI}}{\partial \mathbf{m}} = \frac{-D}{\mu_0 M_s}\nabla \times \mathbf{m} \quad (2.29)$$

$$h_{iDMI} = \frac{-1}{\mu_0 M_s}\frac{\delta \varepsilon_{iDMI}}{\partial \mathbf{m}} = \frac{-D}{\mu_0 M_s}[(\nabla \cdot \mathbf{m})\hat{z} - \nabla m_z] \quad (2.30)$$

The DMI also affects the boundary conditions (BC) of the ferromagnet as shown in the following equations [32]:

$$\text{Bulk DMI BC: } \frac{d\mathbf{m}}{dn} = \frac{\mathbf{m}\times\mathbf{n}}{\xi}$$
$$\text{nterfacial DMI BC: } \frac{d\mathbf{m}}{dn} = \frac{1}{\xi}(\hat{z} \times \mathbf{n}) \times \mathbf{m} \quad (2.31)$$

where $\xi = \frac{2A}{D}$ is a characteristic length and A is the exchange constant.

Later, in chapter 3 and chapter 4, we will show how DMI acts as a fundamental interaction for stabilizing a magnetic soliton.

2.4 Numerical Micromagnetism

Numerical micromagnetism is introduced to study different interesting phenomena of magnetization dynamics, from either the point of view of fundamental physics or from experimental devices. As has been seen in previous sections, magnetization dynamics is described using non-lineal partial differential equations in space and time, which are significantly complicated to solve and in general do not have analytical solutions. The main idea of numerical micromagnetism is discretizing the previously obtained continuous expressions including the discretization of the geometry and of the dynamic equation, as well as all the different effective field contributions to solve the problem numerically [55].

For the spatial discretization of the geometry, the most popular methods applied in micromagnetic solvers are the finite-difference method (FDM) and the finite-element method (FEM). In both methods the magnetic region is subdivided into simulation cells resulting in a mesh. The two methods differ in how the structures are discretized. As a result, their formulation, implementation, speed, and numerical accuracy are different. To ensure accurate simulations, it's important to make sure that the cell size used in the discretization process (i.e., the size of the computational grid cells) is smaller than the exchange length. This ensures that the simulation captures the relevant physics accurately. If the cell size is too large compared to the exchange length, important details of the magnetic behavior at smaller length scales may be missed, leading to inaccuracies in the simulation results.

FDM uses a regular grid of rectangular brick cells, at which the differential operators can be approximated by central differences [56]. The volume of each brick cells is $\Delta x \times \Delta y \times \Delta z$. Due to the regularity of the discretization grid, the formulation of the micromagnetic modeling with FDM is relatively simple and the implementation is quite straightforward. Moreover, the computational speed of FDM can be good for simple magnetic structures, such as thin rectangular films. Therefore, it is extensively utilized in the micromagnetics community for such cases.

On the other hand, FDM suffers from certain factors that prevent the universal application of the method. Most importantly, the modeling accuracy for the magnetic samples that come with fine geometrical features can be unsatisfactory. This is because regular brick cells are intrinsically unsuited to model curved boundaries. FEM greatly solves this problem by applying arbitrary shaped finite elements in the mesh. Each finite element could be a triangle, a quadrilateral, or even a curved triangle in a two-dimensional case. As to three-dimensional mesh, the elements could be tetrahedrons, hexahedrons, pyramids, and prisms [57]. The flexibility in the discretization allows for superior geometric modeling accuracy. The modeling flexibility and accuracy come, however, with complexities in

formulation and implementation. The computational speed may be slower than that of FDM when handling simple magnetic structures.

For the discretization of the micromagnetic equations, it is essential to find the discrete counterparts to the continuous functions that describe all the contributions to the local effective field $\mathbf{H}_{\text{eff}}$, in each computational cell. In the FD approximation the derivatives are replaced by ratios at the center of each cell of the mesh. Among all the energy contributions, the evaluation of demagnetization energy, which is a long-range interaction, is the most complicated one and is extremely time-consuming. It has a computational complexity of $\mathcal{O}(n^2)$, with n being the number of simulation cells. Various methods have been proposed to reduce this complexity, and the widely used fast-Fourier-transform (FFT) based circular convolution method is able to reduce this complexity to $\mathcal{O}$ (nlogn) [58].

To numerically solve the LLG equation including the spin-torque effect and all effective field components, different ordinary differential solver algorithms, which are based on a few explicit Runge-Kutta methods such as the Dormand-Prince method (RK45), the Bogacki-Shampine method (RK32), and Heun's method (RK12) can be implemented.

2.4.1 Software Packages

Various micromagnetics software packages are used to simulate and analyze the behavior of magnetic materials. We can differentiate between them through their features, implementation, and user interface. This includes the most popular open-source FD micromagnetic software: OOMMF [59], which is a multi-platform code running on central processing units (CPUs). It is implemented using C++ and Tcl/Tk scripting language, and offers a wide range of simulation capabilities, including various micromagnetic models, exchange and demagnetization energies, and support for different boundary conditions. Other CPU based software exists including Fidimag and the commercial package MicroMagus [60].

Due to the increasing need for high parallelism and efficient performance in numerical micromagnetics, graphics-processing unit (GPU) based software was introduced. A popular open-source package for finite-difference micromagnetics on GPUs is MuMax3 [61,62], developed at Ghent University and particularly known for its performance in simulating large-scale magnetic structures with high fidelity.

In my thesis, I utilized a diverse array of computational tools to address the complex challenges inherent in my research. Leveraging the capabilities of various software packages such as Mumax, Petaspin code, MATLAB, and Python allowed for a comprehensive exploration of the phenomena under investigation.

The state-of-the-art micromagnetic solvers that helped me widely in my simulations, is the local PETASPIN code. It is implemented by prof. Luis Torres group in Salamanca before 2002, as a CUDA-native and multi-GPU solver benchmarked against the standard problems of micromagnetic community [63]. Our code uses the Adams Bashforth [64,65]

method to numerically integrate the Landau-Lifshitz-Gilbert (LLG) equation. The simulation results of PETASPIN coincide with the ones of OOMMF and Mumax3.

Petaspin code served as robust micromagnetic simulation platforms, enabling the simulation and analysis of intricate magnetic structures and dynamics. It also provided valuable insights into the behavior of magnetic materials at the microscale, facilitating the elucidation of underlying mechanisms and the prediction of emergent phenomena.

Complementing these simulations, MATLAB and Python were instrumental in data analysis, visualization, and algorithm development. MATLAB's rich numerical computation and visualization capabilities, coupled with Python's versatility and extensive library ecosystem, empowered me to tackle complex computational tasks with efficiency and flexibility. By seamlessly integrating these software packages into my research workflow, I was able to achieve a comprehensive understanding of the studied systems and generate impactful insights contributing to the advancement of my field.

Chapter 3

Magnetic Skyrmion

Our intelligence is what makes us human, and AI is an extension of that quality

Yann LeCun

"The skyrmion can be extremely small with diameters in the nanometer range and, importantly, they behave as particles that can be moved, created or annihilated, making them suitable for abacus-type applications in information storage, logic or neuro-inspired technologies.

–Albert Fert "

This chapter concerns the study of magnetic skyrmions. Section 3.1 is a background about skyrmion and its applications. Section 3.2 is divided intp three parts and it deals with topology of the magnetic skyrmion and shows its different configurations. Section 3.3 is divided into two main parts. Then manipulation and dynamics of skyrmions are presented in section 3.3. Transformation from 2D skyrmions into 3D hopfions will be discussed in section 3.4. Finally, section 3.5 is a brief conclusion.

3.1 Introduction to Magnetic Skyrmions

Magnetic skyrmions are chiral spin textures with a whirling configuration forming in thin ferromagnets. Originally, it was proposed by British nuclear physicist Tony Skyrme in the 1960's as a quasi-particle-like topological excitation in certain field theories for the description of the interactions of pions.[66] Later in the 1990's, Bogdanov et al. for the first time theoretically suggested that the topologically protected skyrmion can exisit as a stable or metastable state in magnetic materials with Dzyaloshinskii–Moriya interactions (DMIs) [67]. In 2001, Bogdanov and Rößler theoretically predicted and described the skyrmion in magnetic thin films [68].

In 2009, Mühlbauer et al. first experimentally observed the Bloch skyrmions in the group of B20- type transition metal compounds [69–71]. Most of the B20 compounds including (MnSi [72–75], FeGe [76–78], MnGe [79,80], $Fe_xCo_{1-x}Si$ [81,82], $Co_{1+x}Si_{1-x}$ [83], $Mn_xFe_{1-x}Si$ [84,85]...) stabilize two-dimensional Bloch skyrmion lattices and share a common magnetic field-temperature phase diagram in terms of the spin textures except MnGe and compounds close to its composition. Later Bloch skyrmions were observed in β-Mn-type compounds such as CoZnMn alloys and molybdenum nitrides [86], in addition to polar magnets [87].

Interfacial Dzyaloshinskii–Moriya interactions (iDMI) being the dominant interaction stabilizing the Néel type skyrmions, it can be optimized using HMs that induce opposite iDMI signs at the top and bottom FM interfaces [88,89]. The iDMI vector always aligns along the interface plane and stabilizes Néel skyrmions. The first iDMI material reporting the observation of a Néel skyrmions consists of a single monolayer (ML) of Fe deposited on Ir(111) single crystal substrate denoted as Ir(111)/Fe(1ML) in 2011 at temperatures below 28 K [90].

Later, Néel skyrmions have been observed in a variety of thin film materials with a perpendicular easy-axis of the magnetization and interfacial DMI (iDMI), including Heavy Metal (HM)/single-layer ferromagnet (FM)/oxide [91,92], HM1/FM/HM2 multilayers [88,93], HM/ferrimagnet/oxide multilayers [94,95] combinations of FM/ferrimagnets [96,97], as well as synthetic antiferromagnets (SAFs) [98–100].

Recently, 2d materials have been hailed as building blocks for the next generation electronic devices [101]. Several 2d materials, such as CrI_3 [102], Fe_3GeTe_2 [103], and VSe_2 [104], have shown potentials for the stabilization of non-collinear magnetic textures and spintronic applications. Interesting features of 2d materials, in CrI_3 and in Janus

monolayers Cr $(I, X)_3$ (X = Br, Cl), is the voltage and strain control of magnetic parameters relevant for magnetic textures stability [105–107]. The DMI energetic density expressions and the boundary conditions controlling both types of skyrmions are given in **section 2.3.2** (**Eqs. (2.27-2.31)**).

3.1.1 Skyrmion Based Technology

The attraction of skyrmions rises for many reasons, including their ultra-low energy consumption for manipulation and motion, they retain their state even in the absence of power, support parallel processing and sparse connectivity, as well as their rich dynamic behaviors, including motion, annihilation, and creation. Utilizing its properties allows a successful implementation of synaptic plasticity in neuromorphic systems, with reduced hardware overhead and improved performance. A pioneering application of skyrmions was the racetrack memory [16,53], where Tomasello et al.[16] suggested four different scenarios (A), (B), (C) and (D) as shown in **Fig. 3.1** for designing a skyrmion racetrack memory combining Bloch or Néel skyrmions. The manipulation of both skyrmion types by spin current generated within the ferromagnet or via the spin-Hall effect arising from a non-magnetic heavy metal underlayer, showed that Néel skyrmion moved by the spin-Hall effect (**Fig. 3.1(a)**) is a very promising strategy for technological implementation of the next generation of skyrmion racetrack memories.

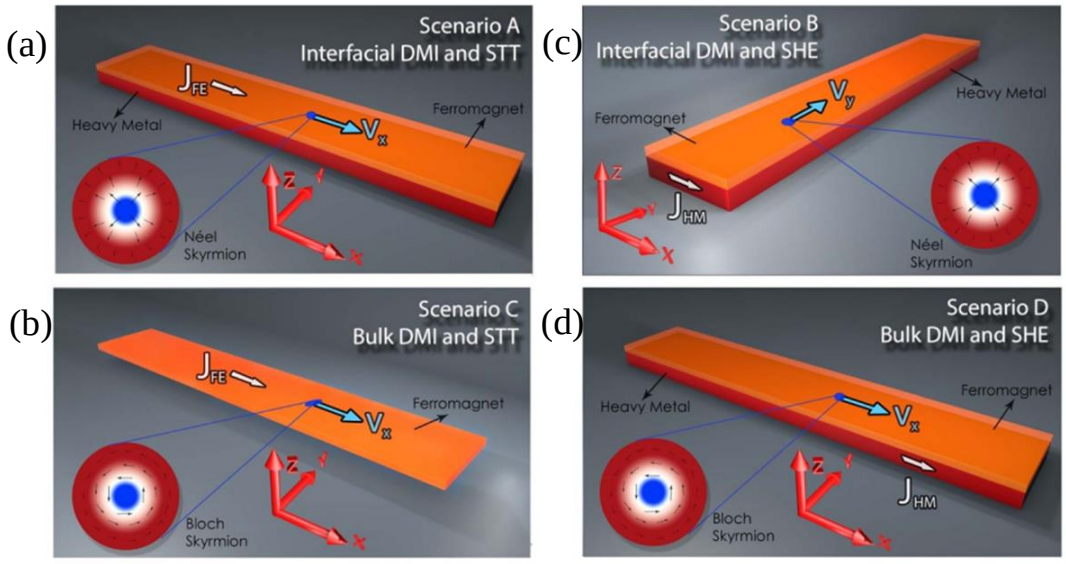

Figure 3.1 Four different scenarios for the design of a skyrmion racetrack memory. (A), Néel skyrmion motion driven by the STT. (B), Néel skyrmion motion driven by the SHE. (C), Bloch skyrmion motion driven by the STT. (D), Bloch skyrmion motion driven by the SHE. The four insets show the spatial distribution of the Néel and Bloch skyrmion, where the background colors

refer to the z-component of the magnetization (blue negative, red positive), while the arrows are related to the in-plane components of the magnetization. The current flows along the x-direction. The skyrmion moves along the x-direction in the scenarios A, C, and D and along the y-direction in the scenario B.

Many other skyrmion based applications have been proposed, such as oscillators [108–111], detectors [112], random bit generator [113], logic gates [114]. Beyond data storage and memory applications, the diverse magnetic skyrmion interactions and excitations can be further exploited for conventional logic computing and unconventional computing like, probabilistic [115], Brownian computing [116], and neuromorphic computing.[117]. One interesting application in this field is a skyrmion-based artificial synaptic illustrated in **Fig. 3.2(a)**, used to perform pattern-recognition using handwritten data set, reaching to the accuracy of ~89% [117]. Beside simulations, experiments were carried out to measure the electrical operations of a skyrmion synapse (**Fig.3.2(b)**), where the corresponding magnetic configuration of each resistance state is also imaged by STXM as shown in **Fig.3 2(c)**.

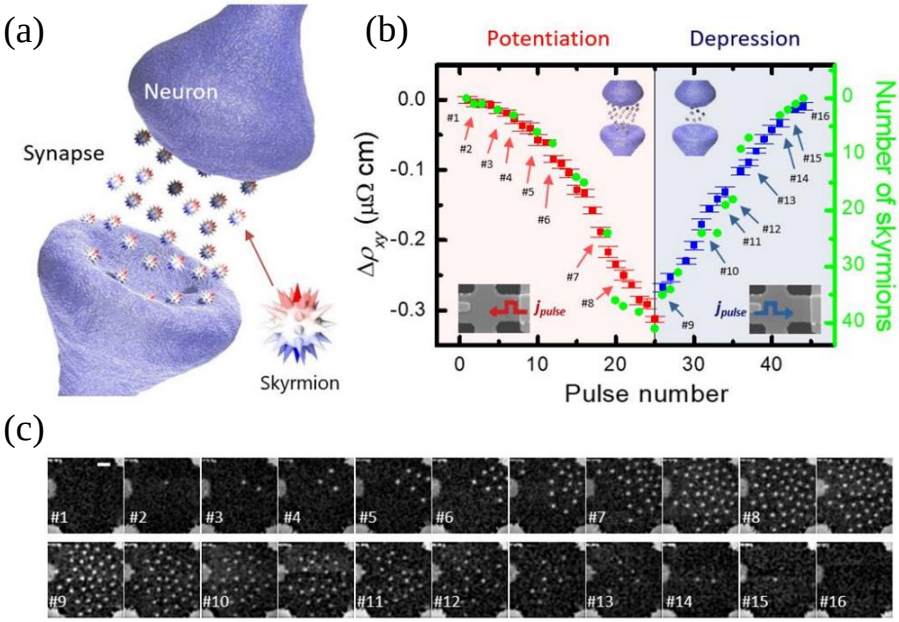

Figure 3.2 (a) Schematic drawing of skyrmion-based artificial synapse, illustrating, Néel skyrmions in thin films mapped onto spheres and are shown in three-dimensional space. The red and blue colored arrows represent magnetic moments pointing +z and -z directions within skyrmions, respectively. The synaptic weights are proportional to the number of skyrmions, which is modulated by the electric current-controlled accumulation and dissipation of them. (b), The measured Hall resistivity change and calculated skyrmion number as a function of injected pulse number. Note that red and blue symbols and colored areas correspond to resistivity changes during potentiation and depression, respectively. Green symbols are used to indicate the number

of skyrmions. Enclosed electrical pulses indicate the direction of charge current pulse, opposite to the direction of electron flow. Error bars denote the standard deviation of the resistivity measurements at each state. (c), Sequential STXM images showing skyrmion populations after injecting unipolar current pulses along the track, during potentiation and depression, respectively, and each image number, #1-#16, corresponds to each resistivity state indicated in (b).

3.2 Skyrmion Properties & Stabilization

In this section, the topological nature and corresponding range of possible configurations of skyrmions are described mathematically. Magnetic skyrmion materials are presented and categorized based on their configuration and the dominant magnetic interactions stabilizing them, including bDMI, and iDMI. In addition, other conditions such as temperature, pressure, magnetic field, electrical field, geometrical constraint, and strain also play a role in stabilizing skyrmions.

3.2.1 Topology and Skyrmion Number

The stability of magnetic skyrmions had been closely linked to the topological configuration of their vector field of magnetic moments. In mathematics, topology refers to the study of geometric properties preserved under continuous deformations such as stretching, twisting, and bending without tearing. Theoretically, a skyrmion described by a continuous vector field is topologically protected because its annihilation requires the transformation into a topologically trivial state.

For two-dimensional magnetic skyrmions on a film, its topology is quantified by the winding number, also known as skyrmion topological number N_{sk} given by [118,119]:

$$N_{sk} = \frac{1}{4\pi} \iint \vec{\mathbf{m}} \cdot \left(\frac{\partial \vec{\mathbf{m}}}{\partial x} \times \frac{\partial \vec{\mathbf{m}}}{\partial y}\right) dxdy \qquad (3.1)$$

where $\vec{\mathbf{m}}(x, y)$ is the normalized magnetization with the magnitude of 1. This expression computes the number of times $\vec{\mathbf{m}}$ wraps around a unit sphere. Hence the structure of a skyrmion have N_{sk} of ± 1. In contrast, the winding number of a plane with uniform magnetization is 0. Thus in the context of finite samples, continuous transformations between these two states are prohibited, and skyrmions can resist annihilation by minor deformations. This stability arising from the geometry or configuration of the skyrmion is referred to as topological stability. Generally, the skyrmion number connects to the total variation of the magnetization angle when moving counterclockwise around a circle, divided by 2π [119].

3.2.2 Skyrmion Configuration

The magnetization $\vec{\mathbf{m}} = (m_x, m_y, m_z)$ configuration of a two-dimensional skyrmion is preferably described by polar coordinates over cartesian coordinates given the skyrmions circular symmetry [120]. The assumption of circular symmetry is valid for a magnetic skyrmion at equilibrium without an in-plane magnetic field. The transformation of spatial coordinates between cartesian $\vec{r}(x, y)$ and polar $\vec{r}(r, \varphi)$ coordinates is given by,

$$x = r\cos\varphi \text{ and } y = r\sin\varphi \qquad (3.2)$$

where **r** is the radial distance from the center of the skyrmion, and **φ** is the azimuthal angle in space. The direction of $\vec{\mathbf{m}}(\theta, \phi)$ vector is described using spherical coordinates given by,

$$\vec{\mathbf{m}}(\theta(r, \varphi), \phi(r, \varphi)) = (\sin\theta\cos\phi, \sin\theta\sin\phi, \cos\theta) \qquad (3.3)$$

where θ is the polar angle and ϕ is the azimuthal angle of the vector.

With the assumption of circular symmetry, the dependence of θ (r,φ) and ϕ (r,φ) are both simplified to θ (r) and ϕ (φ) respectively. By substituting $\vec{\mathbf{m}}(\theta(r), \phi(\varphi))$ into the **Eq. (3.1)** we obtain,

$$N_{sk} = -\frac{1}{4\pi}[cos\theta(r)]_{r=0}^{r=R}[\emptyset(\varphi)]_{\varphi=0}^{\varphi=2\pi} \qquad (3.4)$$

where R corresponds to the radial distance at which $\vec{m}$ becomes fully antiparallel to its core. The term $[cos\theta(r)]_{r=0}^{r=R} = \pm 2$ depends on the polarity or orientation of the skyrmion core. A core in the positive $\hat{z}$ direction returns the value of −2 and vice versa. The term $[\emptyset(\varphi)]_{\varphi=0}^{\varphi=2\pi}$ depends on the skyrmion's vorticity ω defined as $\omega = [\emptyset(\varphi)]_{\varphi=0}^{\varphi=2\pi}/2\pi$. ω describes the relative direction of change in the azimuthal angles φ and ϕ of space and magnetization vector, respectively. ω is +1 if they are unidirectional and −1 if they are in opposite directions. Based on **Eq. (3.4)**, an additional phase term γ defined as the skyrmion helicity can be introduced to ϕ (φ) while conserving the magnitude of N_{sk}, to give,

$$\phi(\varphi, \gamma) = \omega\varphi + \gamma \qquad (3.5)$$

where $\gamma = (-\pi\ \pi]$.

Particularly, we can distinguish between two types of skyrmions: Bloch-Type and Néel Type skyrmions. Bloch and Néel skyrmions both have positive ω but differ in γ as shown in the first and third row of Fig. 3.3. Bloch skyrmions have $\gamma = \{\frac{-\pi}{2}, +\frac{\pi}{2}\}$ that manifest as clockwise (CW) or counterclockwise (CCW) vortex-like configurations, while Néel skyrmions have $\gamma = \{0, \pi\}$ that manifest as spike-like configurations [121].

It is important to note that skyrmions can have any γ between −π and π, and Bloch and Néel skyrmions are merely nomenclature used to describe several specific cases of γ. The second and final row of skyrmions with negative ω shown in **Fig. 3.3** correspond to anti-skyrmions. Anti-skyrmions are topologically equivalent to skyrmions but have alternating Bloch and Néel characters around their core. The configuration of anti-skyrmions is independent of γ due to its rotational symmetry, and hence are effectively characterized by its vorticity alone.

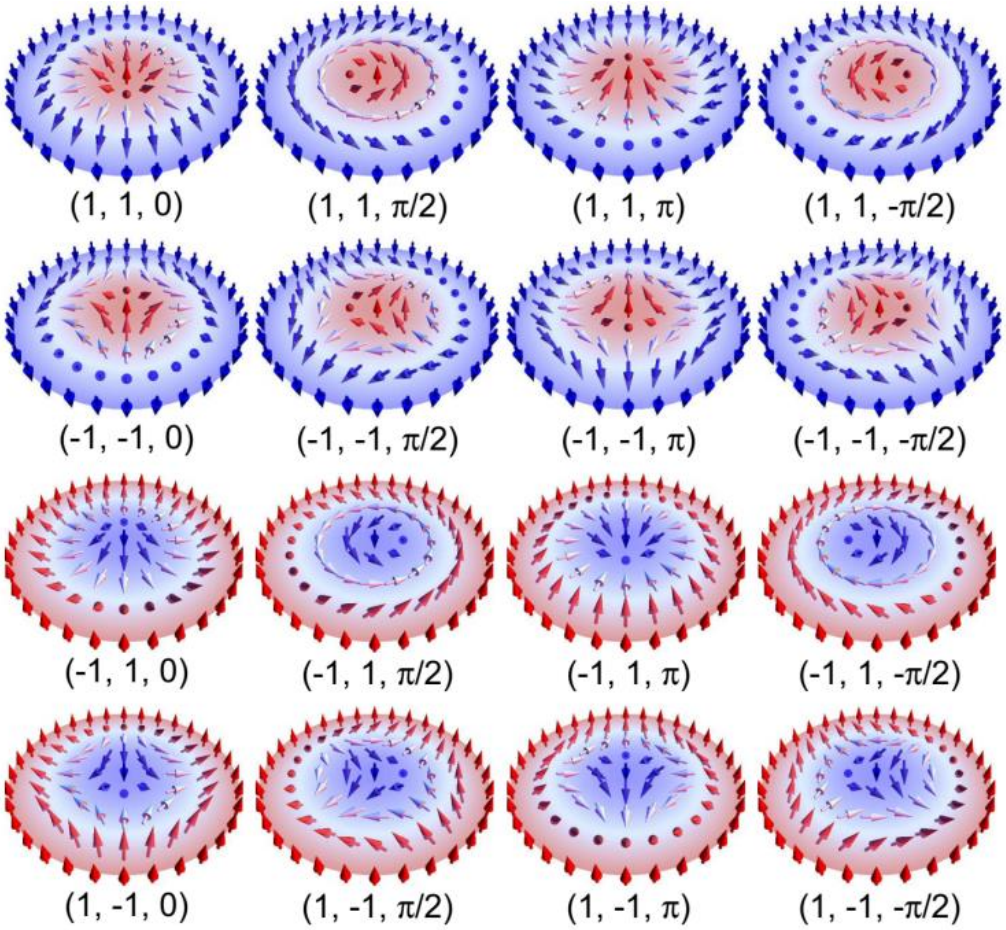

Figure 3.3 Illustration of magnetic skyrmions described by the skyrmion number N_{SK}, vorticity and helicity. The arrow denotes the spin direction while the color denotes the out-of-plane spin value, where red is out of plane, white is IP and blue is into the plane. Adapted from [121].

The two types of skyrmions can be stabilized in the existence of two types of DMI. The DMI in bulk material stabilize Bloch skyrmions, characterized by a vortex like configuration of the domain wall spins (see **Fig. 3.4(a)**); while in the iDMI, Néel skyrmions are obtained which have a radial distribution of the domain wall spins (see **Fig. 3.4(b)**) [53]. Hence, the sign of the DMI parameter plays an important role in the chirality of the two types of skyrmions. It is necessary to underline that the skyrmion has a double protection due to the energetic minimum and the topology.

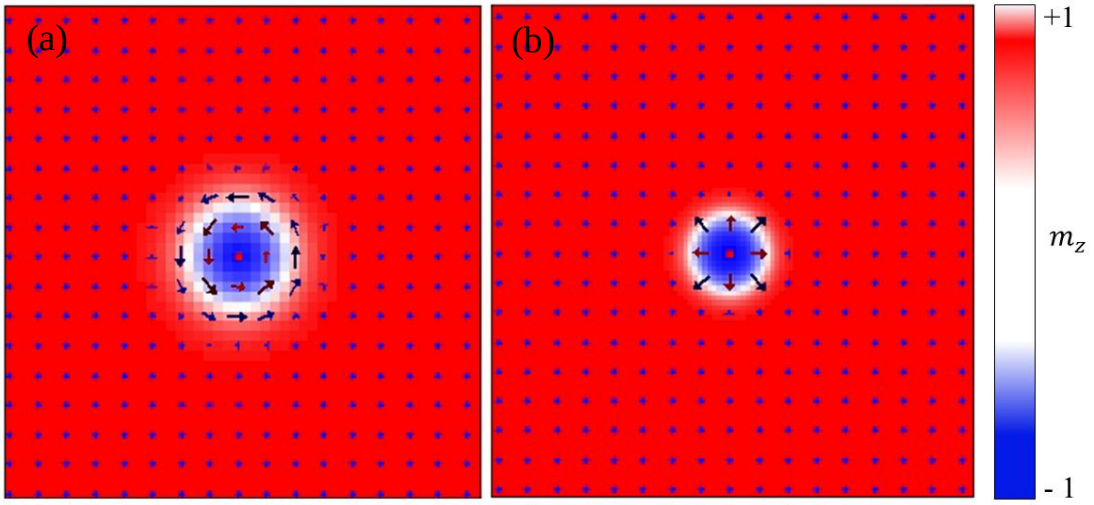

Figure 3.4 Magnetization distribution of a (a) Bloch skyrmion, (b) Néel skyrmion. The color bar denotes the out-of-plane magnetization component m_z: red positive, white zero, and blue negative.

3.2.3 Approaches for Skyrmion Stabilization

A wide variety of approaches were proposed for the manipulation of skyrmions and vortices, including electrical currents through the conventional spin-orbit torques (SOT) [122] external field gradients [123,124], anisotropy gradients, as well as thermal gradients [125–127]. Notably, parameters gradients prove to be very useful in inducing dynamics in the case of electrical insulators compared to electrical manipulation.

3.3 Manipulation of Magnetic Skyrmions Under DMI Gradient

In this section, we present a comprehensive study using numerical and analytical methods of the stability and gradient-driven dynamics of Bloch and Néel skyrmions under the influence of DMI gradients in different geometries (circular and square samples) and two materials (thin film *CoFeB* [128] and 2d CrI_3 [129]). Our results show that under the influence of linear DMI gradients, Néel and Bloch-type skyrmions exhibit motion with finite skyrmion Hall angle. A theoretical analysis was carried out via systematic micromagnetic simulations and corroborated by the Thiele's formalism.

3.3.1 Modeling and Sampling

This section is divided into 3 subsections, where we present the sample, we are simulating, the magnetic properties of our sample, the Thiele's equations governing the motion of the skyrmions, as well as the results.

3.3.1.1 Micromagnetic Modeling

The micromagnetic computations were performed with a state-of-the-art micromagnetic solver, PETASPIN (**section 2.4.1**), which numerically integrate the Landau-Lifshitz-Gilbert (LLG) equation given by **Eq. (2.20)**. For skyrmions, we consider both types of DMI given by **Eqs. (2.22-2.31)**, leading to stabilization of Bloch and Néel types. It has been experimentally shown that while an odd number of layers CrI_3 reveals ferromagnetism, for an even number of layers an antiferromagnetic interlayer coupling is observed [130,131]. Thus we considered an SAF (square & circular samples) compose of two CrI_3 layers separated by a non-magnetic layer as shown in **Fig. 3.5** below, and simulated the antiferromagnetic interlayer coupling as a Ruderman-Kittel-Kasuya-Yosida (RKKY) interaction added to the effective field, hence as a standard SAF $h_{ex,i}^{inter} = \frac{A^{ex}}{\mu_0 M_s^{2j} t_{NM}} \mathbf{m}^j$ [132], where $i,j = L, U$, A_{ex} is the interlayer exchange coupling constant, μ_0 is the vacuum permeability, and t_{NM} is the thickness of the non-magnetic layer. All the simulations were performed at zero bias field and temperature.

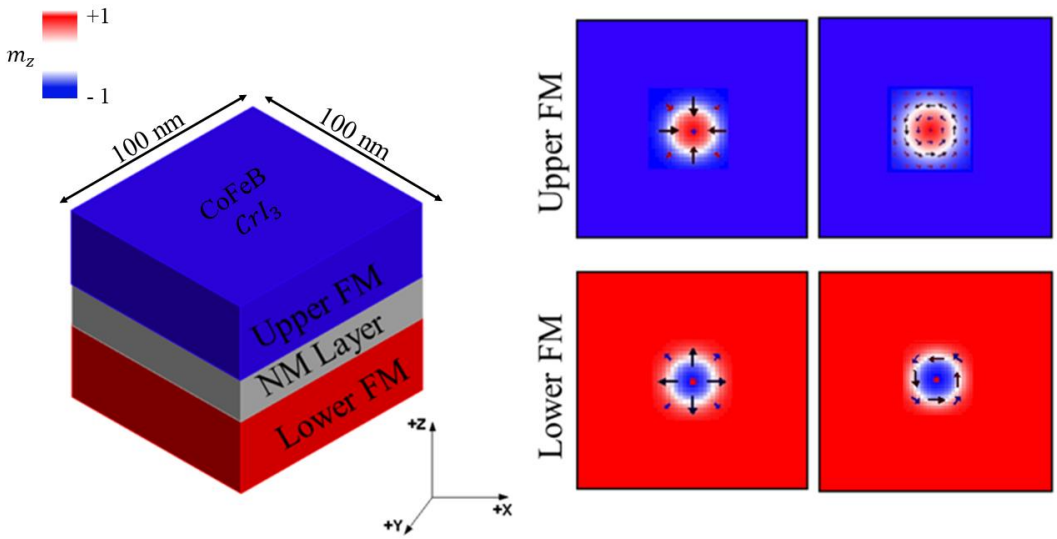

Figure 3.5 3D sketch of the 100 nm × 100 nm square sampled SAF multilayer under investigation, where it is composed of two ferromagnets (upper FM & lower FM) separated by a non-magnetic layer. On the left snapshots representing examples of the spatial distribution of the magnetization for SAF Néel and Bloch skyrmions in the upper and lower FMs respectively.

3.3.1.2 Sample Properties

We considered two materials in our simulations: *CoFeB* and a 2d CrI_3. The material parameters used in simulations are detailed in **Table 3.1** for *CoFeB* and CrI_3. For the skyrmion-hosting samples, we analyze a circular geometry with diameter from d = 100 nm to 500 nm as well as a 100 nm × 100 nm square (**Fig. 3.5**). The thickness was set to t_{FM} = 0.31 nm. The discretization cell used in both geometries is 1 nm ×1 nm × 0.31 nm.

Parameters	**CoFeB**		**CrI_3**	
Type	Bloch Skyrmion	Néel Skyrmion	Bloch Skyrmion	Néel Skyrmion
Ms(kA/m)	900	900	68.781	68.781
A(pJ/m)	20	20	1.21	1.21
K_u(MJ/m^3)	0.8	0.8	0.317	0.317
$\|D\|$(mJ/m^2)	[1.5, 3.0]	[1.5, 3.0]	[0.60,0.77]	[0.59,0.78]

Table 3.1 Micromagnetic parameters of CoFeB and CrI_3 used for simulating Néel and Bloch skyrmions, for both square and circular geometries.

3.3.1.3 Thiele Equation

The core-translation of topological textures can be captured by a particle-like behavior which is well described in terms of the Thiele formalism [133,134] In the Thiele formalism, we assume that the magnetization evolves adiabatically such that at all instants the full magnetization is uniquely defined by the position of the topological texture core, i.e. **m**(**x**,t) = **m**(**x**|$X(t)$,$Y(t)$) where $X(t)$ and $Y(t)$ are the position of the soliton core. Hence, the time-evolution of the magnetization is described as **m**(x,t) = **m**(**x**-Vt) , where $\mathrm{V}(t) = \dot{X}(t)\mathbf{x} + \dot{Y}(t)\mathbf{y}$, for any soliton. Within these assumptions, we can integrate the LLG **Eq. (2.20)** and obtain,

$$\overleftrightarrow{G} \times \mathbf{v} - \alpha_G \overleftrightarrow{D}\mathbf{v} + \mathbf{F} = 0 \qquad (3.6)$$

Where,

$$\left(\overleftrightarrow{G}\right)_{ij} = \varepsilon_{zij}\int \mathbf{m}\cdot\left(\partial_x\mathbf{m}\times\partial_y\mathbf{m}\right)d^2x = 4\pi Q\varepsilon_{zij} \qquad (3.7)$$

$$\left(\overleftrightarrow{D}\right)_{ij} = \int\left(\partial_i\mathbf{m}\cdot\partial_j\mathbf{m}\right)d^2x \qquad (3.8)$$

$$\mathbf{F} = -\frac{1}{\mu_0 M_s{}^2 t}\nabla E \qquad (3.9)$$

Here, Q is the topological charge and is independent of the precise shape of the magnetization configuration. $Q = \pm 1$ for skyrmions and $Q = \pm 0.5$ for vortices according to the soliton polarity. Moreover, ε_{ij} is the antisymmetric tensor with $\varepsilon_{xyz} = 1$, and E is the total free energy. $\vec{\vec{G}}$ and $\vec{\vec{D}}$ are called gyrotropic and viscosity tensors, respectively. The gyrotropic tensor $\vec{\vec{G}}$ produces a motion perpendicular to the applied force and depends only on the topological charge of the soliton [19,133–137]. In the case of the RKKY coupled system, the two solitons have opposite topological charge, and thus, the collective soliton experiences the motion corresponding to zero topological charge[125]. Thus, the net velocity of the collective solitons has no component perpendicular to the force. The viscosity tensor $\vec{\vec{D}}$ produces a motion along the direction of the force, leading to a minimization of the total free energy E. **Eqs. (3.7-3.8)** depends on the exact ansatz of the soliton with the major contributions coming from the vicinity around the soliton core, where the magnetization is not in plane and has a non-vanishing gradient. The spatial dependence of the total free energy E (see **Eq. (3.8)**) may be due to edge repulsion and material inhomogeneities.

3.3.2 Stability Results

In this section, we perform static simulations to obtain the DMI range for the stability of the skyrmions. This range of DMI will be employed as a linear gradient for the skyrmion manipulation.

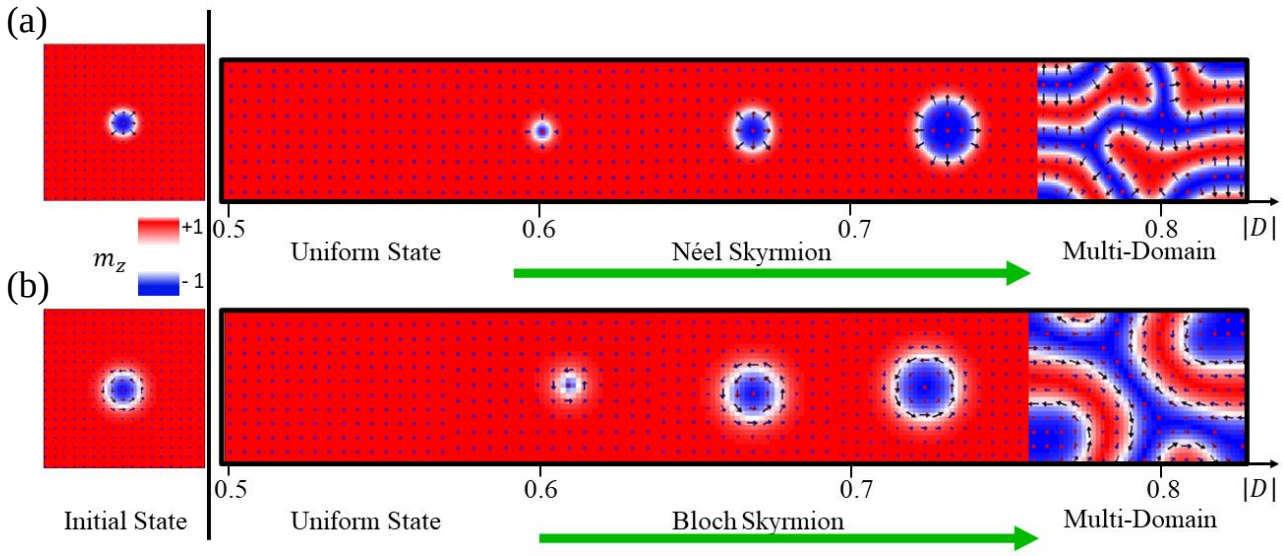

Figure 3.6 Equilibrium configurations of the magnetization of the 2d CrI_3 material as a function of DMI constant |D| at zero external field with the initial configuration being (a) Néel skyrmion, and (b) Bloch skyrmion. The colors refer to the z-component of magnetization (blue negative, red positive).

Magnetic skyrmions stabilization is well-known in thin-film and occurs in the absence of external magnetic fields by the interplay of exchange, DMI, uniaxial anisotropy and magnetostatic fields. It has been shown that isolated skyrmions are metastable states for a range of DMI given by ~0.5 $D_c < D < D_c$ where $D_c = 4\sqrt{A\left(K_u - 0.5\mu_0 M_s^2\right)}\Big/\pi$ [54]. In the thin film approximation, this range is mostly independent of the DMI type, bulk or interfacial. For the *CoFeB* values in **Table 3.1**, we obtain D_c = 3 mJ/m^2, while for CrI_3 we obtain D_c = 0.78 mJ/m^2. These theoretical predictions were corroborated by the static micromagnetic investigation as shown in the stability ranges in **Table 3.1**. **Fig. 3.6** shows that for 2d CrI_3 material, Néel skyrmions (**Fig. 3.6(a)**) are stabilized at 0.59 mJ/m^2 ≤ |D| ≤ 0.78 mJ/m^2, however below this range the configuration will turn into uniform state, and above it a multi-domain configuration will be observed. For the Bloch skyrmion (**Fig. 3.6(b)**), stability is detected for 0.60 mJ/m^2≤|D|≤ 0.77 mJ/m^2. These ranges are independent of the sample geometry. The reason is that skyrmions are localized textures and are not affected by edge effects when they are much smaller than the sample and far from the edges.

3.3.3 Dynamics Results

In this section, we performed micromagnetic simulations considering gradients of DMI within the range of stability of the magnetic solitons in the respective samples, as obtained in **Section 3.3.2**. We fix the minimal and maximal values of the DMI as the values at the edge of the sample and consider a linear gradient along the x-direction of the sample.

The motion of Néel skyrmions under effect of iDMI gradients have been already analyzed in the literature with parameters like the ones considered here for *CoFeB* [54,125,135]. For this reason, we focus on the 2d material CrI_3 and analyze both Bloch and Néel skyrmion dynamics induced by the linear gradient of bDMI and iDMI, respectively (see **Figs. 3.7(a)-(b)** below).

We start from a single layer CrI_3, which reveals a ferromagnetic behavior [130,131]. For the chosen K_u and M_s, the Néel and Bloch skyrmions move with positive velocities in the x- and y-directions. Along the x-direction, it moves towards a higher DMI value, while the motion along the y-direction is given by the Magnus force [125]. This agrees with the Thiele equations for skyrmions [125,136]. The damping coefficient α_G is responsible for the motion towards a lower energy state, corresponding to a higher DMI. Hence, in the simulations, we notice that a higher damping constant is associated to a higher component of the velocity along the linear gradient.

We proceed to consider a CrI_3 with two layers, which coupled antiferromagnetically [130,131] and can be modeled as a SAF [132]. In the SAF CrI_3, two skyrmions of opposite topological charges are antiferromagnetically coupled via the interlayer exchange coupling. This coupling leads to a zero net Magnus force and a suppression of the skyrmion Hall effect [132] which results in a straight motion along the gradient direction (**Figs.**

3.7(c)-(d)). The observed behaviors agree with the Thiele formalism developed in **section 3.3.1.3** by employing the skyrmion ansatz as described in Ref. [125].

We conclude that the skyrmion Hall angle in 2d CrI_3 depends on the number of layers, and it is present for an odd number of layers but vanishes for an even number of layers.

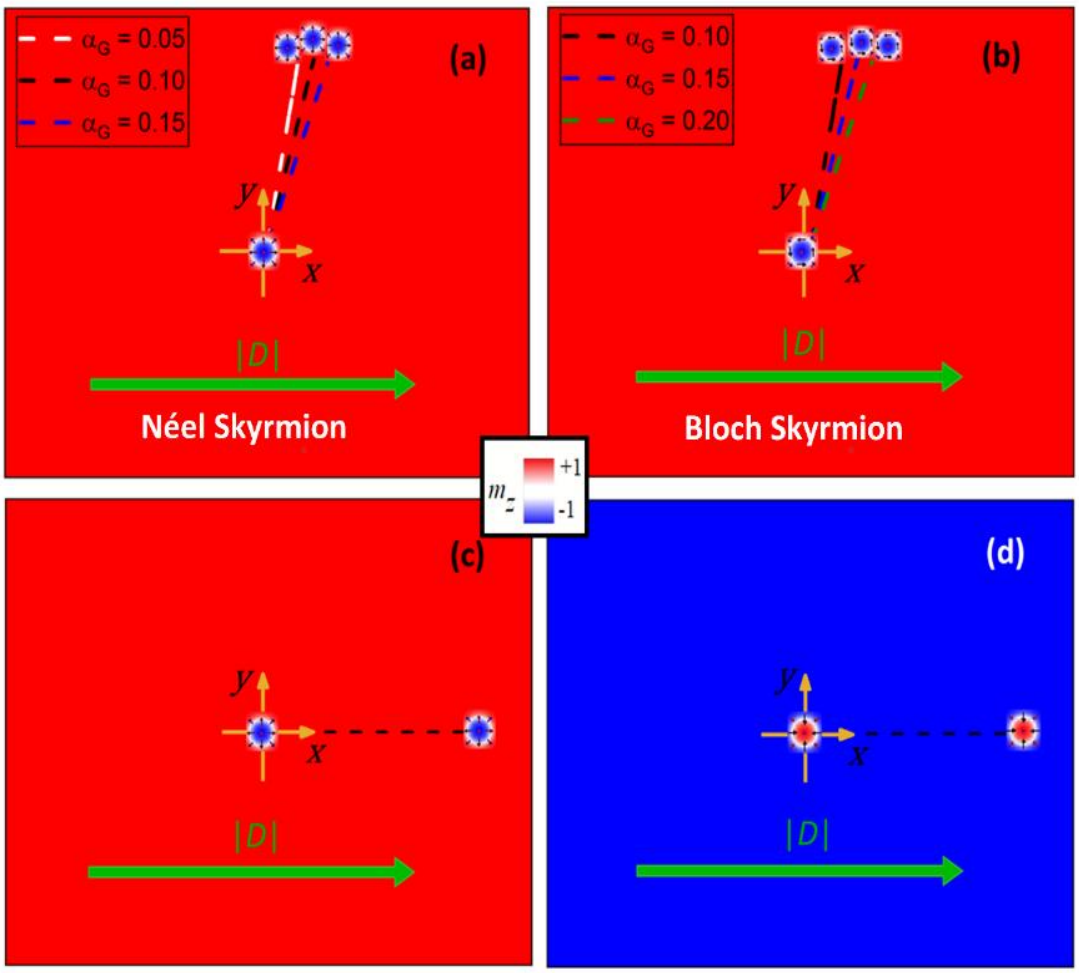

Figure 3.7 Micromagnetic simulations results of the (a) Néel skyrmion trajectory under a linear iDMI gradient (0.59 mJ/m^2 ≤ D ≤ 0.78 mJ/m^2, see **Table 3.1**), and (b) Bloch skyrmion trajectory under a linear bDMI gradient (0.60 mJ/m^2≤D≤ 0.77 mJ/m^2 directed along the positive x-direction as shown in green arrow in a single CrI3 layer as a function of different damping coefficients. (c) – (d) Top and bottom layer of the SAF CrI_3, respectively, where the straight trajectory of the skyrmion is also indicated. The color bar denotes the out-of-plane magnetization component m_z: red positive, white zero, and blue negative.

3.4 From Skyrmions to Hopfions

In this section we provide a brief introduction about hopfions, their topological nature, and their dynamics equations. We also present a comprehensive study using numerical methods for the stability, current driven, and gradient-driven dynamics of Néel-type hopfions under the influence of IDMI gradients in a strip like sample.

3.4.1 Introduction to Hopfions

Exotic magnetic structures are knots in continuous physical fields classified by non-zero Hopf index values. Low-dimensional topological soliton like textures in ferromagnetic (FM) and antiferromagnetic (AFM) materials, such as 1D magnetic domain walls, 2D magnetic vortices, and 2D magnetic skyrmions, have been extensively studied in recent years. When mapped to 3D physical fields, 3D topological solitons, called "hopfions", are true pearls of mathematics and topology, and physics. To understand such transformation from 2D to 3D solitons try to imagine a point like 2D skyrmion as shown in **Fig.3.8(a)** that will become a line vortex in 3D space (**Fig.3.8(b)**).

While single skyrmions can propagate freely in 2d space, hopfions can propagate in all three spatial directions, where this third dimension will not only open new opportunities in magnetic materials due to additional levels of complexity or phenomena that can only exist in 3D, such as chirality, but will also yield substantial challenges for the synthesis, theory, and characterization of such artificially designed 3D systems [137].

Moreover, contrary to chiral magnetic skyrmions requiring materials with strong spin-orbit interaction in combination with a lattice lacking inversion symmetry the materials requirements for the existence of magnetic hopfions are much weaker [138]. Distinct from 2D ferromagnetic skyrmions, hopfions have a vanishing gyrovector.

The existence of 3D topological solitons with stringlike properties was first proposed by Ludvig D. Faddeev [139] as a limit of the Skyrme model [140]. Hopfions have been observed experimentally in Ir/Co/Pt nanodisks of multilayers using X-ray magnetic circular dichroism in the presence of strong DMI and out-of-plane magnetic anisotropy [141] and in the polarization of free-space monochromatic light [142]. However, nucleation and stabilization dynamics of hopfions have been studied in chiral magnets [143–145] and chiral ferromagnets [146] with a tunable Dzyaloshinskii–Moriya interaction (DMI). In ferromagnetic materials, there exist two types of hopfions: Bloch-type [144,145,147] which can be excited in the presence of bulk DMI and Neel-type hopfions [148] which can be excited in the presence of interfacial DMI.

Hopfions dynamics has been studied in different conditions including, presence of external field [149], interfacial magnetic anisotropy (PMA) [144,145], current driven dynamics via spin transfer torque (STT) and spin hall torque (SHT) [148], higher-order exchange interaction [138].

The dynamics of hopfions are so promising starting point for neuromorphic computing applications, where its motion under different gradients can mimic behavior of synaptic utilities. This may be due to several reasons:

i. Both entities process and transmit information. As neurons are the basic units of information processing in the nervous system, transmitting electrical signals through synaptic connections. Similarly, Hopfions can encode and process information through their dynamic motion and interactions with neighboring magnetic structures.

ii. Hopfions and neurons exhibit dynamic behavior. Neurons can adapt their firing rates and synaptic strengths in response to external stimuli, enabling learning and memory functions. Hopfions also display dynamic motion and can respond to external stimuli such as magnetic fields or currents, allowing for the modulation of their properties and interactions.

iii. Both Hopfions and neurons possess a level of topological stability. In the case of Hopfions, this stability arises from the topology of their magnetic structure, while neurons maintain stability through their structural integrity and membrane properties.

iv. Both Hopfions and neurons operate with relatively low energy consumption. Neurons efficiently transmit and process information using electrochemical signals, while Hopfions can undergo motion with low-energy stimuli such as magnetic fields or currents.

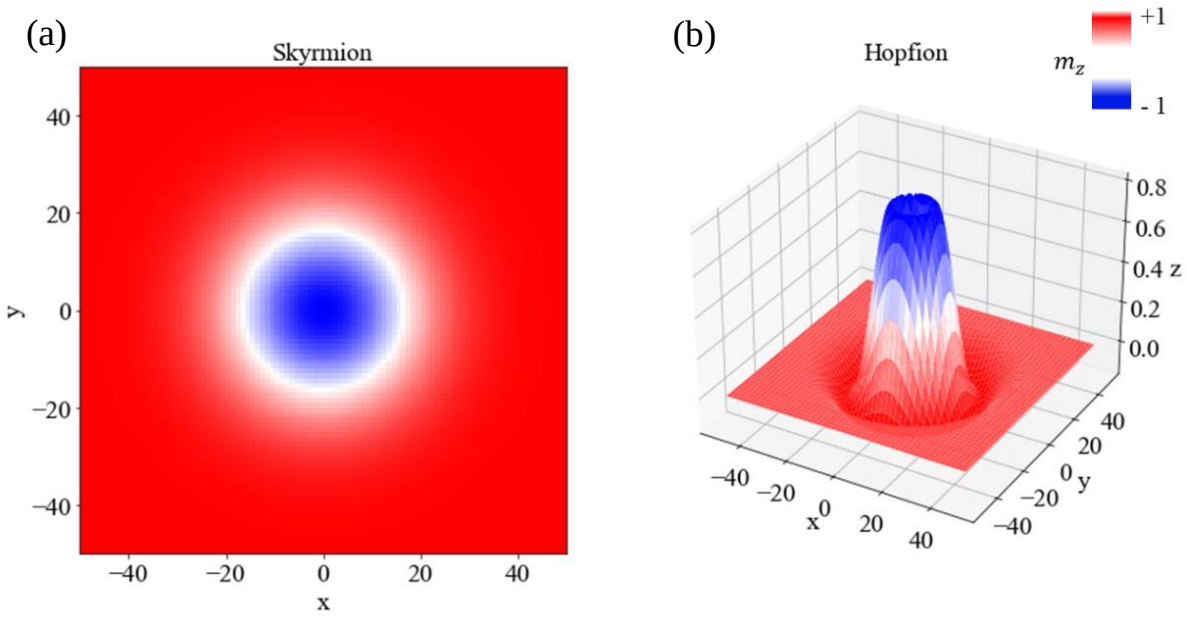

Figure 3.8 Transition from a (a) skyrmion in the x-y plane to a (b) hopfion in the x-y-z space by transforming the magnetization configuration from a localized spin texture with a circular core (skyrmion) to a twisted, three-dimensional structure with a central vortex-like core (hopfion).

3.4.2 Topology and Hopf Number

A hopfion is a topologically nontrivial magnetic texture characterized by a swirling pattern of magnetization in three-dimensional space. It is characterized by a non-zero Hopf charge, which is a topological invariant that quantifies the winding of the magnetization field around a closed loop enclosing the hopfion. The mathematical description of a Hopf. Charge is given by,

$$H = \frac{1}{(8\pi)^2} \int \boldsymbol{F} \cdot \boldsymbol{A}\, d\boldsymbol{r} \quad (3.10)$$

Where $\boldsymbol{F}$ and $\boldsymbol{A}$ are vector fields calculated from the unit vector field $\boldsymbol{n}$ by,

$$F_i = \epsilon_{ijk} \boldsymbol{n} \cdot (\nabla_j \boldsymbol{n} \times \nabla_k \boldsymbol{n}) \text{ And } \nabla \times \boldsymbol{A} = \boldsymbol{F} \quad (3.11)$$

With ϵ being the Levi-Civita tensor, $\boldsymbol{A}$ the vector potential, and $\boldsymbol{n}$ corresponds to the unit microspin. The Hopfion number, also known as the Hopf invariant, is directly related to the Hopf charge and quantifies the topological complexity of the hopfion. **Fig. 3.9** shows that for a first-order hopfion, the hopfion number is *H*=1, indicating a single unit of topological winding. For a second order hopfion, the hopfion number is *H*=2, indicating a higher degree of topological winding.

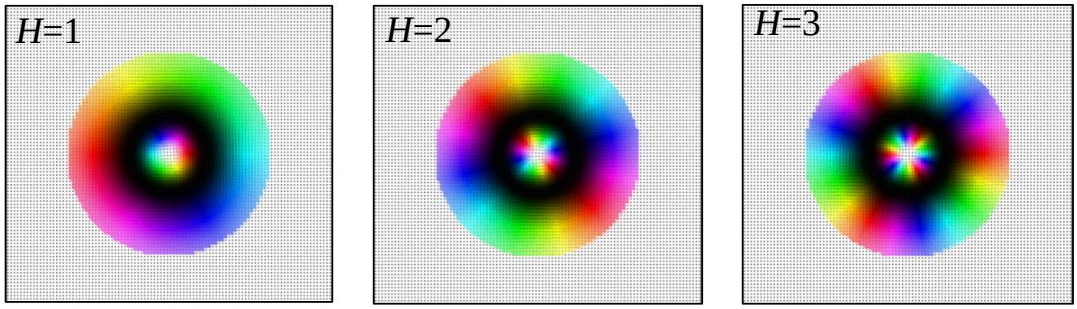

Figure 3.9 Illustration of hopfion with different Hopf number, H=1, H=2, H=3.

3.4.3 Modeling and Sampling

This section is divided into 3 subsections, where we present the sample, we are simulating, the magnetic properties of our sample, the Thiele's equations governing the motion of the skyrmions, as well as the results.

3.4.3.1 Model and Sample Properties

We considered the ground state Néel hopfion to perform micromagnetic computations with the, PETASPIN solver [64,65] that numerically integrate the Landau-Lifshitz-Gilbert (LLG) equation given by **Eq. (2.20)**, while the total energy density of the system is given by **Eq. (2.14)**. Looking at **Fig. 3.10**, we considered a *FeGe* rectangular strip, with L = 320 nm, W = 64 nm, and thickness t_{FeGe} = 8 nm. We sandwiched the *FeGe* layer by two PMA layers with an anisotropy constant of $K_u = 10^6$ J/m^3, which can be experimentally created by oxide or heavy metal layers. The thickness of each capping layer is t_{PMA} = 2 nm. The *FeGe* magnetic parameters used in our simulations are, the iDMI = 1×10^{-3} J/m^2, the exchange stiffness $A_{ex} = 1.1\times10^{-12}$ J/m, the uniaxial anisotropy constant $K_u = 1\times10^3$ J/m^3, and the saturation magnetization $M_s = 3\times10^5$ A/m. An external field H_{ext} = 100 mT is applied along the -z direction.

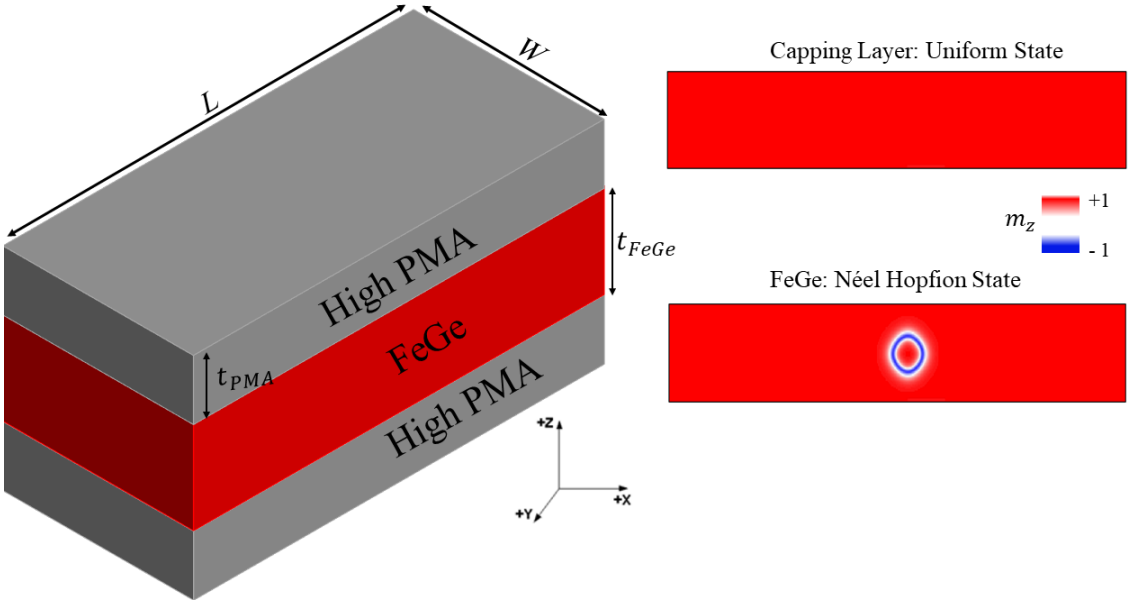

Figure 3.10 Illustration of the 360 nm × 64 nm rectangular strip stack composed of two capping layers characterized by high PMA each with thickness t_{PMA}, sandwiching a *FeGe* layer with thickness t_{FeGe}. On the left snapshots representing examples of the spatial distribution of the uniform magnetization in the external layers and a Néel hopfion state in bulk.

3.4.3.2 Thiele's Formalism

Disregarding deformations, the motion of a hopfion, as a rigid body, is governed by Thiele's equation,

$$\frac{\gamma}{M_s}T + G \times (v - u) - \vec{D} \cdot (\alpha v - \beta u) = 0 \quad (3.12)$$

where γ is the gyromagnetic ratio; α is the Gilbert damping; β is the STT nonadiabaticity [150]; **v** is the velocity of the hopfion; $\mathbf{u} = -\mu_B p\mathbf{J}/[eM_s(1+\beta^2)]$ is a vector with dimension of velocity proportional to the current density **J**, in which p is the spin polarization and e is the electron charge; **G** is the above-mentioned gyrovector; and $\vec{\vec{D}}$ is the dissipation tensor defined as $D_{ij} = \int \partial_i \mathbf{m} \cdot \partial_j \mathbf{m}\, dV$. **T** is the force on the hopfion, expressed as $T_i = -(\partial \int \mathcal{F}\, dV/\partial X_i) - \int (\partial \mathbf{m}/\partial x_i) \cdot (\mathbf{m} \times \tau)\, dV$, where $\mathcal{F}$ is the free-energy functional, X_i is the center position of the hopfion, and $\boldsymbol{\tau}$ represents nonconservative torques other than STT such as the SHT. In our model, all the material parameters are spatially homogeneous; therefore, the first term in T is 0. Since G = 0, the hopfions move along the applied current via STT with velocity,

$$\mathbf{v} = \frac{\beta}{\alpha}\mathbf{u} \qquad (3.13)$$

Considering the thiele's equation **Eq (3.12)**, in the absence of applied current, and concentrating on the effect of iDMI gradient, then **u** = 0 and thus **Eq. (3.12)** will reduce to,

$$\frac{\gamma}{M_s}T + G \times (v) - \vec{D} \cdot (\alpha v) = 0 \qquad (3.14)$$

As a fact of continuous deformation, **G** = 0 applies to all the hopfions, thus the hopfions move along the direction of iDMI gradient. The formula of **v** then becomes, $\mathbf{v} = \gamma T/M_s \alpha D$ with $T = (\partial E/\partial D_i)(\partial D_i/\partial x)$ with $E = -c_D g_D X$ (free energy due to DMI), and D_i is the linear DMI gradient along x direction given as, $D_i(x) = g_D x$. The velocity become,

$$\mathbf{v} = \frac{\gamma c_D g_D}{M_s \alpha D} \qquad (3.15)$$

3.4.4 Dynamics Results

A systematic study was performed on a Néel hopfion, first under the effect of STT, and later under the influence of DMI gradient.

3.4.4.1 STT Driven Dynamics

Fig. 3.11(a) below shows the trajectory during a period of 50 ns of the Néel -type hopfion driven by STT with J = 10^7 A.cm^{-2}, p = 0.8, α = 0.1 and β = 0.2, obtained by numerically solving the Landau-Lifshiz-Gilbert (LLG) equation considering the adiabatic and non-adiabatic STT terms as given in **Eq. (2.25)**. The trajectory is almost along the x direction, where the hopfion change position from (x = 160, y = 32) to (x = 310, y = 32) The small deformation of the hopfion size may come from the discretization near the boundaries. According to **Eq. (3.13)**, the velocity of the hopfion along the x direction $\mathbf{v}_x$ seems to proportionally increase as the applied current density increases as shown in **Fig. 3.11(b)**.

The numerical data from LLG simulations (red circles) are in good agreement with the analytical formula (black line). Above J = 5 × 10^7 A m^{-2}, the hopfion is destroyed.

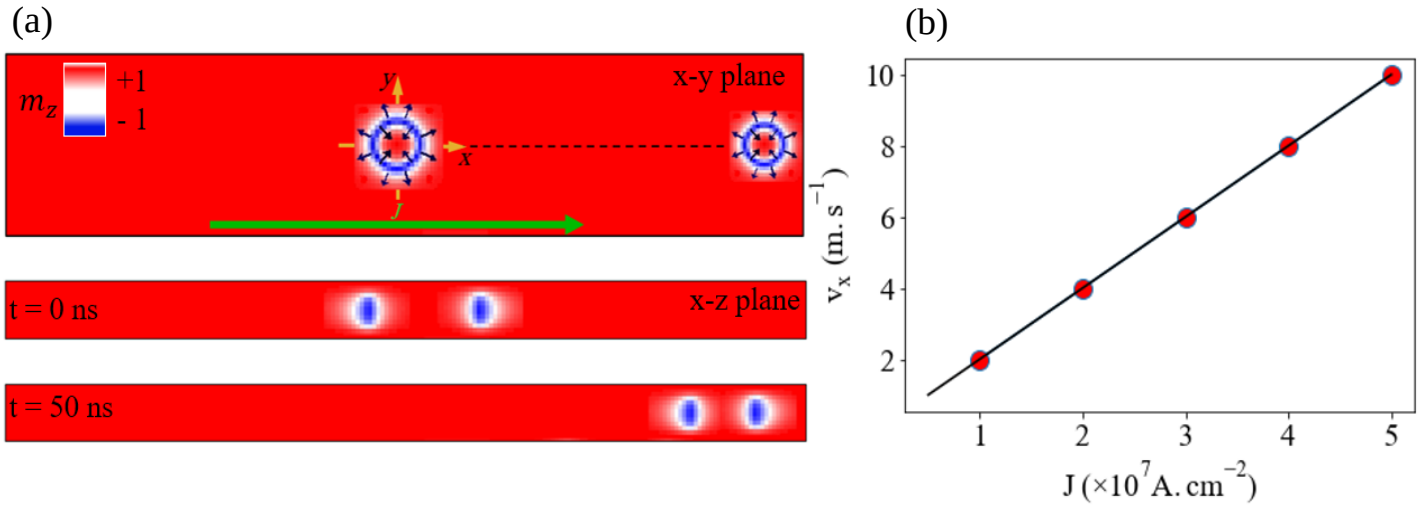

Figure 3.11 (a) Trajectory of Néel hopfion driven by STT during a period of 50 ns, along the x-y plane (upper panel) and the x-z plane (lower panel). (b) Current density J dependence of the longitudinal velocity $\mathbf{v_x}$ of the Néel hopfion. The red circles are numerical results for STT-driven motion. The solid line is theoretical prediction.

3.4.4.2 DMI Driven Dynamics

In this part we neglect the STT effect, and we remove the applied external field. The aim here is to consider only the effect of the iDMI gradient.

As a first step we get the stability iDMI domain to be 0.95 mJ/m^2 ≤ D ≤ 1.02 mJ/m^2, where **Fig. 3.12(a)** shows that below this domain (i $|D|$ = 0.94) a skyrmion like behavior is observed and above it (iv $|D|$ = 1.05) hopfion is destroyed. Considering an iDMI gradient enclosed within the stability domain along the +x direction, the Néel hopfion moves along the direction of applied gradient as expected by thiele's formalism (**section 3.4.3.2**), as shown in **Fig. 3.12(b)** along the x-y plane (upper panel) and the x-z plane (lower panel). Unlike the case of STT dynamics, here no deformations will appear at the boundaries.

The velocity of the hopfion $\mathbf{v}_x$ given by **Eq. (3.15)**, seems to increase linearly with increasing DMI constant (D). The Néel hopfion seems to move with higher velocity under the influence of STT, and this may go back to the fact that the stability of hopfion in presence of DMI is limited into a narrow domain. The result may also depend on the considered magnetic parameters, geometry, and magnetic materials.

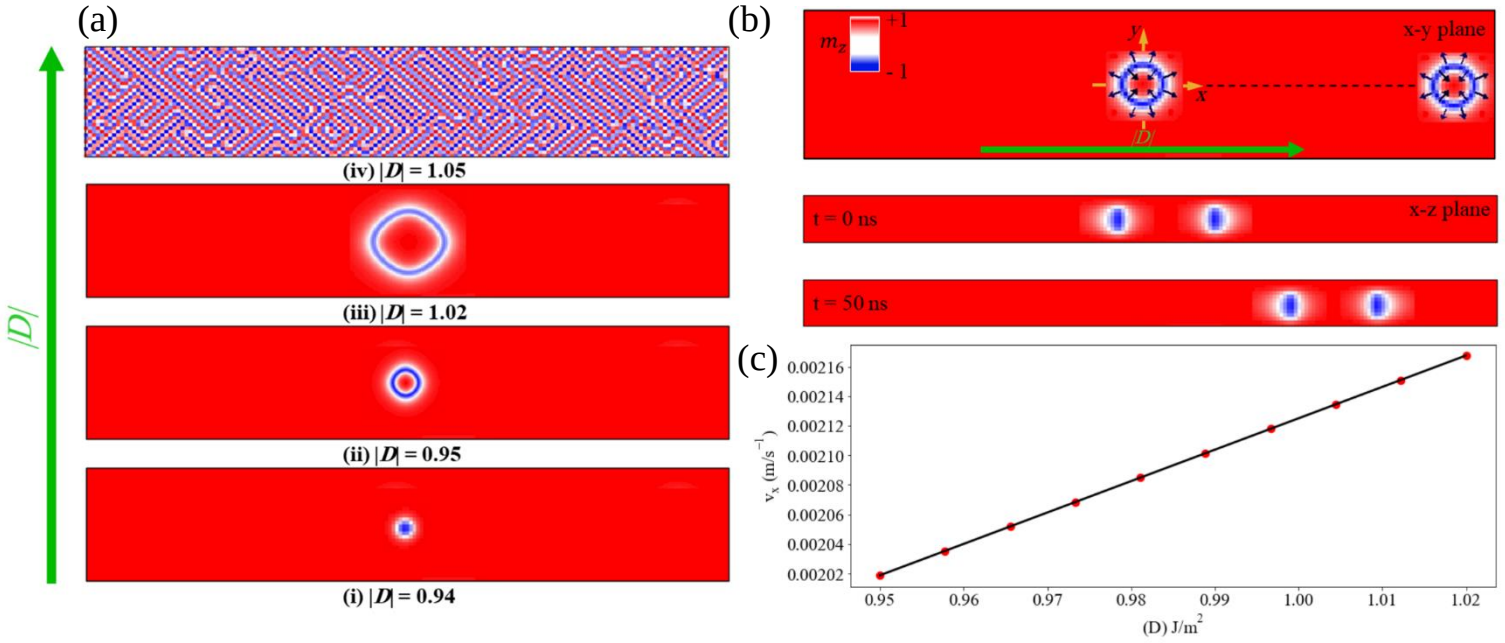

Figure 3.12 (a) Micromagnetic simulations results of the equilibrium configurations of the magnetization as a function of |D|. (b) Trajectory of Néel hopfion driven by DMI gradient for 50 ns, along the x-y plane (upper panel) and the x-z plane (lower panel). (c) Velocity v_x of the Néel hopfion under the influence of DMI constant (D (J/m^2)).Numerical results (red circles), coincides with theoretical predictions (black line).

3.5 Conclusion

In summary, we performed a systematic study of the effect of linear DMI gradient on skyrmions (Bloch and Néel types) motion in a *CoFeB* thin-film and a 2d CrI_3 through micromagnetic simulations and Thiele's equation. Our results showed that stabilization of these magnetic configurations can take place for specific intervals of DMI (depending on the sample geometry) at zero external field. Under the effect of a linear iDMI gradient, skyrmions move with a damping-dependent trajectory in a single-layer *CoFeB* and 2d CrI_3, while a zero skyrmion Hall angle motion was observed in the SAF *CoFeB* and CrI_3. We observed that in 2d materials the DMI domains required for the self-generated dynamics of skyrmions are much smaller than that in case of thin-film material. This suggests alternative means for low-power manipulation of magnetic solitons in 2d materials.

For Néel hopfion, we studied the dynamics under the effect of STT and iDMI gradient, in a system composed of *FeGe* material. We realized that DMI will not provide a wide stability range thus causing the dynamics to be very slow compared to the case of STT driven dynamics.

Chapter 4

Magnetic Vortices

The future of computer memory is in a vortex

Michael Byrne

“I find the magnetic vortex to be a mesmerizing phenomenon, a whirlwind of invisible forces sculpting the fabric of space with its silent dance.”

The fourth chapter is dedicated for exploring magnetic vortices. Section 4.1 delves into the key concepts of the magnetic vortices and shows its different configurations. Section 4.2 is divided into three subsections which focus on the manipulation and dynamics of magnetic vortices. Section 4.3 provides a brief conclusion.

4.1 Introduction to Magnetic Vortices

Vortices are a usual phenomenon in Nature: everyone who has seen a tornado, or the water flow pattern in the bathtub drain, may have an idea of what a vortex is. These are examples of a vortex in a fluid (air or water), and they have in common a characteristic flow, which forms a "curling" pattern in the velocities field. Vortices can appear as a particular curling pattern in other continuous media (e.g., the gravitational field in the case of a spiral galaxy, the electromagnetic field in the case of an optical vortex, the density field in a superfluid like Helium, etc.) [151].

Magnetic vortex is a typical ground state of nanoscale soft magnetic disk [152], which is characterized by its polarity *p* and chirality *c*. The former one refers to the direction of the vortex core, being either upward (p=+1) or downward (p=-1). The latter is linked to the rotation of the in-plane magnetization around the vortex core, which can be clockwise (c=-1) or counterclockwise (c=+1). It has a non-integer Skyrmion number S ($0.5 < |S| < 1$) due to both the vortex core polarity and the magnetization tilting induced by the IDMI boundary conditions. To distinguish different types of vortices, we call the vortex with clockwise (or counterclockwise) chirality circular vortex (**Fig. 4.1(a)-(b)**) or radial (**Fig. 4.1(c)**) if the chirality is outwards (or inwards) [128,153]. The magnetic radial vortex has become a research hotspot due to its better thermal stability and lower driven current density. The behavior of radial vortex has been extensively studied under the influence of high iDMI.

Although, the structure of magnetic vortex core has been predicted long before in theory, the experimental observation only appears recently [154,155]. One experiment among the first observations of magnetic vortex core is just done in the circular dots of Permalloy, (Shinjo, 2000) which was prepared with the help of nanotechnology. They use magnetic force microscopy (MFM) to detect the core of the magnetic vortex. As the core has perpendicular magnetization, while the magnetization vector out of the core parallel to the plane, thus, the force between the cantilever tip and the surface of the core is different from the force between the cantilever tip and the surface of out-of-core.

Later, different approaches were followed to manipulate and stabilize magnetic vortices. This includes magnetic anisotropy [153], magnetic field gradients [156], spin transfer torques and DMI interactions [128].

Due to its polarity feature, magnetic vortices are promising candidates in memory and sensors devices [157,158]. Moreover, it was possible to address various promising medical applications based on magnetic vortex [159,160]. Synchronization between multiple vortex-based nano-oscillators showed impressive outcomes for the future of non-conventional computing. One interesting application in this regard is the magnetic anisotropy-controlled vortex nano-oscillator designed for neuromorphic computing [161].

In this study they performed micromagnetic simulations to synchronize six vortex nano-oscillators, wherein the synchronization state can be modulated by the spin-polarized current and magnetic anisotropy. They tried to explore the ability of coupled vortex nano-oscillators to work as a model system for neuromorphic computing.

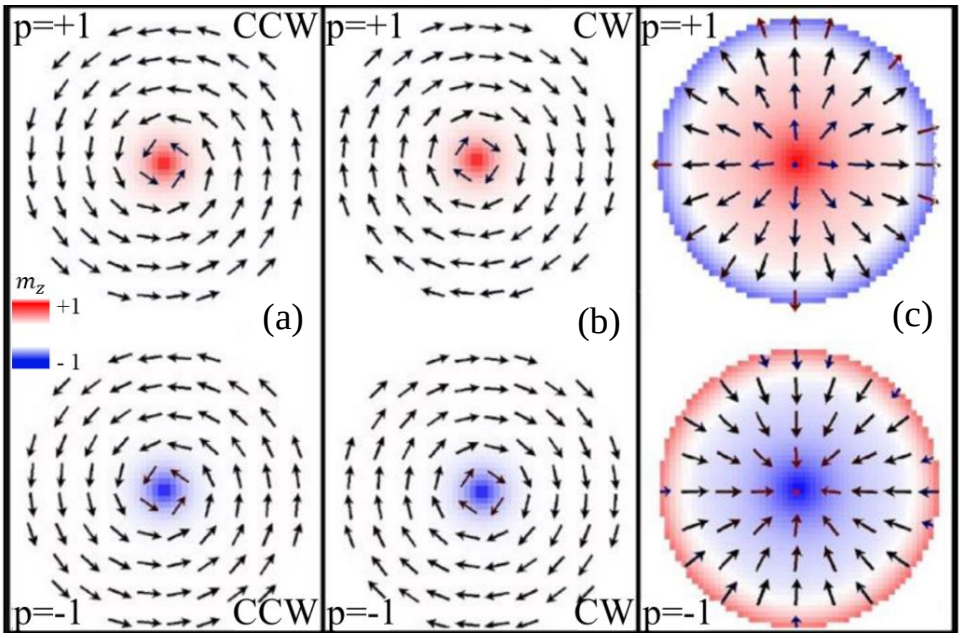

Figure 4.1 Spatial distribution of magnetization for different types of vortices with positive (top) and negative (bottom) polarities. (a) Counterclockwise (CCW) circular vortex. (b) Clockwise (CW) circular vortex. (c) Radial vortex. A color scale linked to the out-of-plane component of the magnetization is also shown (red positive, blue negative).

4.2 Manipulation of Magnetic Vortices Under DMI Gradient

In this section, we present a comprehensive study using numerical and analytical methods of the stability and gradient-driven dynamics of radial and circular vortices under the influence of DMI gradients in different geometries (circular and rectangular samples) and two materials (thin film *CoFeB* [128] and 2d CrI_3 [129]). A theoretical analysis was carried out via systematic micromagnetic simulations and corroborated by the Thiele's formalism.

4.2.1 Modelling and Sampling

As in **Chapter 3**, the micromagnetic computations were performed with a state-of-the-art micromagnetic solver, PETASPIN [63].

For vortices, we only consider the effect of iDMI. In vortices-hosting samples, we consider circular geometry with diameter from d = 100 nm to 500 nm as well as a strip with dimensions 1500 nm × 250 nm. The thickness was set to t_{FM} = 1 nm. The discretization cell used in both geometries is 5 nm x 5 nm x 1 nm. The same results are obtained with a thickness of 0.31 nm and a discretization cell 1 nm x 1 nm x 0.31 nm. We also simulated a SAF for each of the two materials (*CoFeB*, CrI_3), composed of two ferromagnets separated by a non-magnetic layer with thickness 2 nm for *CoFeB* and 0.62 nm for CrI_3.

Parameters	**CoFeB**		**CrI_3**	
Type	Radial Vortex	Circular Vortex	Radial Vortex	Circular Vortex
Ms(kA/m)	1000	1000	68.781	68.781
A(pJ/m)	20	20	1.21	1.21
K_u(MJ/m^3)	0.5	0.5	0.0*	0.0*
$\|D\|$(mJ/m^2)	[1.67, 2.0] (rectangular) [1.7, 2.3] (circular)	[0, 0.8] (rectangular) [0, 1.1] (circular)	[0.045, 0.070] (rectangular) [0.040, 0.090] (circular)	No DMI range (rectangular & circular geometries)

Table 4.1 Micromagnetic parameters of CoFeB [128] and CrI_3 used for simulating radial and circular vortices [129]. The value of the anisotropy of CrI_3 can be tuned as shown in Fig. 1(c) of Ref. [162].

4.2.2 Stability Results

In this section, we perform static simulations to obtain the DMI range for the stability of the radial and circular vortices. This range of DMI will be employed as a linear gradient for the vortex manipulation.

4.2.2.1 Radial Vortex

Magnetic vortices are non-local magnetic textures and, thus, are highly influenced by the sample geometry, boundary conditions, and their chirality (radial or circular). We observed in micromagnetic simulations that radial vortices are stabilized in both materials within a DMI range which depends on the geometry. In particular, the radial vortex is stabilized for circular dot diameters larger than 250 nm, as reported in the literature [128]. At a 500 nm diameter, the radial vortex is stable for 1.5 mJ/m^2 $\leq |D| \leq$ 2.1 mJ/m^2.

Fig.4.2 illustrates the stability of radial vortices as a function of D in the 1500 nm × 250 nm rectangular sample of *CoFeB* (**Figs. 4.2(a)-(f)**) and CrI_3 (**Figs. 4.2(g)-(l)**) i.e in the ranges 1.67 mJ/m^2$\leq |D| \leq$2.0 mJ/m^2 and 0.049 mJ/m^2$\leq |D| \leq$0.070 mJ/m^2 respectively.

We observe that the interplay of exchange, anisotropy and iDMI play an important role in the stability of vortices, that change according to the considered geometry (circular or rectangular). For the upper boundary of radial vortices, we find the transition to the helical

state, see **Figs. 4.2(f)**. Moreover, we notice that the range of iDMI for the radial vortex stability in CrI_3 is around 30 times smaller than in the *CoFeB.*

4.2.2.2 Circular Vortex

We noticed that circular vortices are stabilized only in the *CoFeB* thin film within a DMI range in agreement with the literature [128]. According to (**Fig 4.2(a)-(b)**), we notice that this range is 0.0 mJ/m^2≤ $|D|$ ≤0.8 mJ/m^2. No stabilization of circular vortices was detected in CrI_3 based on our micromagnetic parameters.

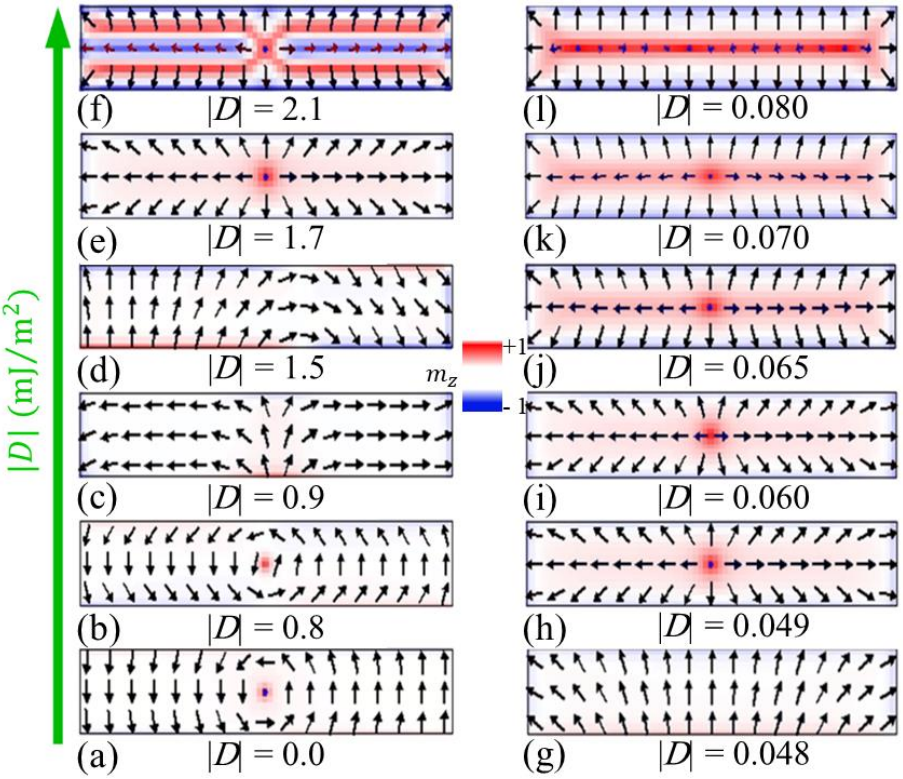

Figure 4.2 Micromagnetic simulations results of the equilibrium configurations of the magnetization as a function of |D| in (a) – (f) CoFeB and (g)-(l) CrI_3 rectangular strips.

4.2.3 Dynamics Results

In this section, we performed micromagnetic simulations considering gradients of iDMI within the range of stability of the magnetic vortices in the respective samples. We fix the minimal and maximal values of the iDMI as the values at the edge of the sample and consider a linear gradient along the x-direction of the sample.

4.2.3.1 Radial Vortex

Fig 4.3 (a)-(b) show the dynamics induced by the iDMI gradient on a single layer 1500 nm × 250 nm *CoFeB* and CrI_3 rectangular strips, respectively. In both materials, the vortex core exhibits a translational motion under the influence of the iDMI gradient. We notice that it moves towards the region of higher $|D|$, with a significant Hall angle. Similarly, to skyrmions, we notice that velocity depends on the damping coefficient, with smaller y-component for higher damping values. However, we observe a major difference: while a skyrmion moves mainly in the positive y-direction, a radial vortex tends to move mainly in the positive x-direction. This is ascribed to: (i) the topological charge of vortices is half of the skyrmion, and (ii) vortices are more influenced by sample boundary effects than skyrmions, since they are non-local textures.

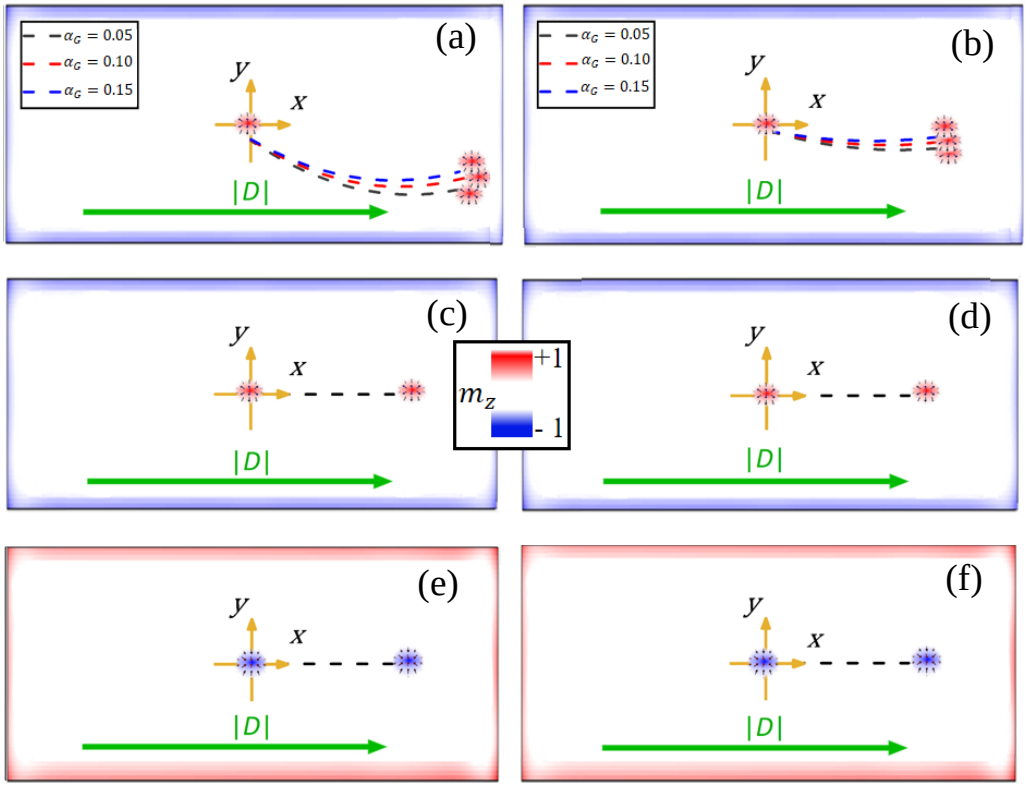

Figure 4.3 Micromagnetic simulations results of radial vortex trajectories under a linear iDMI gradient. In (a) and (b), a single 1500 nm × 250 nm FM rectangular sample under the effect of different damping coefficients in CoFeB and CrI_3, respectively, (c) and (d) in top layers and (e) and (f) in the bottom layers of the SAF composed of CoFeB and CrI_3, respectively.

In a SAF (either *CoFeB* or CrI_3 with an even number of layers), the radial vortex moves with a zero skyrmion Hall angle (**Fig. 4.3(c)-(f)**). However, the radial vortex travels faster in the case of CrI_3 (compare **Figs. 4.3(c), (e)** for *CoFeB* with **Figs. 4.3(d), (f)** for CrI_3 obtained within the same 250ns time interval). The same behavior is observed in a circular sample.

According to Thiele equations given in **Chapter 3** as **Eqs. (3.6-3.9)**, it is necessary to obtain the full magnetic configuration of the magnetic vortex. Previous studies have considered numerical approaches to compare to the micromagnetic simulations [134,162]. For simplicity, we assumed a radially symmetric configuration. The radial symmetry implies, $(\overleftrightarrow{D})_{xx} \approx \left(\overleftrightarrow{D}\right)_{yy} \approx D, (\overleftrightarrow{D})_{xy} \approx \left(\overleftrightarrow{D}\right)_{yx} \approx 0$.

A qualitative description of the vortex motion is shown in **Fig. 4.4**, which agrees with the simulation results of **Fig. 4.3(a)**. We considered both variations of the damping, and the DMI gradient as shown in **Figs. 4.4(a)-(b)** respectively.

Moreover, up to the lowest non-zero order, we can write the free energy of the vortex, due to the DMI gradient and the border repulsion, as $E = -c_D g_D X + kY^2$, where X, Y are the coordinates of the center of the vortex along the x and y directions. We also have that $c_D \approx \int d^2x \left[m_z \nabla \cdot \mathbf{m} - (\mathbf{m} \cdot \nabla) m_z \right]$ and $k \approx \frac{1}{2} \partial^2_Y \int d^2x \left(\mathbf{m} \cdot \mathbf{h}_{bound}(x, y, Y) \right)$ are constants, assuming that the magnetization $\mathbf{m}(x)$ is invariant of the position (we do not consider strong deformations of the texture as it moves) and $\mathbf{h}_{bound}(x,y,Y)$ represents the effective magnetic field due to boundary effects. Moreover, we assumed as the linear gradient of the iDMI parameter $D(x) = g_D x$. The Thiele equations of motion are,

$$\dot{X} = \frac{1}{\mu_0 {M_s}^2 t} \frac{-2\pi kY + \alpha_G c_D g_D \Gamma}{4\pi^2 + {\alpha_G}^2 \Gamma^2} \qquad (4.1)$$

$$\dot{Y} = -\frac{1}{\mu_0 {M_s}^2 t} \frac{2\pi c_D g_D + \alpha_G k \Gamma Y}{4\pi^2 + {\alpha_G}^2 \Gamma^2} \qquad (4.2)$$

We observe that, due to the DMI gradient, the vortex is pushed towards the bottom edge, while the dissipative term pushes it along the gradient. Additionally, edge repulsion tends to accelerate the vortex along the x-direction as it approaches the edge while forcing the vortex back to the center of the strip due to a small dissipative contribution.

As a remark, we notice that lower anisotropy tends to lower the velocity component along x and increase the component along y, while a lower iDMI gradient tends to decrease the velocity along x and along y.

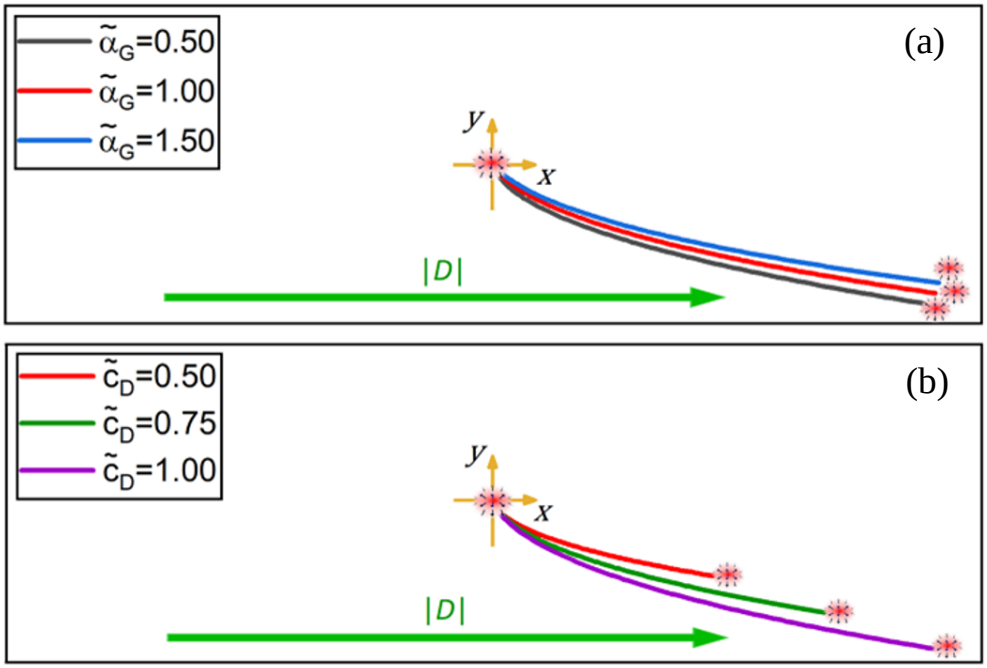

Figure 4.4 Motion of the radial vortex core in an iDMI gradient as obtained from the Thiele's equation. We considered here the Thiele description given by **Eqs. (3.6-3.7)**, for rescaled units for a qualitative description to be compared with the micromagnetic simulations in **Fig. 4.3(a)** away from the border. In (a)-(b), we show the motion for different values of rescaled Gilbert damping and iDMI gradient, respectively. We considered α_G and c_D as renormalized values for numerical simulations for a qualitative comparison.

4.2.3.2 Circular Vortex

We performed a similar analysis to observe the effect of the iDMI gradient on circular vortices, remarking that the circular vortex has not been found stable for the parameters of the 2d CrI_3 (**Table 4.1**). According to our observations, the circular vortex undergoes an expulsion dynamic under the influence of the linear iDMI gradient (**Fig. 4.5**). Since the circular vortex is not a stable magnetization configuration under any finite value of *D*, due to the damping, it decays to the uniform in-plane state [125]. This mechanism is interesting for application of spintronic devices as diodes [163,164]. Recently, it has been shown that the vortex core expulsion can be a mechanism driving an enhancement of sensitivity up to 80kV/W [104,165]. Thus, we envision that the recent discovery of voltage controlled DMI can drive additional enhancement of the performance of spintronic diodes by exploiting this behavior.

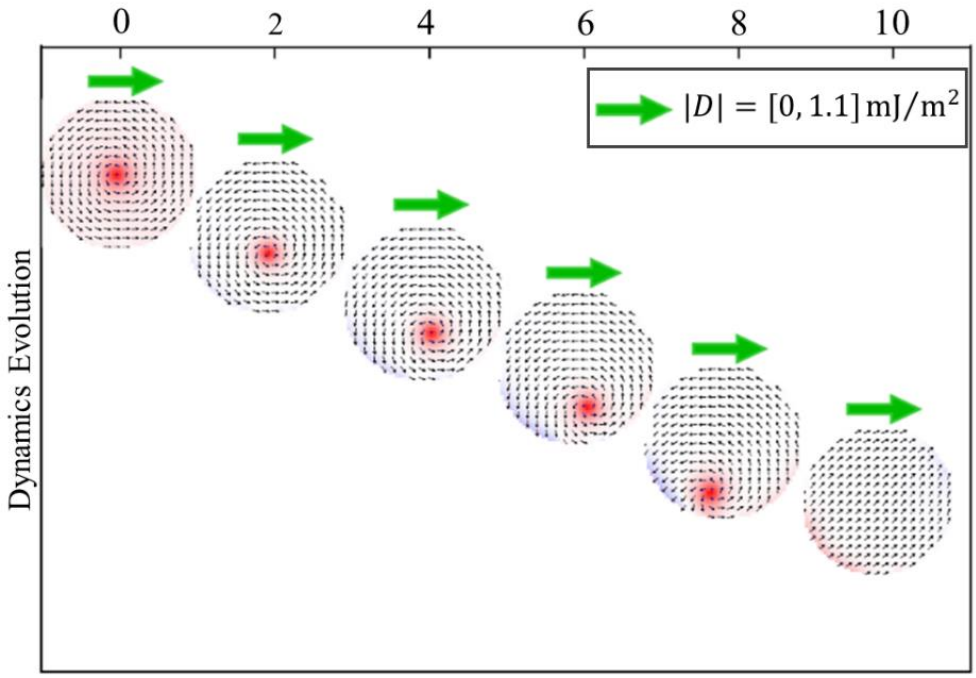

Figure 4.5 Micromagnetic simulations results of the time evolution of the spatial distribution of the magnetization for a circular vortex under the influence of the linear iDMI gradient in a CoFeB circular sample.

4.2.4 Experimental Generation of DMI Gradients

Based on micromagnetic simulations, we were able to explore the ranges of magnetic parameters under which DMI gradients can influence the dynamics of magnetic skyrmions, hopfions (**Chapter 3**), and magnetic vortices. For instance, varying DMI gradient along +x-direction revealed damping-dependent trajectories in single thin films, and a zero skyrmion Hall angle motion in case of SAF. On the other hand, experimental induction of DMI gradients offers validation and refinement of theoretical models by testing their predictions against real-world scenarios. While direct experimental studies on the DMI gradients may not be as prevalent as theoretical or simulation-based investigations, there exist some topics and methods for inducing spatial variations in the DMI strength. To create DMI gradients one can consider different approaches.

The first approach may focus on engineering thin films of Pt with controlled thickness gradients (in Pt/CoFeB heterostructures), this comes after observation of a Pt layer thickness dependence on the induced iDMI in ultra-thin Pt/CoFeB films [166]. Thus, sputtering, or pulsed laser deposition (PLD) can be used to design thin film heterostructures consisting of alternating layers of magnetic materials (e.g., CoFeB) and heavy-metal layers

(e.g., Pt). Varying the thickness of the heavy-metal layer (Pt) in a controlled manner across the sample can lead to the creation of DMI gradients.

In addition, several experimental setups showed the effect of mechanical strain on the magnetic properties of the materials, where it breaks inversion symmetry, providing access into tunable DMI [167]. By considering a thin film system with strong spin-orbit coupling deposited on top of a piezoelectric substrate, and applying an electric field, a controlled mechanical strain is generated.

To reach a DMI gradient resulting from a strain gradient, photolithography and etching, can be used to pattern the surface of a substrate with features of varying heights or shapes. The thin film placed on such a substrate will experience different levels of mechanical strain depending on its position relative to the substrate features.

Moreover, one can still think about different approaches including electric field control, spin-orbit torque gradients, and laser irradiation. These may have significant implications for spintronics and magnetic memory applications with enhanced functionality and performance.

4.3 Conclusion

Under the effect of a linear iDMI gradient, radial vortex moves with a damping-dependent trajectory in a single-layer *CoFeB* and 2d CrI_3, while a zero skyrmion Hall angle motion was observed in the SAF *CoFeB* and CrI_3 for both types of vortices.

On the contrary, the circular vortex was expelled from the sample since it is not stable for any finite iDMI, and we suggested that these dynamics can be exploited in voltage controlled DMI spintronic diodes to increase performance. Our results suggest alternative means for low-power manipulation of magnetic solitons in FM and SAF, and, particularly, in 2d materials. Specifically, future developments on the control of magnetic parameters by strain, geometry design, temperature gradients, and applied voltages and the implementation of 2d materials combined with soliton manipulation can allow for a new generation of highly efficient sensors and diodes for computing and energy harvesting.

Chapter 5

Magnetic Tunnel Junction

Controlling magnetic spin opens a realm of possibilities for creating faster, more efficient devices

Albert Fert

“Spintronics holds the promise of major breakthroughs in the performance of electronic devices and has the potential to revolutionize the field of electronics, creating a new generation of faster, smaller, and more energy-efficient devices.".

– Stuart S. P. Parkin”

This chapter concerns magnetic tunnel junctions (MTJ). First the chapter starts with an introductory section 5.1, followed section 5.2 where the important MTJ parameters are listed and discussed as three subsections. Four different switching approaches are presented in section 5.3. Section 5.4 will present three different MTJ-based applications. Section 5.4 is a conclusion.

5.1 Introduction to Magnetic Tunnel Junctions

Advancements in the field of fabrication technology have sustained the downscaling of CMOS technology over the past five decades due to which performance of the integrated circuits (ICs) has consistently improved following Moore's law. However, CMOS-based circuits suffer from various bottlenecks including scalability and power dissipation. For this reason, beyond-CMOS approaches have been a research concern to find alternatives for the future [168–170].

As the spin property of an electron is increasingly attracting attention, research was directed toward the exploration of spin transport electronics also known as spintronics. Spintronics emerged from discoveries in the 1980s concerning spin-dependent electron transport phenomena in solid-state devices. This includes the observation of spin-polarized electron injection from a ferromagnetic metal to a normal metal by Johnson and Silsbee (1985) [171] and the discovery of giant magnetoresistance independently by Albert Fert et al. [172] and Peter Grünberg et al. (1988) [173]. Spintronics are considered as one of the most promising future technologies, in the impending post CMOS era [174–177]. The class of spintronics is a promising slope [4,22,178–180], since they have a low energy dissipation, a high speed, and a reduced size.

The most common spintronic device used is the magnetic tunnel junction (MTJ) [181], characterized by its scalability, low power consumption and potentially infinite endurance. MTJs are magnetic heterostructures with three main functional components: a free ferromagnetic layer (FL), whose magnetization can rotate freely under the influence of an external magnetic field, an insulating tunnel barrier separating (FL) from next layer, and it is usually a crystalline MgO layer, and a fixed (pinned) ferromagnetic layer (PL) with a fixed magnetization direction. Each of these magnetic layers can be viewed as a single magnetic moment, treated with the Macrospin approximation, and orient in a particular direction.

In industry, the MTJ fabrication techniques typically involve thin film deposition, lithography, and material characterization methods. Most MTJs are designed in such a way as to have two stable magnetic orientations, usually along the same axis but in opposite directions. This can be achieved by patterning the stack into something such as an elliptical nanopillar whose shape creates two energy minima for the magnetic moments along the long axis of the ellipse. Magnetic anisotropy (MA) is an inherent property of the MTJ, where we can distinguish between in-plane magnetic anisotropy (IPA), and perpendicular magnetic anisotropy (PMA), depending on the direction of the easy axis. These two types of MA result in two different forms of MTJs, in-plane MTJ (iMTJ) and perpendicular MTJ

(pMTJ). Based on **Figs. 5.1(a)-(b)**, when the magnetic orientation of the FL and PL are parallel, then the resistance offered by the device for the flow of read current is less, and it is denoted by parallel resistance (R_P). Whereas, if the magnetic orientation of the FL is opposite to that of the RL, the device offers more resistance to the flow of read current, and therefore it is in the high resistance state and denoted by antiparallel resistance (R_{AP}). Thus, MTJs can be used as storage elements, with its two orientations serving as '0' and '1' in spin-transfer torque magnetic random-access memory (STT-MRAM). Such type of memories offers a significantly smaller power consumption, as well as improved scalability and speed compared to current memories in the market [182]. Switching between these two states requires overcoming an energy barrier denoted by E_b (**Fig. 5.1(c)**).

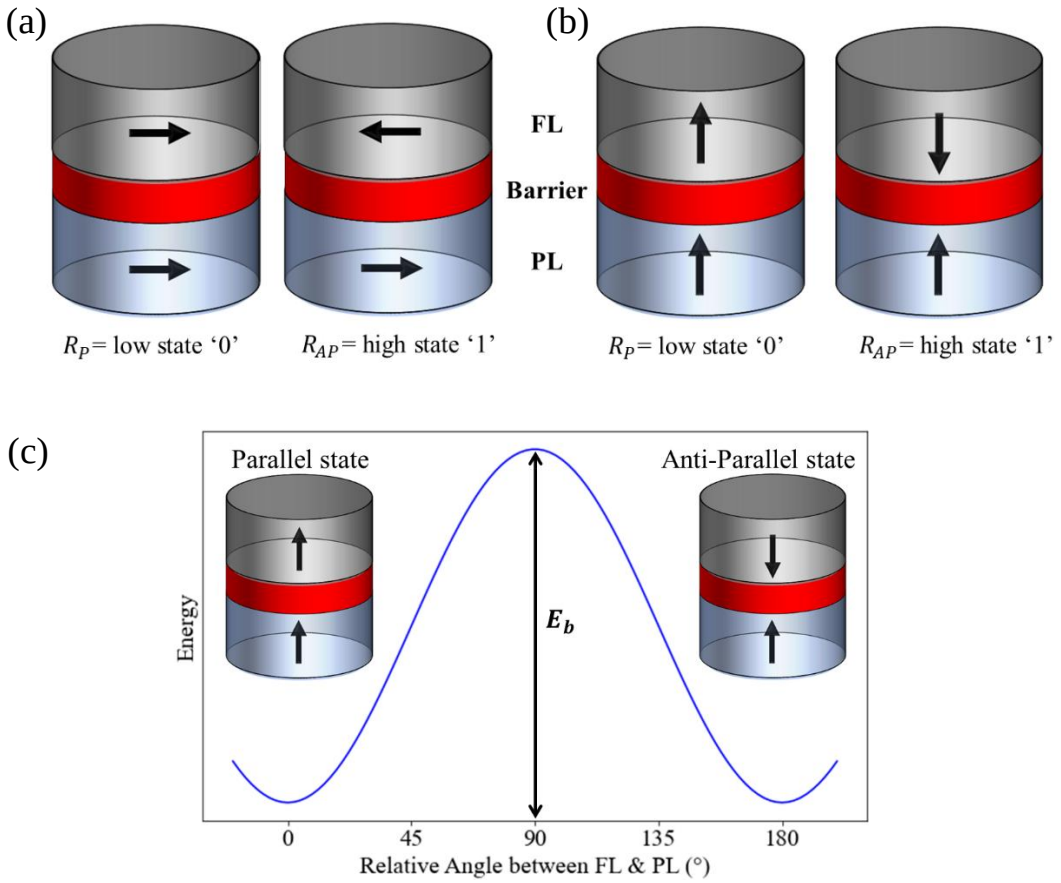

Figure 5.1 (a), (b) Front view of MTJ switching from P state to AP state, and vice versa for iMTJ and pMTJ, respectively. (c) An energy barrier E_b separates P and AP states of pMTJ, where the barrier height decides the stability of stable states of pMTJ.

5.2 MTJ Parameters

To serve as practical computer memory, a device needs to have two core properties: readability, being able to read off the current state of the device, and writability, being able to flip the current state of the device. These necessary properties for an MTJ to function as magnetic memory are facilitated by two quantum mechanical effects present in MTJs: tunneling magnetoresistance and spin-transfer torque. Tunneling magnetoresistance causes the two magnetic states to have different electrical resistances, allowing for a simple method to measure the current state of the MTJ.

5.2.1 Tunneling Magnetoresistance

Tunnel magnetoresistance (TMR) is a quantum mechanical phenomenon that occurs in a magnetic tunnel junction (MTJ). TMR arises from the spin-dependent tunneling of electrons across the insulating barrier between two ferromagnetic layers in an MTJ. The tunneling current through the barrier depends on the alignment of electron spins in the two ferromagnetic layers. When the magnetizations of the two ferromagnetic layers are parallel, electrons with parallel spins have a higher probability of tunneling through the barrier compared to electrons with antiparallel spins. As a result, the electrical resistance of the MTJ is lower in the parallel configuration.

This effect was originally discovered in 1975 by Michel Jullière [183] (University of Rennes, France) in Fe/Ge-O/Co-junctions at 4.2 K, but the relative change of resistance was around 14%, and did not attract much attention. In 2001 Butler and Mathon independently showed that using iron as the ferromagnet and MgO as the insulator, the tunnel magnetoresistance can reach several thousand percent [184,185]. In this regard, the success of the MTJ depends on the selection of material combinations with high TMR ratio (See **Fig. 5.2**). As shown in **Fig. 5.2** the highest TMR ratio is observed in a CoFeB/MgO/CoFeB structure. Significant growth was observed in the TMR ratio in case of MgO-based MTJ (red circles) compared to AlO_x (blue squares).

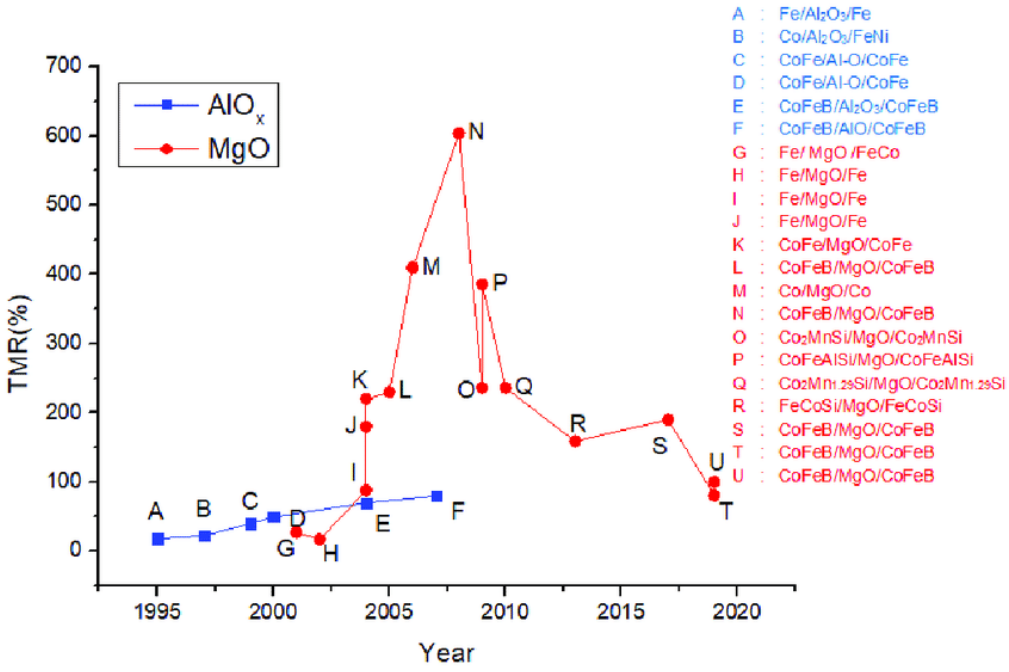

Figure 5 2 TMR ratio plotted at room temperature for various MTJ structures developed using both AlO_x and MgO barrier with a different FL and PL. Significant growth can be observed in the TMR ratio of MgO-based MTJ (red circles) compared to AlO_x (blue squares) during the year 2001 to 2008 [186].

Based on Fermi's Golden Rule, Julliere's model of tunneling magnetoresistance (TMR) states the conductance of each magnetic configuration (G_P & G_{AP}) is proportional to the density of states as follows:

$$G_P \propto \rho_{1\uparrow}\rho_{2\uparrow} + \rho_{1\downarrow}\rho_{2\downarrow} \quad (5.1)$$

$$G_{AP} \propto \rho_{1\uparrow}\rho_{2\downarrow} + \rho_{1\downarrow}\rho_{2\uparrow} \quad (5.2)$$

here $\rho_{1\uparrow}$ and $\rho_{1\downarrow}$ ($\rho_{2\uparrow}$ and $\rho_{2\downarrow}$) are the density of states at the Fermi energy of the majority and minority spins of the first (second) ferromagnetic layer. This can be viewed as a two current model, one for each spin state, depicted by **Fig. 5.3**. In this model, the current whose spin is the majority spin of both ferromagnetic layers will dominate over currents of minority spins or mixed majority and minor spins. This results in a lower resistance P state (because current can flow more easily) and higher resistance AP state. Now, if one defines spin polarization Pi for the *i-th* ferromagnetic layer as the net spin for electronic states at the Fermi surface:

$$Pi = \rho i\uparrow - \rho i\downarrow / \rho i\uparrow + \rho i\downarrow \qquad (5.3)$$

TMR is quantified by the TMR ratio, which is defined as the percentage change in resistance between the parallel and antiparallel configurations and can be calculated in terms of the spin polarization:

$$TMR \equiv \frac{R_{AP}-R_P}{R_P} = \frac{G_P-G_{AP}}{G_{AP}} = \frac{2P_1P_2}{1+P_1P_2} \quad (5.4)$$

where R_{ap} is the electrical resistance in the anti-parallel state, whereas R_p is the resistance in the parallel state.

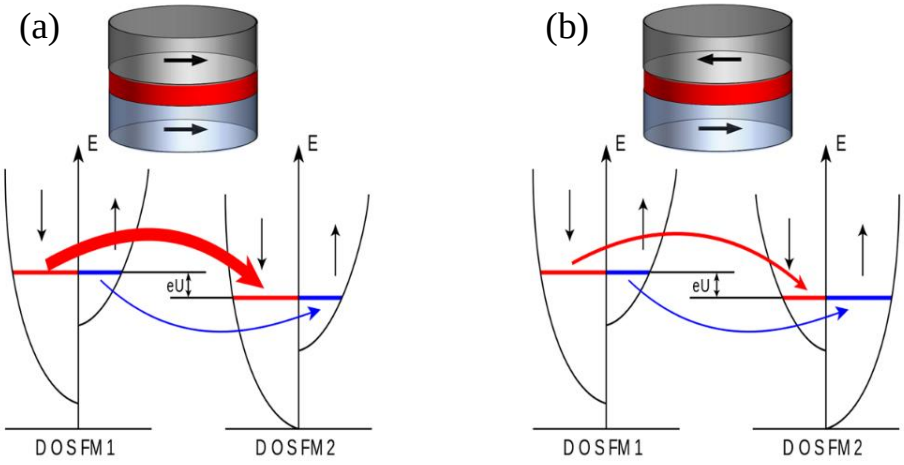

Figure 5.3 Band diagrams for up and down spins when MTJ is in (a) parallel configuration and in (b) anti-parallel configuration, to illustrate effect of tunneling magnetoresistance.

5.2.2 Switching Current I_c

The magnetization of the ferromagnetic layer is switched if the torque is large enough to overcome the energy barriers in the ferromagnetic layer. The rate of spin momentum transfer and the torque exerted are proportional to the rate of electron flow or the current and decide the switching time. The current needed to achieve a specific switching time is the critical current, I_C. This electric parameter is an important magnitude to switch the MTJ resistance. In addition, it is heavily related to the write pulse width, or switching time, which is defined as the length of time that the switching current is applied to the MTJ. Reducing the write pulse width will increase the critical switching current rapidly. The critical switching current is the whole-time range, from the long-time thermal reversal region to the short-time dynamic region, can be modeled by the stochastic Landau-Lifshitz-Gilbert dynamic equation with a spin-torque term.

$$I_c = I_{c0}\left\{1 - \frac{k_BT}{E_b}\ln\left(\frac{\tau}{\tau_0}\right)\right\} \quad (5.5)$$

Here, I_{c0} is the critical switching current at 0K, k_B is the Boltzmann constant, T is the temperature, E_b is the barrier height, τ is the switching time, and τ_0 is the inverse of the attempt frequency.

5.2.3 Thermal Stability

The thermal stability of MTJs is a critical property that determines their reliability and performance under different temperature conditions. It is influenced by different factors, including energy barrier E_b, magnetic barrier, magnetic anisotropy (MA), exchange coupling, temperature, and device design.

If the magnetization is switched via uniform rotation, the energy barrier is given by the anisotropy energy $E_b = K_u V$, where K_u is the anisotropy energy density and V is the MTJ cell volume. The thermal stability factor is then given by,

$$\Delta = \frac{K_u V}{k_B T} = \frac{H_k M_s V}{2 k_B T} \qquad (5.6)$$

where M_s is the saturation magnetization and H_k is the anisotropy field $H_k = 2K_u/M_s$.

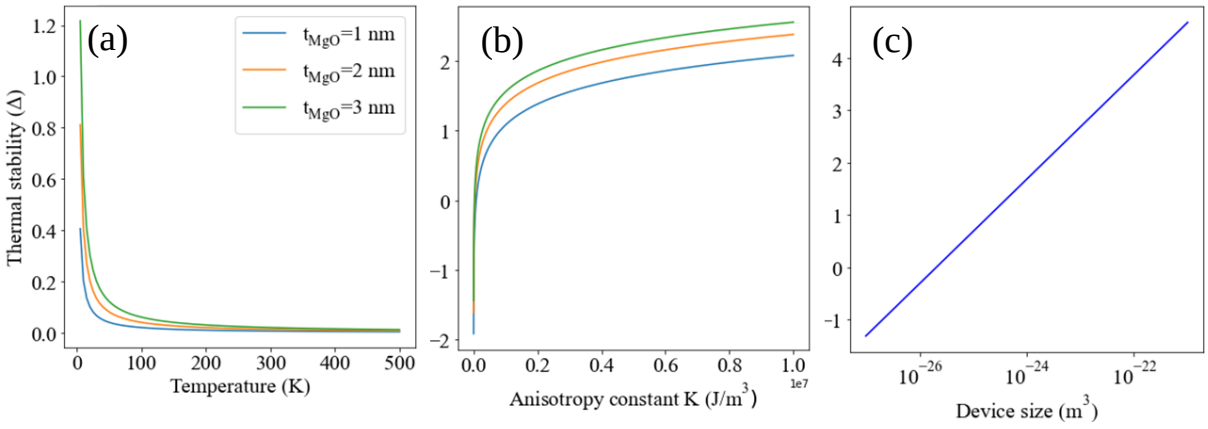

Figure 5.4 Variation of thermal stability (Δ) for an MTJ for three different thicknesses of MgO barrier, (a) versus temperature (K), magnetic anisotropy (J/m^3),and MTJ size (m^3).

In **Fig 5.4** we consider a circular MTJ device composed of CoFeB/MgO/CoFeB, with diameter 1 nm, and considering $M_s = 10^6$ A/m, T = 300 K, and anisotropy K = 10^5 J/m^3. **Fig. 5.4(a)** shows that for high temperatures, thermal fluctuations become more significant, leading to a reduction in the stability of the magnetic configuration. As the MgO barrier thickness increases, the thermal stability decreases. This is evident from the fact that the curves for thicker MgO barriers exhibit lower thermal stability compared to thinner barriers. **Fig. 5.4(b)**, proves that increasing the magnetic anisotropy of a material effectively strengthens the resistance of the material to thermal fluctuations, leading to higher thermal stability. According to **Fig. 5.4(c)**, larger MTJ devices tend to have higher thermal stability because they possess larger effective energy barriers, lower thermal energy densities, reduced damping, and potentially enhanced magnetic anisotropy. This

increased stability is advantageous for applications requiring reliable and robust magnetic behavior, such as magnetic memory devices and spintronic devices.

5.3 MTJ Switching Approaches

As we discussed that MTJ can exhibit two resistance states R_P and R_{AP} based on TMR effect, it becomes important to know the methods by which the novel device can be switched between the states. There exist a few methods available, where some are discussed below, to achieve the transition between the two states, each having its own advantages and disadvantages.

5.3.1 Field Induced Magnetic Switching (FIMS)

FIMS mechanism was employed in the first-generation iMTJs developed using an aluminum oxide-based insulating barrier [187]. In FIMS, the magnetization of the FL is switched by an externally induced magnetic field **H** produced by the current-carrying conductors placed close to the MTJ device.

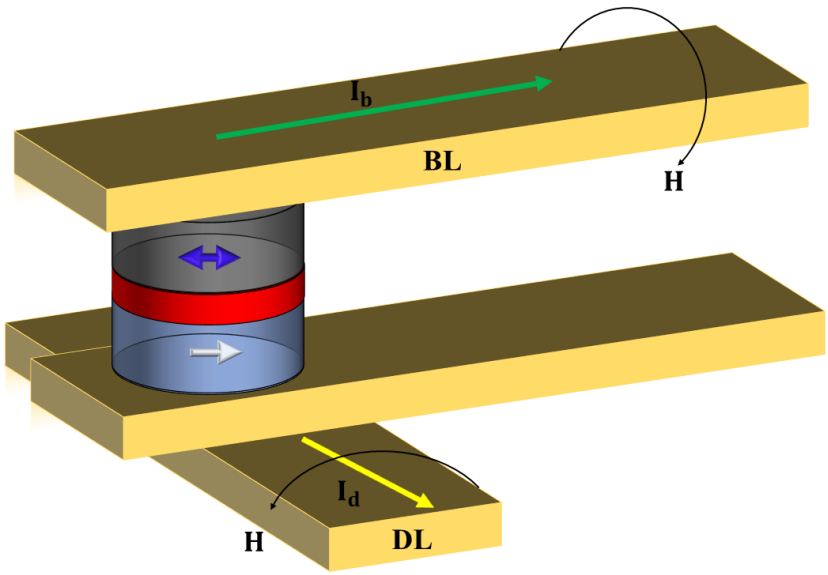

Figure 5.5 Illustration to understand the FIMS switching mechanism in iMTJ, situated between DL and BL, respectively.

As illustrated in **Fig. 5.5** MTJ is placed in between the two orthogonal current lines called digit line (DL) and bit line (BL). Bit line current ($\mathbf{I_b}$) with the assistance of digit line current ($\mathbf{I_d}$) is used to change the magnetic orientation of MTJ [188]. The current polarity of $\mathbf{I_b}$

decides the state of the MTJ (P or AP). Based on this mechanism, Freescale launched the first commercial 4-Mbit MRAM-MR2A16A in 2006 [186]. However, this method has several disadvantages, such as FIMS occupies a large area per cell and refrains from achieving the high density. FIMS mechanism needs a large current (>10 mA), which increases the total power consumption. In addition to that, as the separation between the adjacent cells reduces, magnetic field interference is induced between the cells which causes write error. MTJ situated close to the selected MTJ will be influenced by the external magnetic field generated by BL and DL. This tends to change the logic stored in the adjacent unselected MTJ. These issues hindered its commercialization.

5.3.2 Thermally Assisted Switching

To address the issues faced by FIMS, thermally assisted switching (TAS) method was proposed [189]. As illustrated in **Fig. 5.6** two extra anti-FM layers are added to the conventional MTJ, one AF_1 above the free layer and the other AF_2 below the reference layer, with AF_1 having a higher blocking temperature than AF_2. A temporary joule heat is produced by a pulse of low current $\mathbf{I_h}$ through the selected MTJ that heats the magnetic layers above their magnetic ordering temperature to reduce greatly the required switching field and then a magnetic field H, produced by magnetization current is applied to write it. This method of writing mechanism requires less power and provides higher speed. However, the mandatory heating and cooling processes lower the operation speed, which makes TAS approach expensive in the high-speed logic applications.

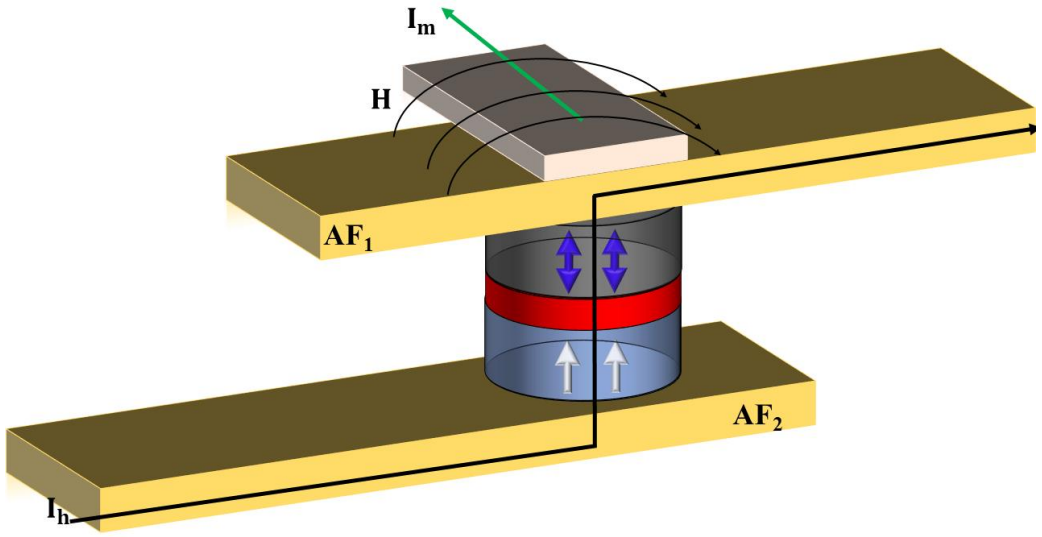

Figure 5.6 Illustration of TAS switching mechanism in pMTJ, which is present between two antiferromagnetic layers named AF_1 and AF_2.

5.3.3 Spin Transfer Torque (STT) Switching

Another switching methodology is based on STT [190], which uses only one low current going through the MTJ to switch its state. John Slonczewski at IBM first discovered this impact in 1996. STT switching is predicted as the most effective writing approach for MRAM and magnetic logic application till date [182,191].

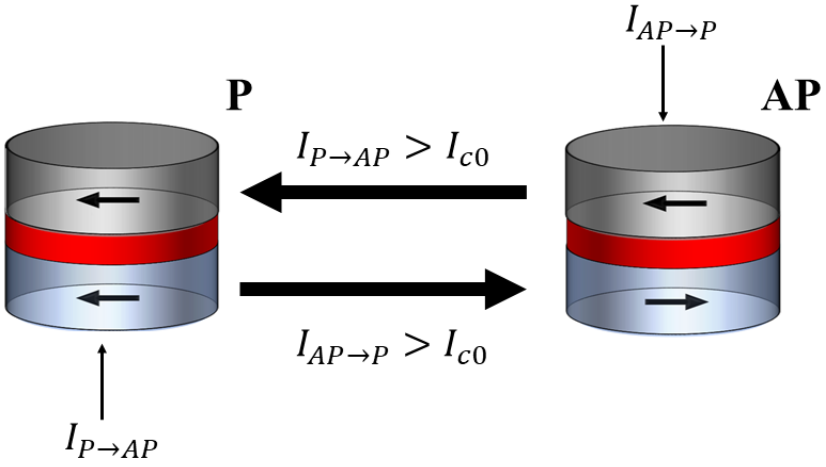

Figure 5.7 STT switching mechanism of an MTJ demonstrates two different states P and AP.

STT switching approach demonstrates two different states of MTJ. The state of the MTJ depends on the direction of current flow between the free and fixed layer. Writing current flowing from free layer to the fixed layer will store the logic "0" in the MTJ with the storage layer spin magnetization direction parallel to the pinned layer, whereas when current flows from the fixed layer to free layer, it will store the logic "1" in the MTJ with the storage layer spin magnetization direction antiparallel to that of the pinned layer resulting in high resistance of the MTJ. To change the resistance state or logic-in MTJ, the writing current flowing through MTJ must be greater than the critical current density (J_{c0}). STT switching presented in **Fig.5.7** shows that the behavior can be categorized into two main regions:

1. Precessional region ($I_{P->AP} > I_{C0}$)

2. Thermal activation region ($I_{P->AP} < I_{C0}$).

In the precessional region, MTJ experiences rapid precessional switching. In the thermal activation region, although the current is less than the critical value, switching can occur with a long input current pulse due to thermal activation. While STT approach offers significant advantages in terms of read energy and speed, a significant incubation delay due to the pre-switching oscillation incurs high switching energy.

5.3.4 Spin Hall Effect (SHE) Switching

Spin Hall effect (SHE) is another way to switch the magnetization of the free layer by an in-plane injecting current [192]. A three-terminal magnetic device based on SHE has been proposed, where a heavy metal strip (e.g., Ta, Pt) with a large spin-orbit coupling parameter is placed below the free layer. When a current passes through the heavy metal, electrons with different spin directions are scattered in opposite directions. The spin-orbit coupling converts the charge current into perpendicular spin current, generating a torque called spin-orbit torque (SOT, or spin Hall torque) to assist magnetization reversal. The orientation of the free layer is controlled by the direction of the injecting current.

5.4 MTJ Based Devices

Based on the appealing features of MTJ, much research effort has been devoted to applying it in design of memories and specific logic functions. This section will briefly review some typical designs of MTJ based circuits.

5.4.1 Magnetoresistive Random Access Memory

Magnetic Tunnel Junctions (MTJs) have garnered significant attention in the development of Magnetoresistive Random Access Memory (MRAM) [186]. The architecture of MRAM consists of several MTJs, where each MTJ is connected to the crossing points of two perpendicular arrays of parallel conducting rows and columns. To successfully program the memory cell, current pulses are sent through one line of each array and the MTJ at the crossing point of these two orthogonal lines can be switched with sufficient magnetic field (for FIMS) or current density (for STT). For reading operation, the resistance of the device between the two selected crossing lines can be sensed out, which represents the information stored in the MTJ.

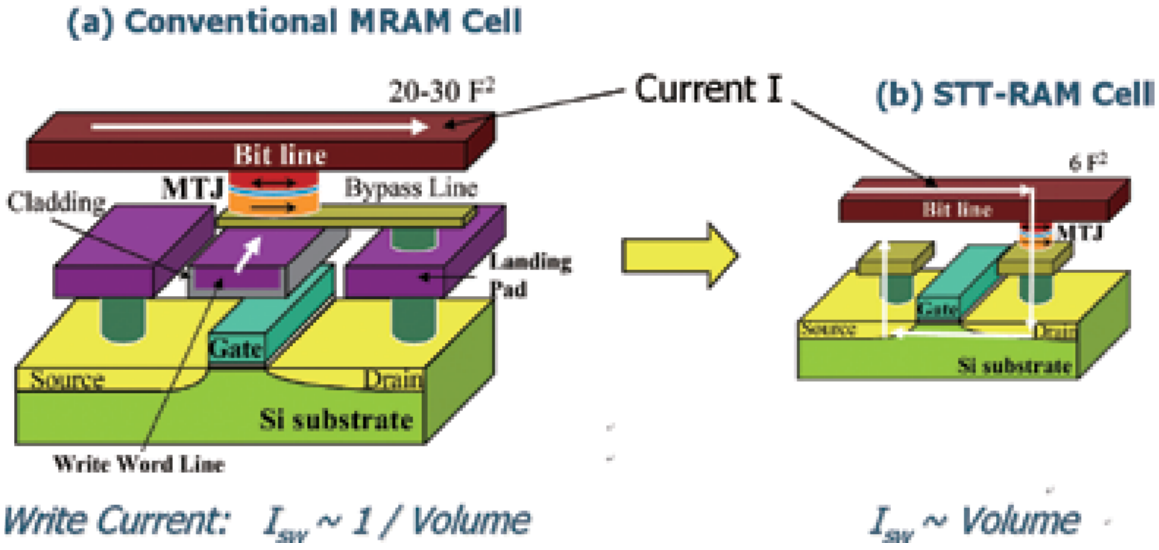

Figure 5.8 Comparison of memory cell architecture between (a) conventional field switching MRAM, and (b) spin transfer torque MRAM.

The ability of a spin-polarized current to switch the orientation of the magnetic moment, and to excite it into microwave precession, by the torque exerted through the transfer of spin angular momentum from the incident conduction electrons, have catalyzed the new generation of MRAMs, particularly spin-torque magnetic random-access memory (ST-MRAM) and possibly spin-torque excited, nanoscale microwave oscillators. Much progress has been made on the MTJ parametric level including thermal stability, resistance area product (RA), and magneto-resistance ratio (MR) [191]. A study carried by Huai et al. illustrated the transformation from conventional MRAMs to STT based MRAM (**Fig. 5.8(a)-(b)**) and yielded reliable reversal behavior for pulse widths as short as 100 psec for an energy pulse of less than 0.2 pJ [182].

5.4.2 MTJ Based Spin Logic

Traditional transistor-based semiconductor logic uses charge for encoding binary information as 0 and 1, which means logic level switches depend on the changes of charge magnitudes. As a result, drastic power consumption limits future development in this domain. The arrival of the up and down spins of electrons, MTJ-based logic provides numerous advantages, including nonvolatility, high speed, and low power consumption [181].

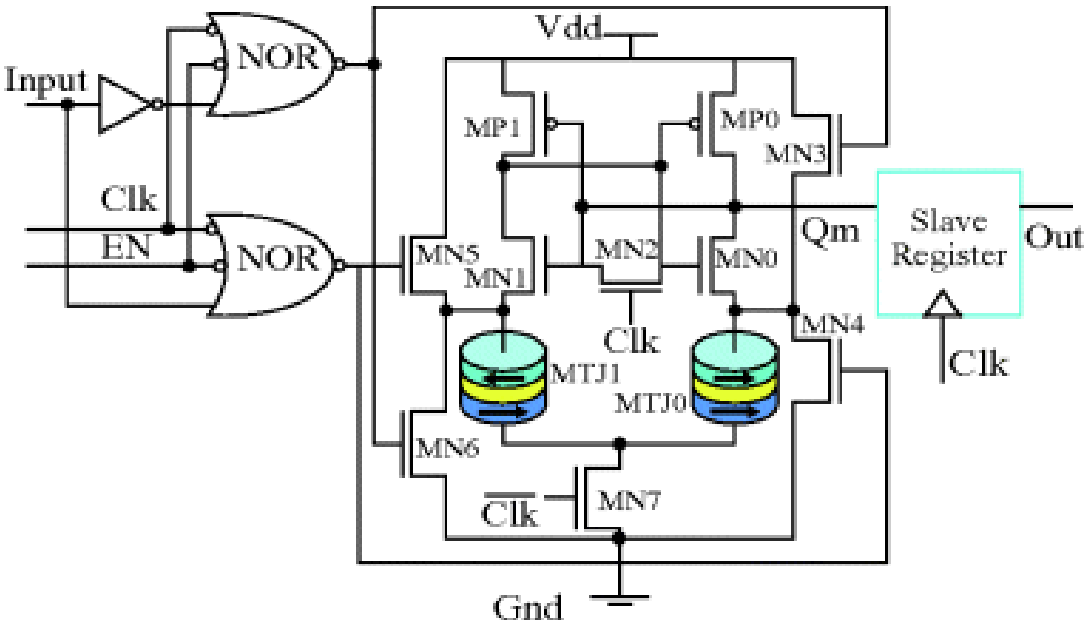

Figure 5.9 Full schematic of spin-MTJ-based non-volatile flip-flop.

Generally, MTJ-based logic design follows two approaches: First, one or more MTJs are used to realize logic functions individually, such as a single device or a flip-flop register as illustrated in **Fig. 5.9** second, a range of MTJs constitutes a two-dimensional memory array, for example, the field-programmable gate arrays (FPGAs).

5.4.3 MTJ Based Neuromorphic Computing

Neuromorphic computing systems inspired by the human brain can benefit from MTJs as building blocks for memory and computation. MTJs with multilevel resistance states can emulate the analog behavior of biological synapses, enabling efficient and parallel processing of neural signals.

Stochastic synapses in biological neural networks exhibit randomness in their response to input signals [11], similarly a stochastic behavior is observed in MTJs during magnetization reversal. This stochasticity arises from various sources, such as thermal fluctuations, spin-transfer torque, and voltage-induced effects [193]. Thus, a recognized number of research was done in this context. This include the mapping of the probabilistic spiking nature of pyramidal neurons in the cortex to the stochastic switching behavior of a Magnetic Tunnel Junction in presence of thermal noise [10].

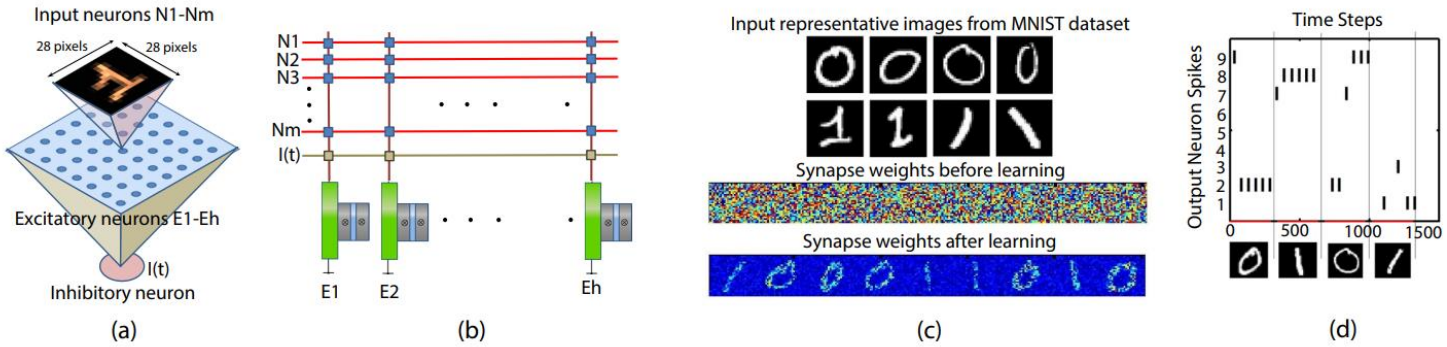

Figure 5.10 (a) Stochastic spiking neural network used for digit recognition. Input spike trains are received by all the stochastic neurons (connections shown for only one neuron). The inhibitory neuron prevents the neurons from spiking in case an excitatory neuron spikes. (b) Corresponding implementation in a crossbar array fashion. Programmable resistive synapses are present at each cross-point. Input voltages are applied at each row and the neurons receive input synaptic current which is the weighted summation of the input voltages. (c) A network of 9 excitatory neurons were used for the recognition purpose. The synapse weights were randomly initialized. 784 input neurons (28 x 28 images) are rate encoded by ensuring that the spike frequency is directly proportional to the pixel intensity. After learning the neurons respond selectively to each input image. (d) For testing the behavior of the network after learning has been accomplished, STDP and homeostasis were turned off. The neuron stochastically spikes the maximum for the class which it has learnt while the others remain mostly silent. A common lateral inhibitory signal during testing results in sparse spiking events.

The behavior of a network of such stochastic MTJ neurons were studied in a standard digit recognition problem based on the MNIST data set (**Fig. 5.10(a)**). A crossbar array was designed (**Fig. 5.10(b)**), consisting of 9 neurons characterized by random synaptic weight as shown in **Fig. 5.10(c)** Moreover the STDP rule was used in the learning process (**Fig. 5.10(d)**).

Another study was carried by Sengupta and his colleagues [22], where they demonstrated the close resemblance of the magnetization dynamics of a Magnetic Tunnel Junction (MTJ) to short-term plasticity and long-term potentiation observed in biological synapses. In order to test if the proposed MTJ synapse mimics the short-term memory (STM), and the long term memory (LTM) of a biological neuron, a 34 × 43 memory array was stimulated by a binary image of the Purdue University logo.

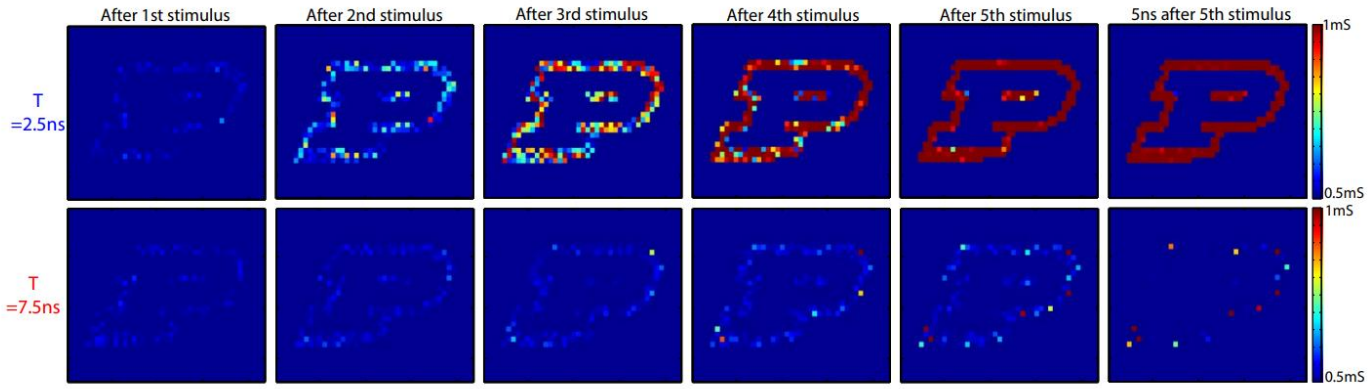

Figure 5.11 STM and LTM transition exhibited in a 34 × 43 MTJ memory array. The input stimulus was a binary image of the Purdue University logo where a set of 5 pulses (each of magnitude 100μA and 1ns in duration) was applied for each ON pixel. While the array transitioned to LTM progressively for frequent stimulations at an interval of T = 2.5ns, it "forgot" the input pattern for stimulation for a time interval of T = 7.5ns [22].

The snapshots of the conductance values were given in **Fig.5.11** for two different stimulation intervals of 2.5ns and 7.5ns respectively. While the memory array attempts to remember the displayed image right after stimulation, it fails to transition to LTM for the case T = 7.5ns and the information is eventually lost 5ns after stimulation. However, information gets transferred to LTM progressively for T = 2.5ns.

5.5 Conclusion

In conclusion, this chapter has provided a quick exploration of Magnetic Tunnel Junctions (MTJs), some of their important parameters that will be later in the coming chapters, and few examples about their diverse applications in various fields, including spintronics, memory devices, and neuromorphic computing.

Chapter 6 Neuromorphic Computing & Spiking Neural Networks

Where attention goes, neural firing flows, and neural connection grows

Daniel J. SIEGEL

"A single neuron in the brain is an incredibly complex machine that even today we don't understand. A single 'neuron' in a neural network is an incredibly simple mathematical function that captures a minuscule fraction of the complexity of a biological neuron.

— Andrew Ng"

"

Chapter six starts by section 6.1 presenting the principles of neuromorphic computing from its very beginning till our present time. Then section 6.2 will shed light on the most powerful type of neural networks, the spiking neural network "SNN". While section 6.3 describes the dynamics of biological neurons, the two most popular neuron models are discussed in section 6.4. Sections 6.5 and 6.6 focus on the neural coding paradigms and the noise of the spiking neurons respectively. Learning procedures are discussed in detail in section 6.7.The last section 6.8, presents the concepts of synaptic plasticity.

6.1 The principles of neuromorphic computing

Inspired by the human brain and the functionality of our nervous system, Neuromorphic computing was introduced in the 1980s by Carver Mead colleagues. He proposed the idea of building electronic circuits that mimic the principles of the human brain, emphasizing the efficient processing of sensory data and cognitive tasks. This came after conventional computers based on von-Neumann architectures showed up their deficiency in several areas. Since in modern computers based on Von Neumann architecture, the central processing units (CPU) and the main memory are separated physically and connected by a central bus consisting of collection of wires (**Fig. 6.1(a)**). Thus, energy and data throughput will be lost during transmission between memory storage and the processing unit. An additional bottleneck in von-Neumann computers is encoding data in binary values.

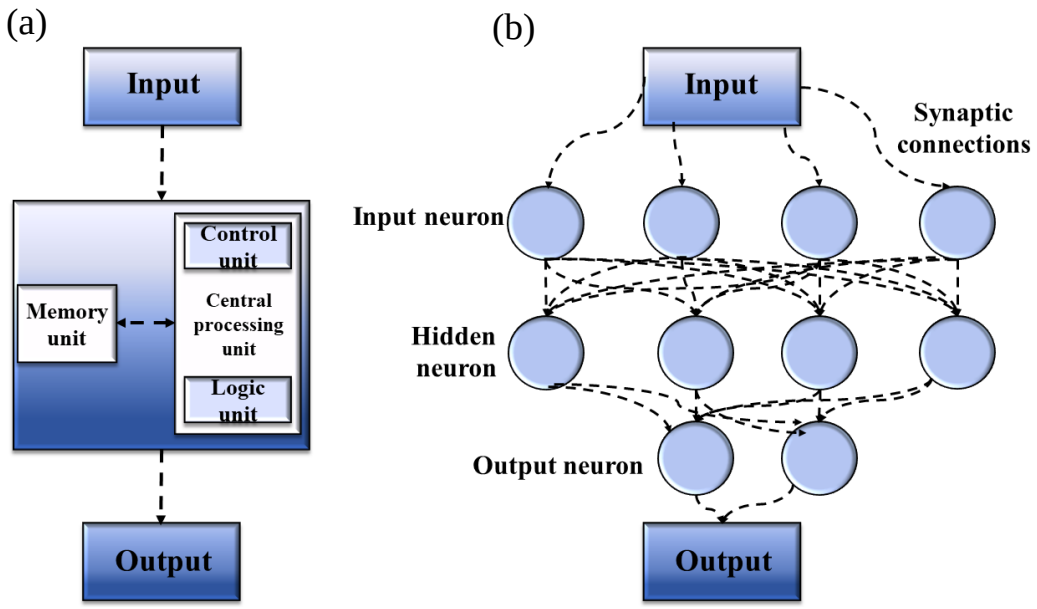

Figure 6.1 Comparison between (a) von-Neumann and (b) neural network computing architectures.

Neuromorphic computing architecture (**Fig. 6.1(b)**) has grown to refer to a variety of brain-inspired computers, devices, and models that contrast with the pervasive von-Neumann computer architecture. This biologically inspired approach aims to create highly connected synthetic neurons and synapses that can be used to model neuroscience theories as well as solve challenging machine learning problems. Recently, this concept has taken the front seat, as artificial intelligence has led scientists to advance neuromorphic computing to excel in the field of technology. One of the technological advancements that has rekindled the interest of scientists in neuromorphic computing is the development of the Artificial Neural Network (ANN) model.

6.1.1 Early Networks and Development.

The evolution of ANNs can be broadly categorized into three generations, each representing advancements and innovations in architecture, training algorithms, and applications [194]. The early start was in 1943, with the first-generation neural networks-based McCulloch-Pitts neurons designed to perform simple logical operations. However, the first attempt to create machine learning algorithms based on neural network principles was introduced in 1958 by Frank Rosenblatt through the development of perceptrons. Which takes a weighted sum of input and returns '0' if the result is below threshold and '1' otherwise (**See Fig. 6.2**).

The second generation of neural networks saw the development of multi-layer perceptrons (MLPs), which are capable of learning non-linear decision boundaries using hidden layers. Backpropagation, a training algorithm for MLPs, was also developed during this time.

Later the third generation of neural networks has been dominated by the rise of deep learning, which involves training neural networks with many layers (deep architectures). This includes the Feedforward Neural Networks (FNNs), the Convolutional Neural Networks (CNNs), the Recurrent Neural Networks (RNNs).

These networks have demonstrated unprecedented success in machine learning, however these algorithms most often run on supercomputers, which, unlike the brain, physically separate core memory and processing units.

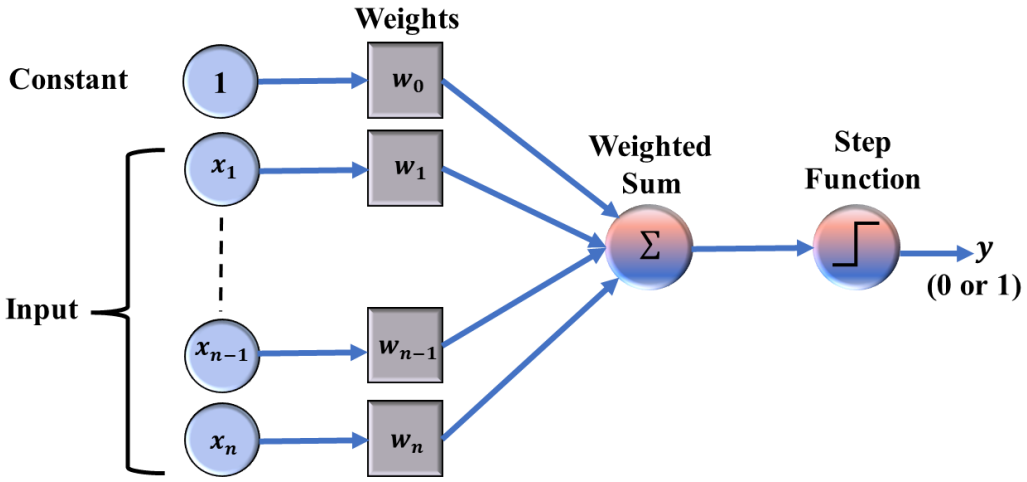

Figure 6.2 Schematic representation of a perceptron. It takes a weighted sum of input and returns '0' if the result is below threshold and '1' otherwise.

This slows them down and substantially increases their energy consumption, because the information is shuttled between the storage units and the processor. Additionally, modern computers have been designed to solve complicated numerical problems with high precision, while the brain uses many low-precision calculations in parallel to perform a task such as recognizing a face. For that reason, the brain differs vastly from human-made computing systems, both in terms of topology and how it processes information.

6.1.2 Neural Network Architecture

Let us suppose we have the network shown in **Fig. 6.3(a)**, the leftmost layer in this network is called the input layer, and the neurons within this layer are called input neurons. The rightmost or output layer contains the output neurons (in this case, a single output neuron). The middle layer is called a hidden layer since the neurons in this layer are neither inputs nor outputs. The network above has a single hidden layer, but some networks have multiple hidden layers. For example, **Fig. 6.3(b)** shows a four-layer network with two hidden layers. The output of each single neuron in the hidden layers and the output layer is expressed as $f(\boldsymbol{wx}) = f(\sum_{i=1}^{n} w_i x_i + w_0)$ where f is called activation function. In the case of a perceptron as introduced previously, f is a step function. However, other activation functions such as sigmoid function $\sigma(z) = 1/(1+e^{(-z)})$ are more commonly used because the differentiability of the function makes it possible for learning the weights of the networks. The output of the neuron in this case is $\sigma(\boldsymbol{wx})$.

The design of the input and output layers in a network is straightforward. Let's consider an image of a handwritten "two" A natural way to design the network is to encode the intensities of the image pixels into the input neurons. If the image is a 64 by 64 greyscale image, then we would have 4,096 = 64 × 64 input neurons, with the intensities scaled appropriately between 0 and 1. The output layer will contain just a single neuron, with output values of less than 0.5 indicating "the input image is not a "two", and values greater than 0.5 indicating "the input image is a "two".

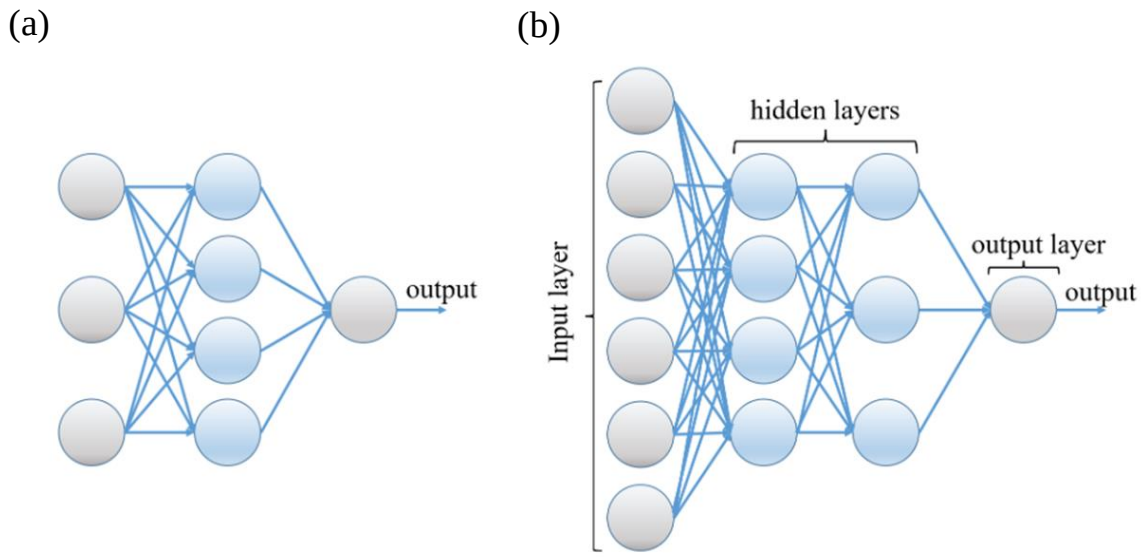

Figure 6.3 Schematic representation of the neural network's architectures. (a) A single hidden layer neural network. (b) A four-layer network with two hidden layers.

Researchers proposed many design heuristics for the design of hidden layers, which help practitioners get the behavior they want out of their networks. The neural networks where the output from one layer is used as the input to the next layer without any loops are called feedforward neural networks (FNN).

6.2 Spiking Neural Network

As the human brain is the most powerful and energy efficient computing system known, with billions of neurons each connected to about 10000 other neurons via synapses. with less than 20W of power consumption, and as ANNs showed several limitations that

researchers and practitioners need to be aware of, an attempt to design a neuro-inspired system that mimics the human brain and that exploit nanoelectronics has become extremely urgent and has led to the emergence of major projects [12].

Neurons in an ANN are characterized by a single, static, and continuous valued activation. However, biological neurons use discrete spikes to compute and transmit information, and the spike times, in addition to the spike rates, matter [195]. Although ANNs are historically brain-inspired, there are fundamental differences in their structure, neural computations, and learning rules compared to the brain. One of the most important differences is the way that information propagates between their units.

All the observation mentioned above, led to the realm of the third-generation bio-realistic neural networks, also known as spiking neural networks (SNN) are believed to hold promise for further energy improvement over artificial neural networks [194], being the best to mimic human brain. In the brain the communication between neurons takes place via trains of action potentials, known as spike trains. Each individual spike is sparse in time; thus, the timing of the spike holds high information content. It has been shown that the precise timing of every spike is highly reliable for several areas of the brain and suggests an important role in neural coding [196].

The architecture of a typical spiking neural network (SNN) is composed of a set of pre- and post-neurons that fire stochastically and connected through synapses. A postsynaptic neuron receive signals through the dendrites from a presynaptic neuron, where the receiving neuron read the analog input data in a form of spike trains using either a rate based method [197] which is based on spike firing first spike relies solely on the number of spikes over a certain time period, or by temporal coding [198] which is based on the temporal information in spike trains and includes time-to-first-spike. We can also mention the population coding [199], rank-order coding [200], and phase coding [201]which uses a periodic oscillation function as a global reference. As biological neurons in the brain or either in a simulated spiking neuron receive synaptic inputs from other neurons in the neural network, we can state that biological neural networks have both action potential generation dynamics and network dynamics. This makes biological neural networks much complex compared to artificial SNNs that we tend to simplify as much as we can. In this context we should mention that spiking neurons are governed by different models, with varying levels of sophistication, ranging from the most complex Hodgkin-Huxley model [202] to the simplest Izhikevich neuron model [203].

On the engineering level, SNNs are advantageous over traditional neural networks regarding implementation in special purpose hardware. As spiking networks have the special property to be sparse in time, this means that the energy consumption in biological networks depends on the number of events. Thus, few events or spikes characterized by high information content led to reduced energy consumption [204]. Hence, it is possible to create low energy spiking hardware which is highly responsive to event-based sensors based on the property that spikes are sparse in time [205]. **Table 6.1** below illustrates a comprehensive comparison of the spiking neural networks with other machine learning methods over different inclinations.

Method	Statistical Method	ANN	SNN
information	Scalar	Scalar	Spiking Sequence
Data presentation	Scalars, vectors	Scalars, vectors	Whole TSTD pattern
Learning	Statistical, limited	Hebbian rule	STDP
Dealing with RSTD	Limited	Moderate	Excellent
Parallel computation	Limited	Moderate	Massive
Hardware support	Standard	VLSI	Neuromorphic VSLI

Table 6.1 Comparison of the SNN and other machine learning techniques [206].

Recently a remarkable number of research focused on SNNs due to its success in the domains of visual processing [207–209], speech recognition [210,211] and luckily medical diagnosis, where Gosh et al. succeeded in developing an efficient SNN model for epilepsy and epileptic seizure detection using electroencephalograms (EEGs), a complicated pattern recognition problem [212]. Moreover, in [213] Kasabov and his colleagues presented a novel method and system for modelling of spatio-temporal patterns with a case study on stroke.

One complexity of SNNs is the difficulty of the learning process, where in comparison to traditional deep networks, training deep spiking networks is in its early phases. In SNNs the spike trains are represented formally by sums of Dirac delta functions and do not have derivatives. This makes it difficult to use derivative-based optimization for training SNNs, although very recent work has explored the use of various types of substitute or approximate derivatives [214]. However, training a spiking neural network does not follow the rule of conventional ANN, and we need to devise new methods of training that are compatible with the unsupervised nature of these networks. Thus, spiking networks enables a type of bio-plausible learning rule that cannot be directly replicated in non-spiking networks. This learning rule is the spike time dependent plasticity (STDP). Its key feature is that the weight connecting a pre- and post-synaptic neuron is adjusted according to their relative spike times within an interval of roughly tens of milliseconds in length [215]. Unsupervised learning in SNNs often involves STDP as part of the learning mechanism.

6.3 Dynamics of a Biological Neuron

Although neurons are only one of many brain cells, they have attracted more attention than other brain cells because of their fundamental role in computational operations. The fundamental function of a neuron is simple: the neuron receives input signals from other neurons via connections called Synapses, and if the potential of the input signals exceeds certain threshold, they will fire an action potential (spike) that propagates through synapses to other neurons.

Neurons consisted of three main parts: the dendrite, the soma, and the axon. Dendrites are considered as the receiver of input signals, and neurons receive input current via their dendrites. This input's current is then transmitted to the main body of the cell, called the soma. When a neuron generates an action potential, it sends current down its axon, causing neurotransmitters to release at the synapses, which are connections from a neuron's axon to the dendrites of other neurons. This neurotransmitter release causes the flow of dendritic currents in other connected neurons. The main body of the neuron is called soma. From a computational perspective, this is where all the incoming currents from dendrites are integrated. The process of producing an action potential also occurs in the soma.

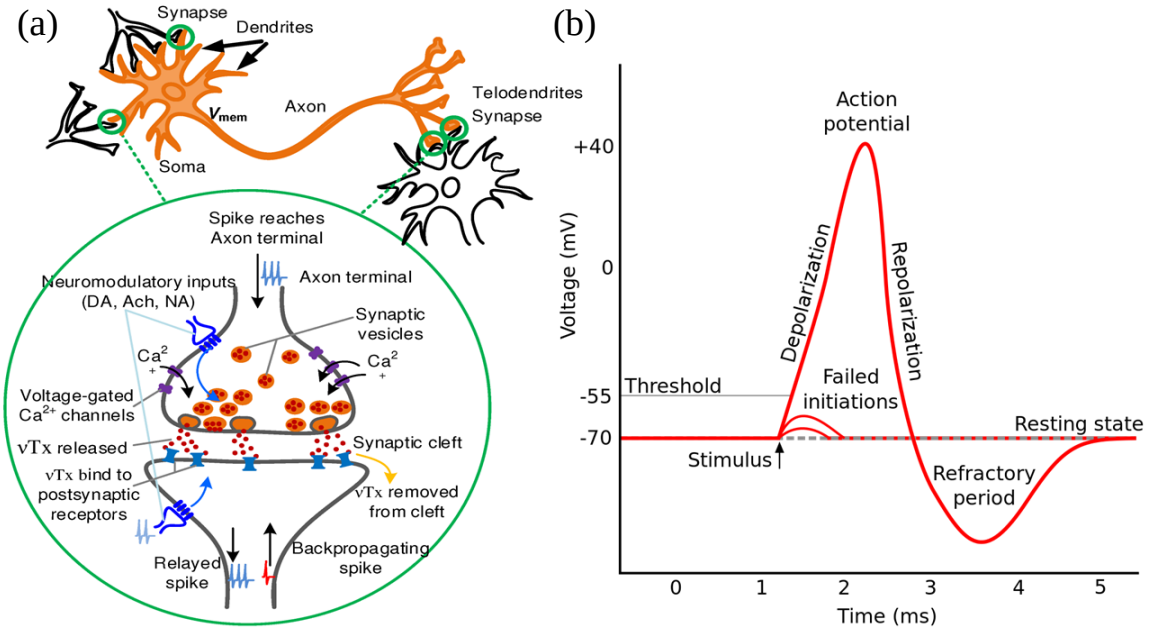

Figure 6.4 (a) The Synapses are present at the junction of axonal terminal and dendrites of the biological neurons. Some of the known neurotransmitter signaling mechanisms are illustrated [216]. (b) Approximate plot of a typical action potential shows its various phases. The membrane potential starts out at approximately −70 mV at time zero. A stimulus is applied at time = 1 ms, which raises the membrane potential above −55 mV (the threshold potential). After the stimulus is applied, the membrane potential rapidly rises to a peak potential of +40 mV at time = 2 ms. Just as quickly, the potential then drops and overshoots to −90 mV at time = 3 ms, and finally the resting potential of −70 mV is reestablished at time = 5 ms.

When a neuron is in resting state, the soma has a negative potential called the resting potential and controlled by ion pumps that maintain a particular concentration of ions (mostly sodium Na^+, potassium K^+, and calcium Ca^{2+}) inside the cell. The incoming current from dendrites causes the cell membrane to depolarize. The difference in ionic concentrations inside the cell membrane is considerably small during a single spike, but

throughout many spikes, the ion pumps are required to maintain the proper concentrations of sodium and potassium.

Fig. 6.4(a) illustrates the neuron as a complicated information-processing unit, which receives thousands of signals from the dendrite of other neurons through synaptic connection. The single output of this neuron is an action potential (spike) which emits whenever the membrane voltage reaches a threshold. Whenever the potential in the soma becomes high enough, it starts to trigger sodium channels, which allow sodium ions to enter the cell and further depolarize it. The process continues until the electrical gradient of the sodium channel opposes the chemical gradient of imbalance in sodium charge inside and outside of the cell. This process causes a considerable change in membrane potential and alters the membrane potential from a negative to a positive charge.

The considerable depolarization of the membrane potential triggers the potassium channels and lets them reach out of the cell and eventually repolarize it. At the same time, the sodium channels become inactivated. The open potassium channels finally bring the cell to a potential lesser than its resting potential, which is called the hyperpolarized state. Here process continues for a short while in which the neuron is not capable of generating spikes, which is called the absolute refractory period (the different states of a neuron are illustrated in **Fig. 6.4(b)**).

6.4 Models of Single Neurons

There are so many biological neuron models available to analyze the behavior of a biological neural network with varying levels of sophistication. These models play a key role for characterizing what the nervous system does, determining how it functions, and explaining why it operates in a particular way. Starting with the leaky integrate and fire model (LIF) being the earliest neuron model which was first investigated in 1907 by Lapicque [217], to the most detailed and realistic Hodgkin-Huxley model which is the starting point for detailed neuron models accounting for numerous ion channels, different types of synapses, and the specific spatial geometry of an individual neuron. This model was set by Alan Hodgkin and Andrew Huxley who derived it in 1952 to explain the ionic mechanisms underlying the initiation and propagation of action potentials in the squid giant axon [202].

6.4.1 Leaky Integrate-and-Fire Model

The leaky integrate-and-fire neuron is probably the best-known example of a formal spiking neuron model. Action potentials of a neuron **i** here are considered as events in which if their voltage $\mathbf{u_i(t)}$ reaches a threshold ϑ, the neuron fires a spike. This potential is considered in its resting state $\mathbf{u_{rest}}$ when there is no coming input to the cell membrane.

To describe the dynamics of the neuron, integrate and fire models use two separate components: first, an equation that defines the evolution of the membrane potential $u_i(t)$, and second, a mechanism for generating action potentials [197]. Louis Lapicque [217]

showed that a neuron can be considered as a circuit consisting of a resistor R that represents ion channels, (each small resistor represents an ion channel) in parallel to a capacitor C that represents the membrane potential this circuit was known later as LIF circuit. The input data received by a neuron is represented by input current *I*(t), in the RC circuit (**Fig. 6.5**).

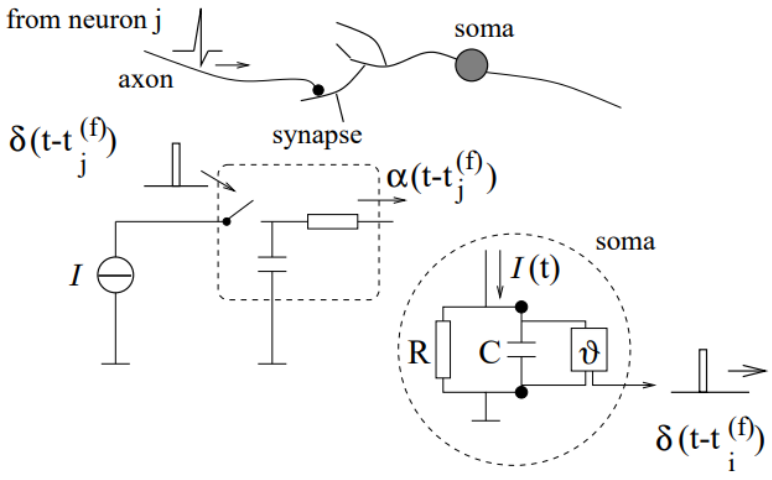

Figure 6.5 Schematic diagram of the integrate-and-fire model. The basic circuit is the module inside the dashed circle on the right-hand side. A current I(t) charge the RC circuit. The voltage u(t) across the capacitance (points) is compared to a threshold ϑ. If u(t) = ϑ at time $t_i^{(f)}$ an output pulse δ(t − $t_i^{(f)}$) is generated. Left part: A presynaptic spike δ (t − $t_j^{(f)}$) is low-pass filtered at the synapse and generates an input current pulse α (t − $t_j^{(f)}$) [218].

Using the law of current and splitting into two elements,

$$I(t) = I_R + I_C \quad (6.1)$$

Using Ohm's law, we can rearrange (**Eqn. 6.1**) to the equation presented below:

$$I(t) = \frac{u(t)-u_{rest}}{R} + C\frac{du}{dt} \quad (6.2)$$

Multiplying (**Eq. 6.2**) by R and using the time constant τ_m = RC yields the standard form:

$$\tau_m \frac{du}{dt} = -[u(t) - u_{rest}] + RI(t) \quad (6.3)$$

The solution to this differential equation considering the initial condition $u(t_0) = u_{rest} + \Delta u$ is in form:

$$u(t) - u_{rest} = \Delta u \exp(-\frac{t-t_0}{\tau_m}) \text{ for } t > t_0 \quad (6.4)$$

6.4.1.1 Dynamics

Based on **Eqs. (6.1-6.4)**, several simulations are performed to show the behavior of LIF neurons under specific conditions. The simulation time is set to 10 ms and the membrane time constant here is considered τ=1 ms, his means that the membrane potential reaches approximately 63.2% of its steady-state value after 1 ms when subjected to a step change in input current. The current density ($\mu A/cm^2$) is denoted by I in our simulations. First let's consider that the membrane potential has a threshold $\mathbf{u_{th}}$ = 0.5 mV, if the external pulse is less than exciting the membrane potential, then the membrane potential will gradually increase in response to the input current but will not reach the threshold potential for firing.(**Fig. 6.6(a)**). When the applied pulse is large enough($< 0.5\ \mu A/cm^2$) to excite the neuron's membrane. then continuous spiking (red circle) will occur.

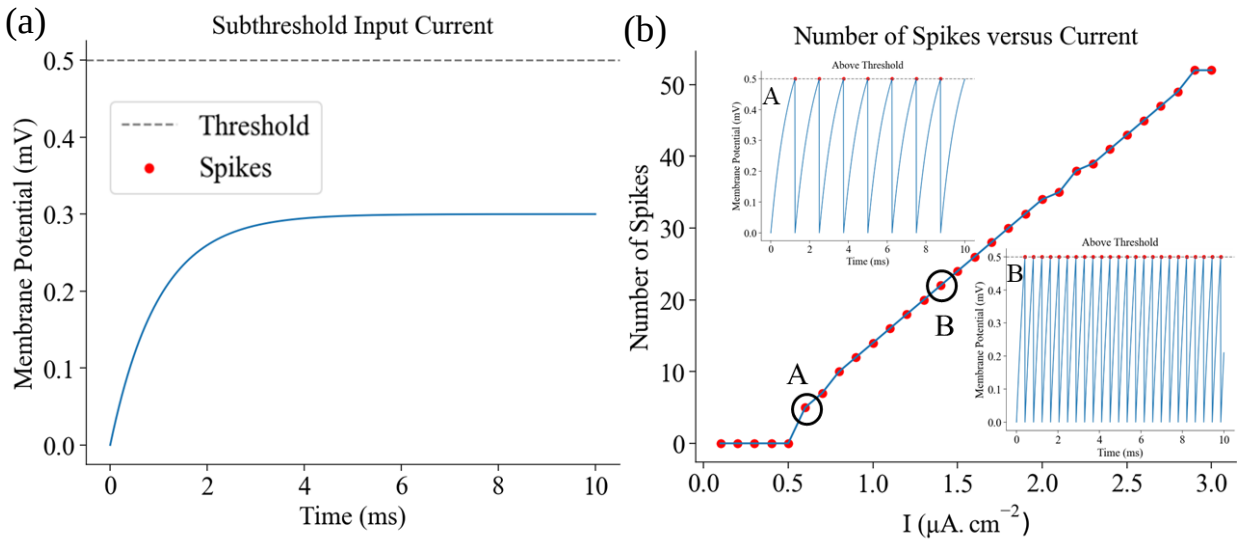

Figure 6.6 Membrane potential of a LIF neuron at (a) constant current $I \leq 0.5 \mu A/cm^2$, where no spikes are fired. (b) For increasing current the number of fired spikes increase, as (A) shows 7 spikes for $I = 0.7\ \mu A/cm^2$, and 24 spikes for $I = 1.5\ \mu A/cm^2$.

Fig. 6.6(b), shows that number of fired spikes depends widely on the value of applied pulse, so considering different current values changing between $0 \leq I \leq 3\ \mu A/cm^2$, we observe that higher current means more spikes from zero spikes in absence of current into 50 spikes at $3\ \mu A/cm^2$.

Many aspects play in the nature and sequence of the fired spikes, considering a ramp input stimulus will produce action potentials with an increasing firing rate (**Fig. 6.7(a)**) as the input strength increases. This behavior is described in **Fig. 6.7(b)** where the interspike interval (time interval between each consecutive spikes) decreases exponentially from 0.8 ms to 0.1 ms, as the applied current increases.

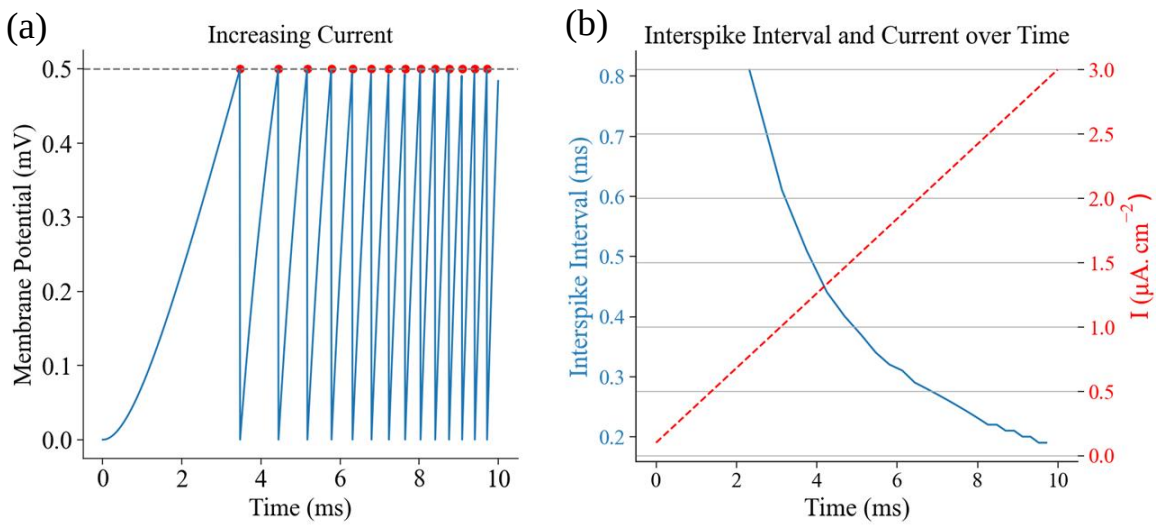

Figure 6.7 (a) The membrane potential versus time under the influence of an increasing current $0 \leq I \leq 3\ \mu A/cm^2$. (b) The variation of the interspike interval between consecutive action potentials as function of current and stimulus time.

6.4.2 Hodgkin-Huxley Model

In 1952, Hodgkin and Huxley performed experiments on the giant axon of the squid and found three different types of ions current: sodium, potassium, and a leak current that consists mainly of Cl− ions. They used a set of differential equations to describe the dynamic behavior of these ion channels.

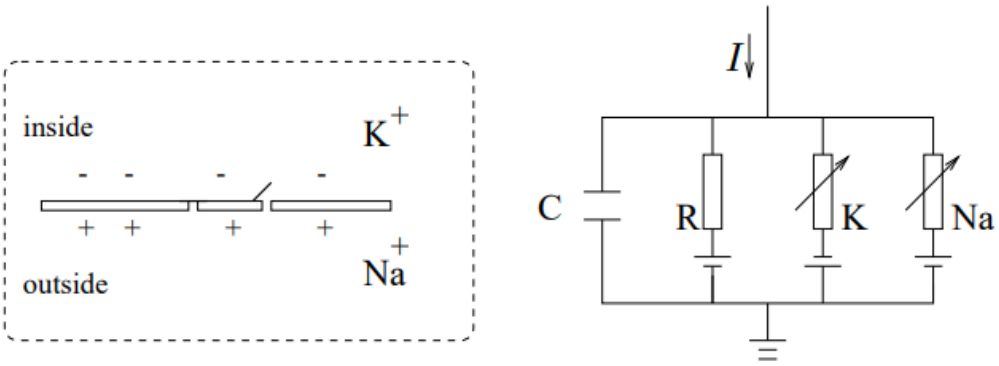

Figure 6.8 Schematic diagram for the Hodgkin-Huxley model [218].

The semipermeable cell membrane separates the interior of the cell from the extracellular liquid and acts as capacitor C. If an input current *I*(t) is injected into the cell, it may add further charge on the capacitor, or leak through the ion channels in the cell membrane. Because of active ion transport through the cell membrane, the ion concentration inside the cell is different from that in the extracellular liquid. Each ion channel is represented by a resistor as shown in **Fig. 6.8**. The resistance of sodium, potassium and leakage channel indicated by respectively R_{Na}, R_K, and R. We denote the potential across this membrane by *u*. Moreover, the Nernst potential generated by the difference in ion concentration is represented by a battery.

The current *I*(t) flowing in the circuit can be splitted as below,

$$I(t) = I_C + \sum_k I_k(t) \quad (6.5)$$

With I_c is the current passing through the capacitor and can be written as, $I_C = C\ du/dt$, hence,

$$C\frac{du}{dt} = -\sum_k I_k(t) + I(t) \qquad (6.6)$$

the sum runs over all ion channels and is given by,

$$\sum_k I_k(t) = g_{Na}m^3h(u - E_{Na}) + g_K n^4(u - E_K) + g_L(u - E_L) \qquad (6.7)$$

The parameters E_{Na}, E_K, and E_L are the reversal potentials. Reversal potentials and conductance are empirical parameters. These values are based on a voltage scale where the resting potential is zero. To get the values accepted today, the voltage scale must be shifted by -65 mV. For example, the corrected value of the sodium reversal potential is E_{Na} = 50 mV, that of the potassium ions is $E_K = -77$ mV.

The activation of each channel of the model in terms of voltage-dependent transition rates α and β is given as:

$$\dot{m} = \alpha_m(u)\,(1 - m) - \beta_m(u)\,m$$

$$\dot{n} = \alpha_n(u)\,(1 - n) - \beta_n(u)\,n \qquad (6.8)$$

$$\dot{h} = \alpha_h(u)\,(1 - h) - \beta_h(u)\,h$$

With $\dot{m} = dm/dt$, and so on. The terms m and h are controlling variables for the sodium channel while the potassium channels constrained by the term n. Here $\dot{m}$, $\dot{n}$ and $\dot{h}$ are respectively the derivative of the m, n and h with respect to the time. The various functions α and β, given in **Table 6.2**, are empirical functions of *u* that have been adjusted by Hodgkin and Huxley to fit the data of the giant axon of the squid.

x	**E_x**	**g_x**
Na	115 mV	120 mS/cm^2
K	-12 mV	36 mS/cm^2
L	10.6 mV	0.3 mS/cm^2

x	α_x(u / mV)	β_x(u / mV)
m	(0.1 − 0.01 u) / [exp(1 − 0.1 u) − 1]	0.125 exp(−u / 80)
n	(2.5 − 0.1 u) / [exp(2.5 − 0.1 u) − 1]	4 exp(−u / 18)
h	0.07 exp(−u / 20)	1 / [exp(3 − 0.1 u) + 1]

Table 6.2 The parameters of the Hodgkin-Huxley equations. The membrane capacity is C = 1μF/cm^2 . The voltage scale is shifted so that the resting potential vanishes.

As shown in the Hodgkin-Huxley circuit (**Fig. 6.8**), electrical activity in neurons is sustained and propagated by ion currents (Na^+, K^+) through neuron membranes. The Na^+ and K^+ ions are considered to flow through ion channels where a series of gates determine the conductance of the ion channel. The macroscopic conductance of the Hodgkin & Huxley model arises from the combined effects of many microscopic ion channels embedded in the membrane. Each individual ion channel can be thought of as containing one or more physical gates that regulate the flow of ions through the channel. According to **Fig. 6.8**, the current flowing in the circuit is $I_{ext}=I_L+I_{Na}+I_K+I_m$, this can better be presented in terms of current density $J_{ext}=J_L+J_{Na}+J_K+J_m$.

6.4.2.1 Dynamics

Considering the summation of current mentioned above and the **Eqs. (6.5-6.8)**, in addition to the parameters given in **Table 6.2**, we can give a clear image of the dynamic of the H-H neuron model under different conditions. Note that in our simulations we denoted the applied current density ($\mu A/cm^2$) by *I*.

(c)

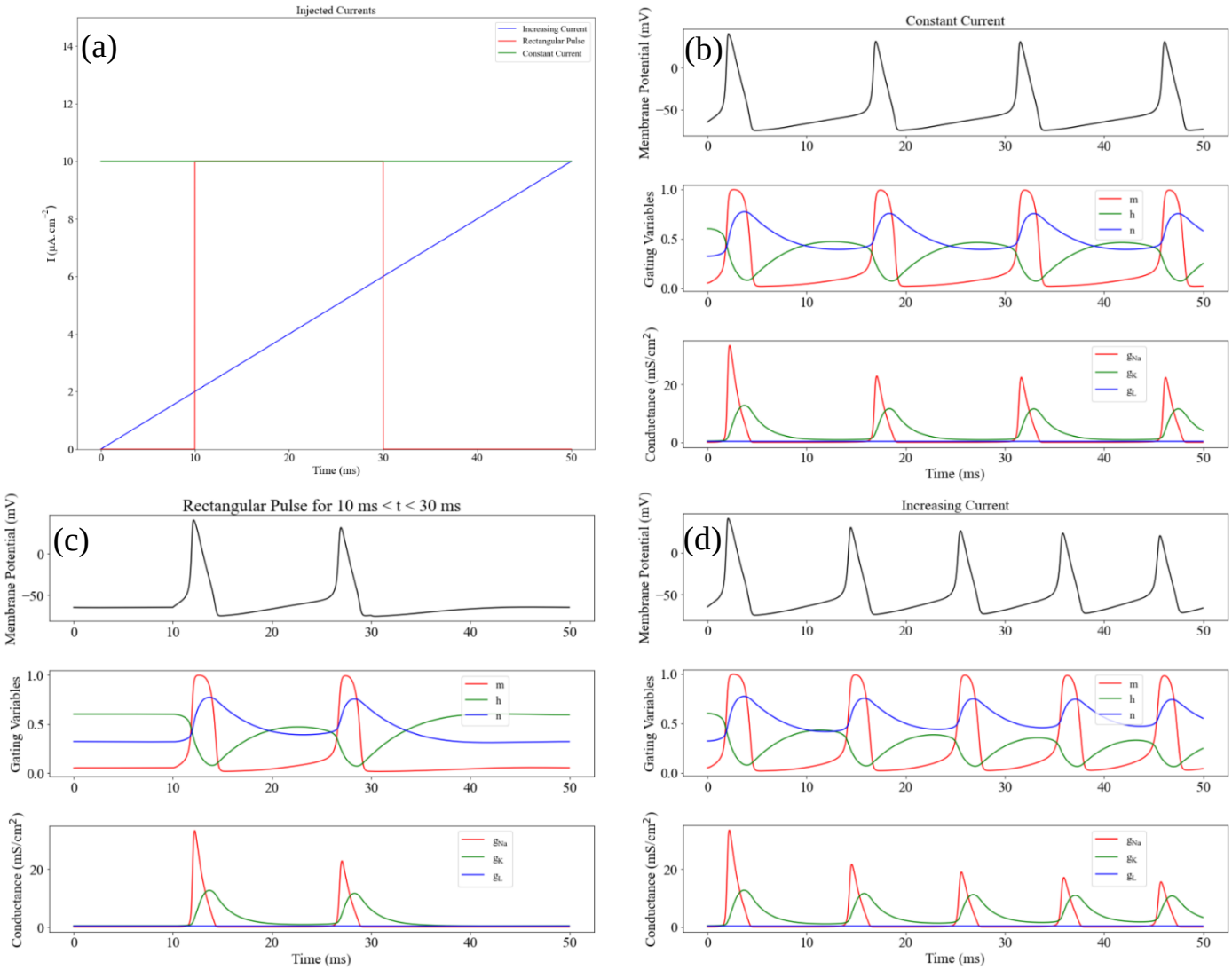

Figure 6 9 (a) Three different pulses are considered for a simulation time of 50 ns, Variation of action potential, gating variables n, m and h , and conductance for (b) constant current I =10 $\mu A/cm^2$, (c) rectangular pulse between 10 ms < t < 30 ms, (c) and for an increasing current with slope of 0.5.

In **Fig. 6.9(a)** three different current densities are considered through the ion channels and the membrane. A constant current I=10 $\mu A.cm^{-2}$ leads to the generation of four consecutive spikes with equal interspike interval t_{int} = 10 ms (**Fig. 6.9(b)**), and each spike is followed by a drop into the rest state. A smooth variation of ion channels conductance is observed, and this goes back to the behavior of (d) the gate variables **n**, **m** and **h** and the conductance for potassium and sodium as functions of time. The conductance of sodium channels

increases due to increasing **m**. As a result, positive sodium ions flow into the cell and raise the membrane potential even further. If this positive feedback is large enough, an action potential is initiated. At high values of membrane potential (u), the sodium conductance is shut off due to the factor h. The time constant for **h** is always larger than **m**.

In **Fig. 6.9(c)**, a rectangular pulse applied (I =10 $\mu A/cm^2$) for 10 ms < t < 30 ms, where outside this range zero current is considered. For the first 10 ms, the membrane potential does not change with time t as du/dt = 0. Only in the time domain of the applied pulse, action potentials will be generated. For this case the current flow in the ion channels seems to be continuous, being positive in the potassium ion channel as the K^+ ions move from inside to the outside of the cell whereas the sodium current is negative as Na^+ ions move into the cell across the membrane. The rise in the sodium conductance and fall occurs more rapidly for Na^+ than for K^+ mainly due to the behavior of the gate variables **m** and **h**. *We* see that **m** and **n** increase with increasing u whereas **h** decreases.

The H-H neuron shares the same behavior as that of the LIF neuron under the influence of a continuously increasing current (**Fig. 6.9(d)**), where it can be represented as I ($\mu A/cm^2$) = 10 + 0.5 × t (ms). Several spikes will be fired, but the with varied interspike interval changing from about 12 ms between the fires two spikes into 7 ms between the last two.

6.5 Neural Coding

Spiking neural networks employ precise timing of spikes for transferring information. Various procedures for converting input data to an understandable stimulus for SNN proposed, here we discuss different techniques of neural coding.

6.5.1 Rate vs Temporal Coding

The rate coding refers to encoding the input to a stimulus in terms of firing rate or frequency of action potentials. The concept of mean firing rates has been successfully applied during the last 80 years. It dates to the pioneering work of Adrian [219,220] who showed that the firing rate of stretch receptor neurons in the muscles is related to the force applied to the muscle. The mean firing rate is given by,

$$\nu = \frac{n_{sp}(T)}{T} \qquad (6.9)$$

With $n_{sp}(T)$ being the number of spikes that occur in a time window T. The unit of firing rate is reported in units of s^{-1} or Hz.

However, studies suggest that the human brain employs a different procedure for interpreting visual stimuli considering the response time of the visual receptors to these stimuli, which is remarkably short, and no time will remain for ascertaining the average firing rate by the neural system. Thus, temporal coding is a type of neural coding which relies on precise timing of action potentials or inter-spike intervals and the timing of individual spikes is equivalently important [221]. Unlike rate coding, the temporal coding

model tries to account for short-term stimuli producing a small number of spikes. Several applications have been based on temporal coding including, auditory systems [222].

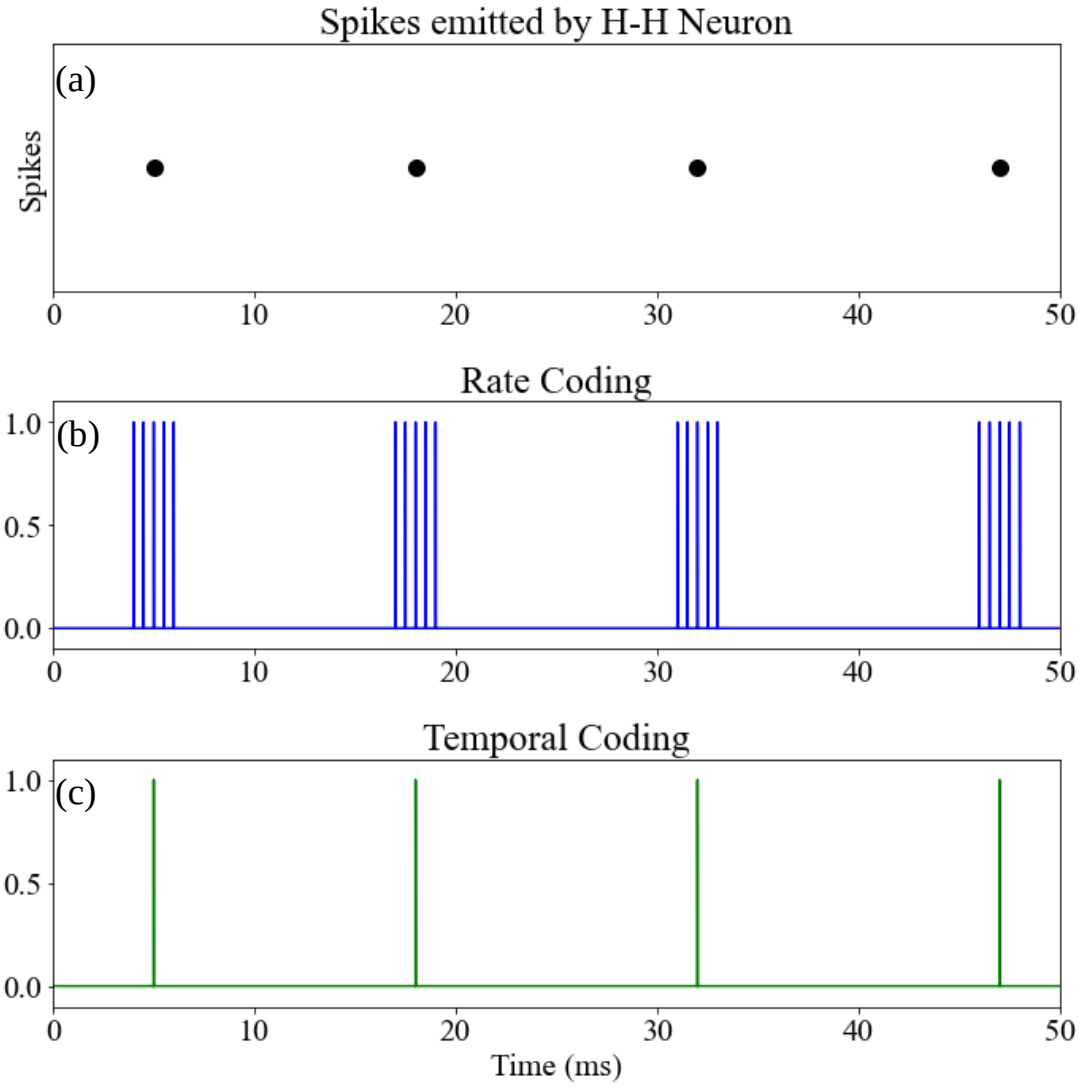

Figure 6.10 (a) Four spikes emitted by H-H neuron at constant current. These spikes are encoded based on two paradigms, (b) rate coding and, (c) Temporal coding.

For better understanding, we considered in **Fig. 6.10(a)** the four action potentials generated by the H-H neuron (back to **Fig. 6.9(b)**), in case of rate coding each spike will be encoded by a region of high frequency as shown in **Fig. 6.10(b)**, where we detect four regions of high frequency going back to each spike. Whereas based on temporal coding the spikes will be encoded by their time of emission, as shown in **Fig. 6.9(c)**.

6.5.2 Population Coding

In opposition to rate and temporal coding, which consider the firing rate of an individual neuron, population coding is a means by which information is coded in a group of neurons. All neurons in the population should have the same pattern of input and output connections.

One famous population coding model is the "population vector" model from a 1986 paper by Georgopoulos [223], proposed to describe motor neuron tuning in primary motor cortex. In this model, each neuron in the population has a preferred movement direction, and the resulting movement is a weighted average of the preferred movements, where the average is weighted by firing rate.

6.6 Noise in Spiking Neuron Models

In *vivo* recordings of neuronal activity are characterized by a high degree of irregularity. The spike train of individual neurons is far from being periodic and relations between the firing patterns of several neurons seem to be random. Although several studies investigated the effect of noise in SNNs [224,225], but the origin of this irregularity is still poorly understood. We can distinguish between intrinsic and extrinsic noise sources. Intrinsic noise generates stochastic behavior on the level of the neuronal dynamics.

A source of noise, which is literally omnipresent, is thermal noise. Since neuronal dynamics is described by an equivalent electrical circuit containing resistors R, the neuronal membrane potential fluctuates at finite temperature. Another source of noise that is specific to neurons arises from the finite number of ion channels in a patch of neuronal membrane [226]. Apart from intrinsic noise, the extrinsic noise arises from network effects and synaptic transmission [227]. Synaptic transmission failures, for instance, seem to impose a substantial limitation to signal transmission within a neuronal network. Experiments with double electrode recordings from two synaptically connected neurons suggest that only 10–30 percent of presynaptic spikes generate a postsynaptic response [228].

In **Fig.6.11** below, we show the effect of noise on the membrane potential of LIF and H-H neurons, where we considered a constant mean current $I = 20\ \mu A.\ cm^{-2}$, and noise is added using the **rand** function (**Fig.6.11(a)**). In the case of LIF neurons, the noise seems to cause a delay in the spike generation, by resisting the membrane from reaching the threshold easily (**Fig.6.11(b)**). However, it will not affect the spike timing of the H-H model as shown in **Fig.6.11(c)**, but it will leave its stump by perturbing the refractory period.

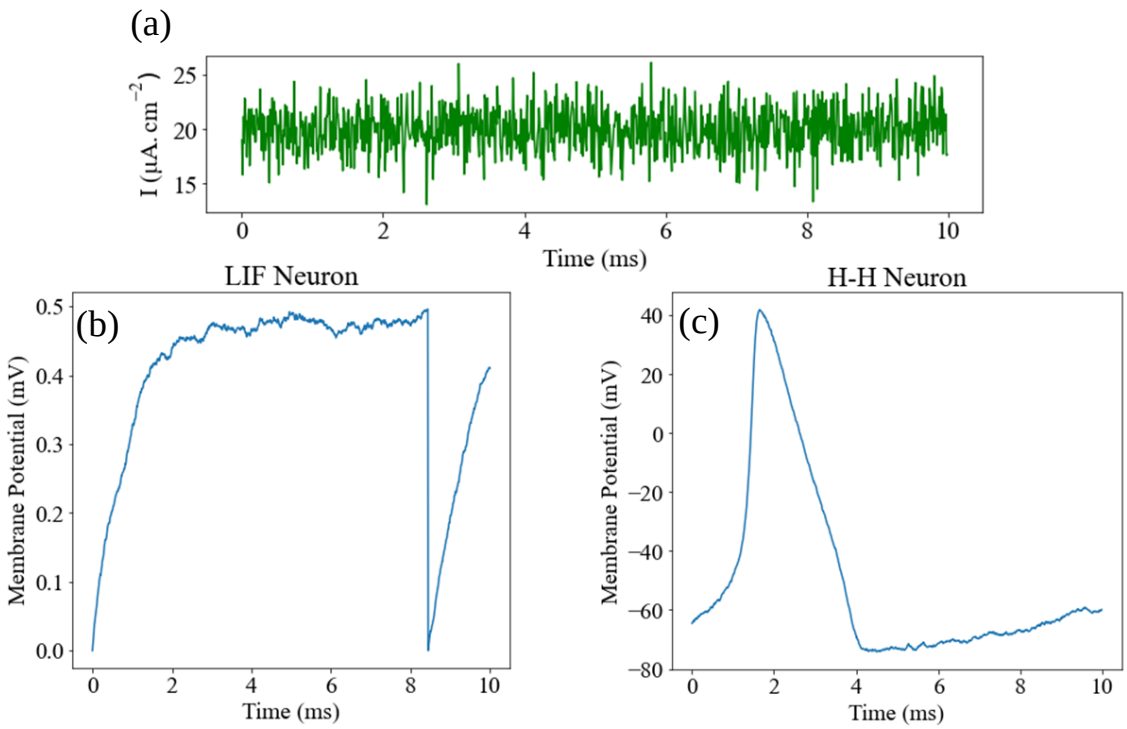

Figure 6.11 (a) A noisy pulse current is injected into, (b) a LIF neuron firing a noisy spike with a delayed firing time. (c) A H-H neuron shows a little disturbance in the refractory period of the action potential.

6.7 Supervised and Unsupervised Learning in SNN

In contrast to supervised learning where the network parameters optimized for every input stimulus to achieve the least error, unsupervised learning refers to the change of synaptic connection according to the statistics of the input stimuli [218].

6.7.1 Supervised Learning

The first supervised algorithm which used a gradient-based technique to transfer information in the timing of a single spike was SpikeProp [229]. In this model, each neuron can produce at most one action potential during the spike interval. If the neuron fires more than one spike during the period, the algorithm only considers the first spike as the exact firing time. The model is comprised of the connections with different synaptic delays and weights, which enable them to solve linearly inseparable problems (like XOR function) and attain high-grade results on the problem with a small dataset. However, having multiple connection weights per synapse and adopting a single spike optimization procedure restricted its application to the problems with small datasets. McKennoch, Liu, and Bushnell [230] proposed the method to enhance the convergence rate of the SpikeProp, though their approach was not expandable to large datasets. An alternative method to

SpikeProp proposed in [231] which specially designed for non- leaky integrate and fire models. The model replaced the multi delay elements of the SpikeProp model with an exponential connection between each pair of neurons. The model replaced the multi delay elements of the SpikeProp model with an exponential synaptic connection between each pair of neurons. The single and two-layer model of the proposed network achieved test errors of 2.45% and 2.86%, respectively. The main associated problem with the proposed method is a dropout since most of the regularization techniques do not apply to the network and sometimes prevent neurons from firing. Stromatias and Marsland [232] used a different approach than the previous works and employed the genetic algorithm to optimize multiple spikes of each neuron instead of considering only the first spike. However, this method only applies to small networks with less than ten neurons in the hidden layer. One of the main reasons is the limitation of the genetic algorithm for scaling problems with so many parameters. Lee, Delbruck, and Pfeiffer [233] proposed a different method for optimizing multiple spikes of the neuron, assuming the output of the neuron as a linear function of its input. This simplification allows them to train the network in the forward direction and still can perform backpropagation (BP) in the backward direction. The method ignores the refractory period following the generation of a spike and uses the property of lateral inhibition to enhance the performance of the network. Despite all the simplification, the model is still able to achieve good results on the MNIST dataset, obtaining a test error of 1.30% using stochastic gradient descent.

6.7.2 Unsupervised Learning

During recent years, various strategies for unsupervised learning in spiking neural networks developed, which are often based on variants of the Hebbian method. Inspired by Hopfield's idea, Natschlager and Ruf [231] introduced an unsupervised clustering method in spiking neural networks. Their approach is analogous to the radial basis function (RBF) except the input, which is in terms of spike timing. A winner-takes-all learning rule used to adjust the synaptic weights between the source neuron and the first firing neuron in the target layer. If the start of the postsynaptic potential occurs immediately before the spike in the target neuron, the weights of the synapse will increase. On the other hand, the synaptic weights of the earlier and later synapses will decline, which indicates their negligible impact on the firing of the target neuron. Employing this learning procedure, we can encode input patterns into synaptic weights in such a way, the spike timing of the output neurons indicates the difference between the evaluated pattern and the learned input pattern, which is quite like unsupervised learning in RBF neuron.

To improve accuracy and expand the clustering capacity of the Natschlager and Ruf network, Bohte [199] applied a temporal version of population coding. He applied multiple receptive fields to encode the input data into temporal spike-time patterns. Bohte proved using such an encoding technique, spiking neural networks can perform efficient clustering tasks. **Fig. 6.12** presents the unsupervised SNN proposed by Natschlager and Ruf in which individual connection is considered as multi-synaptic. The weights are random, and a set of increasing delays introduced to facilitate unsupervised learning of input patterns. Querlioz and his colleagues[234] introduced a simplified and customized spike time-

dependent plasticity (STDP) scheme for unsupervised learning in memristive devices. Their network comprised of an unsupervised layer that extracts features of the input's images utilizing a rectangular shape of STDP and achieves accuracy comparable to traditional supervised learning models with the same number of parameters. They employed homeostasis and lateral inhibition to encourage competition among neurons.

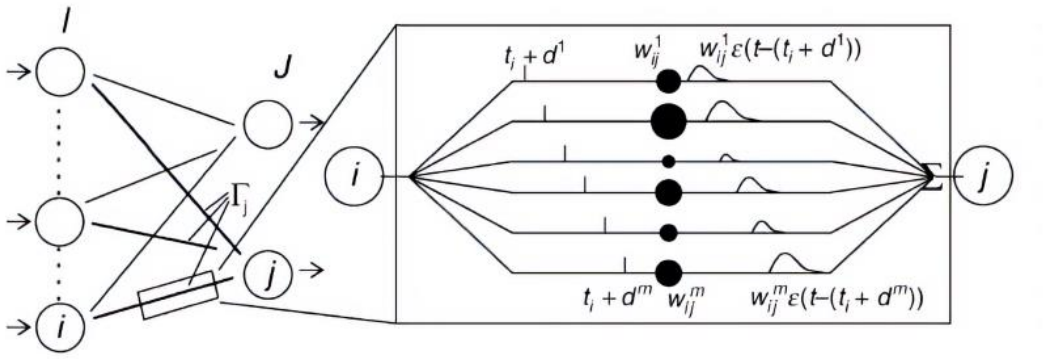

Figure 6.12 Unsupervised learning rule in SNN proposed in [231]

Diehel and Cook [235] proposed an unsupervised method for digit recognition using a conductance-based model of leaky integrate and fire neuron. They introduced an adaptive threshold method which prevents a neuron from dominating the response to the input pattern and facilitates the competition among neurons. Using 3600 excitatory neurons, they obtained an accuracy of 95% on the handwritten digits of the MNIST dataset. Their model consists of the same number of inhibitory neurons in the output layer. The neurons in the excitatory layer are connected in a one-to-one fashion to the corresponding inhibitory neuron in the output layer. The neurons in the inhibitory layer connect to all the other neurons in the excitatory layer except their corresponding neuron in the excitatory layer (See **Fig. 6.13**). This architecture allows them to use the property of lateral inhibition in which the first firing neuron inhibits all the other neurons in the output layer plus their corresponding excitatory neuron. Lateral inhibition enables the neuron to adapt its weights according to the input pattern.

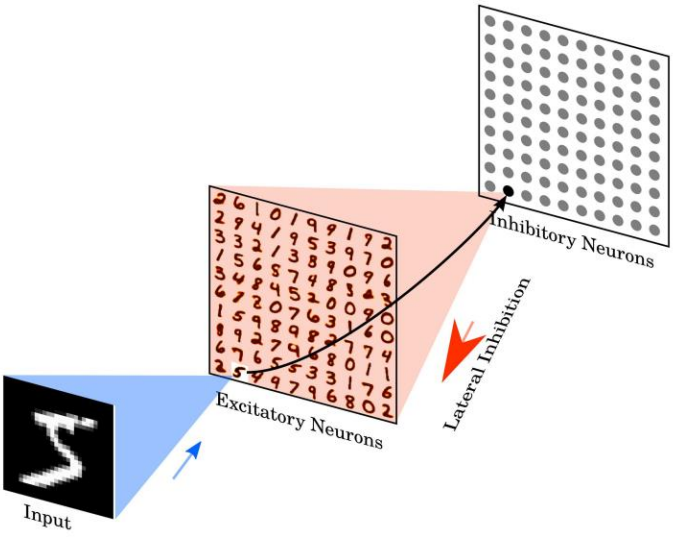

Figure 6.13 Architecture of the Diehel & Cook network [235].

6.8 Synaptic Plasticity

Experiments confirm that the amplitude response of a postsynaptic neuron is not fixed and changes over time. In neuroscience, this change of synaptic strength is referred to as synaptic plasticity. If a persistent strengthening of synapses observed, the effect described as long-term potentiation of synapses (LTP). In opposition to long-term potentiation is long-term depression (LTD) when we witness a reduction in the efficacy of neuronal synapses. In 1949 Hebbs [236] described the change procedure in connection from presynaptic neuron A to a postsynaptic neuron B by his famous postulate:

"When an axon of cell A is near enough to excite cell B or repeatedly or persistently takes part in firing it, some growth process or metabolic change takes place in one or both cells such that A's efficiency, as one of the cells firing B, is increased".

Today, 50 years later, this famous postulate is often rephrased in the sense that modifications in the synaptic transmission efficacy are driven by correlations in the firing activity of pre- and postsynaptic neurons.

6.8.1 Mathematical Formulation of Hebb's Rule

To find a mathematically formulated learning rule based on Hebb's postulate we focus on a single synapse with efficacy $\mathbf{w_{ij}}$ that transmits signals from a presynaptic neuron **j** to a postsynaptic neuron **i**. In the following, the activity of the presynaptic and postsynaptic neurons is described by the firing rate ν_j and ν_i respectively. According to Hebb's postulate the change in synaptic efficacy is characterized by two properties *Locality* and *Cooperativity*. This mean that the efficacy change depends on local variables available

including the firing rates of pre- and postsynaptic neurons and thus the efficacy change is given by,

$$\frac{d}{dt}w_{ij} = F(w_{ij};\ \nu_i, \nu_j) \qquad (6.10)$$

Here, $\frac{d}{dt}w_{ij}$ denote the rate of change in synaptic strength, and *F* is a function that describes the synaptic change based on the local variable [237–239].

The second important aspect of Hebb's postulate, cooperativity, implies that pre- and postsynaptic neurons must be active simultaneously for a synaptic weight change to occur. We can use this property to learn something about the function F. If F is sufficiently well-behaved, we can expand F in a Taylor series about $\nu_i = \nu_j = 0$,

$$\frac{d}{dt}w_{ij} = c_0(w_{ij}) + c_1^{post}(w_{ij})\nu_i + c_1^{pre}(w_{ij})\nu_j + c_2^{pre}(w_{ij})\nu^2_j + c_2^{post}(w_{ij})\nu^2_i + c_2^{corr}(w_{ij})\nu_i \nu_j + \mathcal{O}(\nu^3) \qquad (6.11)$$

The term containing c_2^{corr} on the right-hand side of **Eq. (6.10)** is bilinear in pre- and postsynaptic activity. The simplest choice for our function F is to fix c_2^{corr} at a positive constant and to set all other terms in the Taylor expansion to zero. The result is the prototype of Hebbian learning,

$$\frac{d}{dt}w_{ij} = c_2^{corr}(w_{ij})\nu_i \nu_j \qquad (6.12)$$

6.8.2 Spike-Time Dependent Plasticity

In this section we study the synaptic efficacy on the level of individual spike and focus on changes in the synaptic efficacy that are driven by temporal correlations between presynaptic spike arrival and postsynaptic firing. This biological process that adjusts the strength of connections between neurons in the brain is known as Spike Time Dependent Plasticity (STDP). Assume that t_{pre} and t_{post} are respectively the time in which pre and postsynaptic spike happen. The change in synaptic weight is a function of temporal difference $|\Delta t| = |t_{post} - t_{pre}|$. Thus, we define a 'learning window' as,

$$\Delta w_+ = A_+(w) \cdot \exp(-|\Delta t|/\tau_+) \text{ at } t_{post} \text{ for } t_{pre} < t_{post}$$

$$\Delta w_- = A_-(w) \cdot \exp(-|\Delta t|/\tau_-) \text{ at } t_{pre} \text{ for } t_{pre} > t_{post} \qquad (6.13)$$

Where $A_\pm(w)$ represents the update dependency on the current value of the synaptic weight. $A_+(w)$ and $A_-(w)$ normally have a positive and negative value respectively. Whenever a presynaptic and postsynaptic spike happens, we need to update the synaptic weight. **Fig. 6.14** presents the diagram of spike-timing-dependent plasticity. The STDP rule describes the changes in synaptic weights as a function of timing of pre and postsynaptic spikes. Considering now we have two sets of spike trains $S_i(t)$ and $S_j(t)$, the efficacy change will be given as follow:

$$\frac{d}{dt}w_{ij} = \mathrm{S_j(t)}\,[a_1^{pre} + \int_0^{\infty} A_{-}(w_{ij})W_{-}(s)S_i(t-s)ds] + S_i(t)\,[a_1^{post} + \int_0^{\infty} A_{+}(w_{ij})W_{+}(s)S_j(t-s)ds] \qquad (6.13)$$

Here a_1^{pre} and a_1^{post} are non-Hebbian parameters and $W_{\pm}(s)$ represent the time scale of the learning window [240].

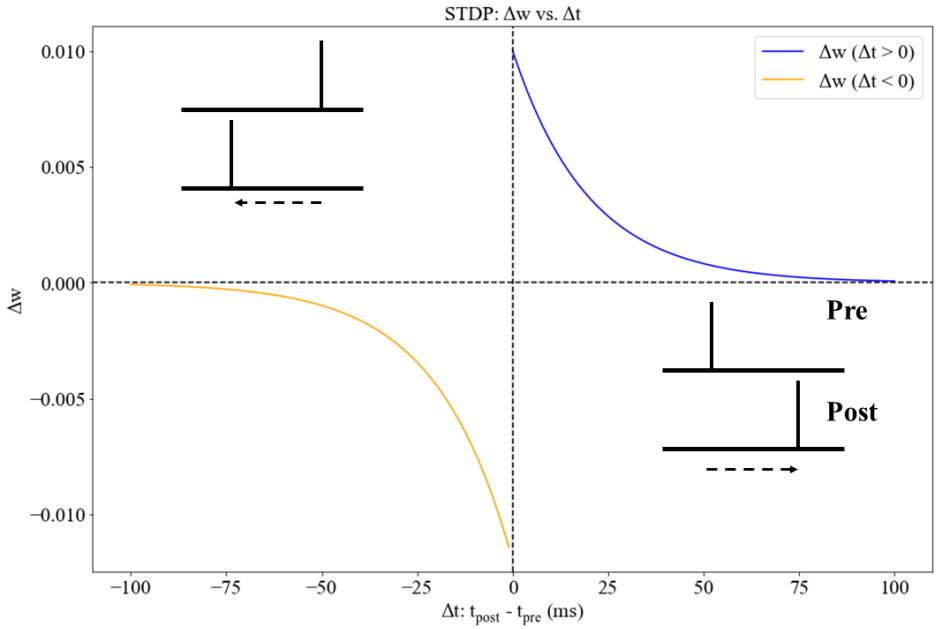

Figure 6.14 Representation of the spike-timing-dependent plasticity (STDP) learning rule. The strength of the connection (synaptic weight) is adjusted based on the timing of pre- and post-synaptic spikes. For $\Delta t > 0$, Δw is positive, indicating an increase in synaptic weight, whereas, for $\Delta t < 0$, Δw is negative, indicating a decrease in synaptic weight.

Several studies have developed several SNNs using STDP and stochastic gradient descent. Spiking networks consisting of many spiking neurons equipped by spike-based synaptic plasticity rules have shown success in different fields with varying percentages of accuracy. **Table 6.3** below shows some applications of spiking neural networks based on STDP learning.

Data	Training	Neural Coding	Accuracy
MNIST	STDP	Rate	96.5% [241]
Caltech face &	Unsupervised-STDP	Temporal	99.1% [242]

motor bike			
CIFAR 10	Unsupervised-STDP	Temporal	93% [243]

Table 6.3 Applications of spiking neural networks trained by STDP based on different neural coding paradigms and data sets.

Chapter 7

MTJ-Based Synapse

The human brain is an incredible pattern-matching machine

Jeff Bezos

“MTJ-based Spiking Neural Networks (SNNs) herald a new era in neuromorphic computing, where the fusion of magnetic and neuronal dynamics enables unprecedented efficiency and scalability..

— Unkown”

”

This is the last chapter, where section 7.1 serves as introductory background about importance of MTJ in neuromorphic applications. In section 7.2 we introduce our proposed MTJ device, and the micromagnetics deriving it. To understand the functionality of our MTJ synapse, section 7.3 will present different device aspects. As a continuation, a systematic study was performed in section 7.4 to show the spiking behavior under different conditions. In section 7.5 a SNN was designed based on the MTJ synaptic device. Finally, section 7.6 sums up the entire work.

7.1 Introduction

Magnetic tunnel junctions (MTJs) have been investigated for neuromorphic computation where they have already shown to mimic synapse plasticity and firing [10,22,23,244,245]. Recently, MTJ-based devices have been proposed to emulate the Leaky-Integrate-and-Fire (LIF) model of neurons which has low computational costs [10,244,246]. These MTJ-based proposals rely solely on the magnetization dynamics generated by a series of pulses, which when integrated over time produces a single switch of the magnetization. A common caveat of these proposals is the requirement of a reset current pulse in the opposite direction to return the MTJ to the initial condition. The need for a reset mechanism also implies a clocking system which significantly reduces computational speed. To overcome the need of a resetting system, it has been proposed to use MTJs in the stochastic regime, where the magnetization switches between the maximum and minimal resistance configuration due to thermal fluctuations [247,248]. This paradigm suffers from the fact that true spikes are not obtained, since the switch of the magnetization is not immediately followed by the reverse switching. Moreover, the highly stochastic nature of these devices leads to a high error rate which significantly increases the computational time. Other proposals that do not require a resetting mechanism involve the use of antiferromagnetic materials [178,179]. These proposals, however, suffer from the need of a single domain ground state and, in the case of true sharp spikes, the presence of an applied alternate current [178]. A recent spiking MTJ-based proposal has shown that combining the stochastic behavior and ferro-antiferromagnetic coupling allows for the emulation of spiking with single pulses without the need for a resetting pulse [249]. Despite these advances towards the hardware implementation of the computationally cheap LIF model, a scalable room-temperature device that emulates more bio-realistic neuron models is still lacking. As we showed in **Chapter 6**, the Hodgkin-Huxley model can mostly mimic the efficiency of the brain, and the firing behavior derives from the combination of the different response times of physical processes in the neuron.

Model	H-H Neuron	MTJ Device
Output	In terms of membrane potential	In terms of electrical resistance of device
Physical Mechanism	Interplay between the concentrations of Na+, K+ , and leakage currents	Interplay between magnetization dynamics and thermal effects

Neuron Behavior	Tonic spiking of the voltage at constant input current	Tonic spiking of the voltage at constant input current
Firing Rates	1-10 KHz [213,262–265]	100 MHz - 5 GHz
Applied Voltage	1-200 Mv [213,265]	100-300 mV
Refractory Period	Present	Present

Table 7.1 A comparison between H-H model and the single MTJ device. The performance of the single MTJ device is based on experimental results [250].

In this chapter we propose a single MTJ device that emulates bio-realistic neurons that fire at frequencies in the MHz to GHz range by leveraging thermal effects and Joule heating. The device produces sharp firing signals followed by a refractory period, which is essential for the implementation of bio-realistic learning processes such as STDP. We show that with a single constant input the device at room temperature fires at constant rate and presents a small, but not vanishing, stochasticity due to the thermal field [251]. A single firing response can also be obtained by integrating discrete pulses and thus the device also emulates the LIF model. The proposed device employs a single MTJ, which renders it CMOS-compatible, compact, robust, scalable, and reproducible as required for SNNs. In **Table 7.1** a brief comparison is made between the H-H model and our proposed MTJ device.

7.2 Device and Model

This section is divided into two subsections, where we define the device designed throughout our study, as well as the magnetic properties used in our micromagnetic study are also presented.

7.2.1 Device Properties

However, while the variation of the membrane potential in the biological neuron is due to the Sodium (Na^+), Potassium (K^+), and leakage currents, the variation of the potential through the MTJ corresponds to a change in the resistance and is induced by the input current and thermal effects. The active part of the MTJ proposed here has a hybrid configuration where the free layer equilibrium configuration of the magnetization is out-of-plane, and the polarizer is in-plane (See **Fig.7.1(a)**). As discussed extensively in the experimental work [250], this MTJ configuration has a distinct behavior compared to MTJs where the easy-axis of the free-layer is along the direction of the magnetization in the fixed layer. In this case, the auto-oscillation generated by the STTs induces an oscillation of the resistance since the free-layer magnetization rotates between a state of maximum and minimum resistance, i.e., antiparallel, and parallel to the polarizer respectively. The resistance variation in an MTJ generates the spiking behavior described in **Fig.7.1(b)**, which is characterized by a sharp change in resistance followed by a refractory period

where the resistance reaches the highest values. Experiments have demonstrated that this MTJ concept exhibits ultralow current density threshold (<10^6 A/cm^2) for the excitation of the auto-oscillation [250].

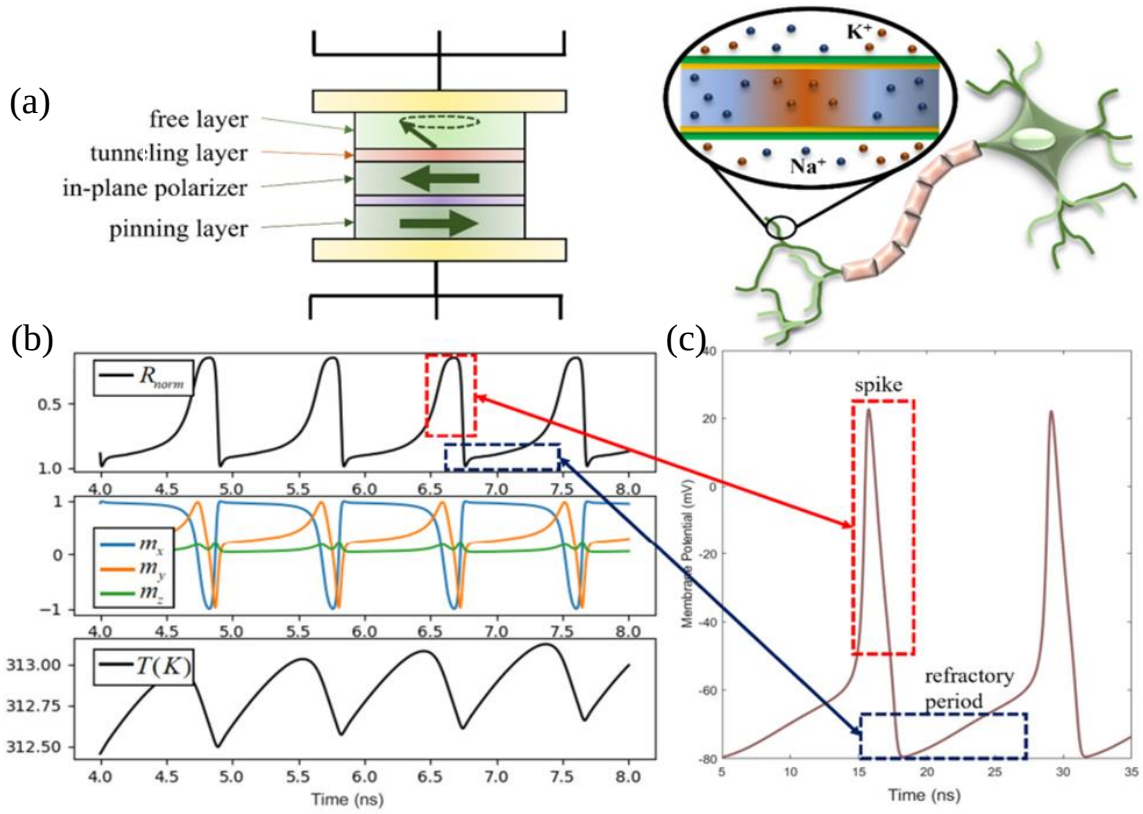

Figure 7.1 An MTJ implementation of bio-realistic firing behavior. (a) On the left we show a sketch of the device concept of the proposed MTJ synaptic device and on the right a sketch of a biological neuron. Both receive the input in terms of currents and produce an output in terms of voltage variation. In the spintronic device, the potential variation is due to changes in resistance produced by the input current and thermal effects. In the neuron, the potential variation is due to the Sodium (Na^+), Potassium (K^+), and leakage currents. (b) and (c) compare the resistance variation of the proposed MTJ device with the potential spiking in a biological neuron according to the Huxley-Hodgkin model. In (b) from top to bottom we show: the spikes in the resistance through the device; the dynamics of the magnetization components; the temperature variation of the device. (c) An example of a numerical simulation of the dynamics of a H-H neuron. It can be observed 6 that the behavior of a sharp firing signal followed by a refractory period is a common feature in both models.

The ultralow threshold is achieved by considering a polarizer composed of a synthetic antiferromagnet that allows for proper control of dipolar fields which drives a small tilting

of the equilibrium magnetization of the free layer at zero bias field. The relative resistance of the MTJ is given by,

$$R_{norm} = \frac{1+P^2}{1-P^2(\mathbf{m}\cdot p)} \quad (7.1)$$

Where **m** = M /M_s is unitary magnetization vector of the free layer, M_s is the magnetization saturation, P < 1 is the polarization and **p** is the direction of the spin-polarized current. Hence in the absence of spin-transfer torque (STT) [35,252,253], the resistance of the MTJ is not at a minimal (m and p in the same direction) or maximum (**m** and **p** in opposite directions) state since the magnetization of the free layer is perpendicular to the magnetization of the polarizer (**m**·**p** » 0). When a polarized spin-current along the maximum resistance direction is applied, the STT drives a large amplitude magnetization precession. To couple the magnetization dynamics with thermal effects, we consider three phenomena given below.

7.2.1.1 Resistance Variation Driven Gain-Loss

The first phenomenon is associated to the gain-loss of temperature of the MTJ driven by variations of the resistance,

$$\frac{dT}{dt} = \rho \frac{R_{norm}(JA)^2}{k_B} - \frac{(T-T_{amb})}{\tau_0} \quad (7.2)$$

Where T is the temperature of the MTJ, ρ is the heating efficiency, J is the applied current density, A is the area of the MTJ, k_B is the Boltzmann constant, T_{amb} is the room temperature, and τ_0 the natural temperature decay time of the MTJ. The coefficient depends on the maximum resistance of the device R_0, the thickness tb and thermal conductivity λ of the free layer.

7.2.1.2 Parameter Scaling

The second phenomenon is given by the temperature scaling of micromagnetic parameters, such as the magnetization saturation of the free layer and the polarization [193,254–257].

$$M_s(T) = M_{s,0}\left(1 - \left({}^{T}/_{T_c}\right)^{1.5}\right) \quad (7.3)$$

$$P(T) = P_0({}^{M_s(T)}/_{M_{s,0}})^{\varepsilon_P} \quad (7.4)$$

where T_c is the Curie temperature, $M_{s,0}$ and P_0 are the magnetization saturation and polarization, respectively, at T = 0K, and $\boldsymbol{\varepsilon_P}$ is a scaling coefficient.

7.2.1.3 Stochasticity

The third phenomenon is the thermal excitation of the magnetization in the free layer, which produces a stochasticity of the magnetization trajectory. The thermal excitation is incorporated as a temperature induced white noise, with magnitude [251,257].

$$h_{ther} = \sqrt{\frac{2k_B\alpha T}{M_s\gamma V\Delta t}} \qquad (7.5)$$

Where α is the phenomenological Gilbert damping, γ is the gyromagnetic ratio, V is the volume of the free layer and Δt is the simulation time step.

7.2.2 Micromagnetic Model

The overall design of the proposed device is shown in **Fig. 7.1(a).** Like a biological neuron, the device generates voltage spikes due to an applied current corresponding to the weighted sum of all signals received from other neurons.

We consider an MTJ of Ref. [250] with an MgO barrier sandwiched between a free layer with PMA and an in-plane magnetized fixed layer. The magnetization of the free layer is described by a single magnetization vector which evolves in time according to the Landau-Lifshitz-Gilbert (LLG) **Eq. (2.20)** of the main text. In our model the effective magnetic field, h_{eff}, is given by,

$$h_{eff} = -\mu_0 M_s\left(D_x\mathbf{m_x}\hat{x} + D_y\mathbf{m_y}\hat{y} + D_z\mathbf{m_z}\hat{z}\right) - H_F n_F \qquad (7.6)$$

where $\mathbf{m} = M/M_s$ is unitary magnetization vector of the free layer, M_s is the magnetization saturation, D is the effective anisotropy vector, and μ_0 is the vacuum permeability. We also consider an external field due to the coupling to the fixed layers with strength and direction given by H_F, proportional to the magnetization of the fixed layer, and n_F respectively. The thermal field H_{ther} is modelled by a Gaussian noise is given by **Eq. (7.5).**

(a)

Magnetic Parameters	Value
Saturation Magnetization (M_s)	8.47×10^5 A/m
Dipolar Field (H_F)	7.7 mT
Polarization Constant P(T)	0.78
Gilbert Damping (α)	0.01
Demagnetizing vector (D)	(0.1,0.2, -0.95)
Fixed layer magnetization direction (n_F)	(1, 0, 0)

(b)

Geometric & Thermal Parameters	Value
Area of Free Layer (A)	6.25×10^4 nm^2
Thickness of Free layer (d)	1.6 nm
Curie Temperature (T_c)	800 K
Ambient Temperature (T_{amb})	300 K

Temperature decay time (τ_0)	4 ns
Heat efficiency (B)	3.0×1014 K/Js
Polarization scaling coefficient (ε_P)	1.5

Table 7.2 (a) Magnetic and (b) geometric and thermal parameters used in the macrospin simulations at room temperature (T = 300 K).

7.3 Results

To understand the working principles of our MTJ-device different aspects were studied including the change in resistance and temperature of the device which is essential during the switching process. Moreover, the firing rate as a function of the applied impulse is also reported. The flexibility of our device allows it to emulate the behavior of not only Hodgkin-Huxley but also the LIF neurons.

7.3.1 Resistance and Temperature Relation

We first applied different currents to analyze the change in average resistance and average temperature. Two behaviors are observed as shown in **Fig. 7.2(a)**: in regions (i) and (iii) the magnetization is fixed by a strong bias given by the anisotropy or the STT, and (ii) where large amplitude auto-oscillations are excited. Notice that the variation of temperature is essential for the firing behavior, characterized by a switch between steady and auto-oscillating states. The alternation is due to the parameter scaling and the stochasticity as seen on the bottom of **Fig 7.2(a)**. **Fig. 7.2(b)** shows the average temperature in terms of applied current which is responsible for the parameter scaling and the amplitude of the thermally induced stochasticity. Moreover, we emphasize that the stochasticity of the device due to the thermal fluctuations also induce a small level of stochasticity of the firing behavior which is relevant for neuromorphic applications.

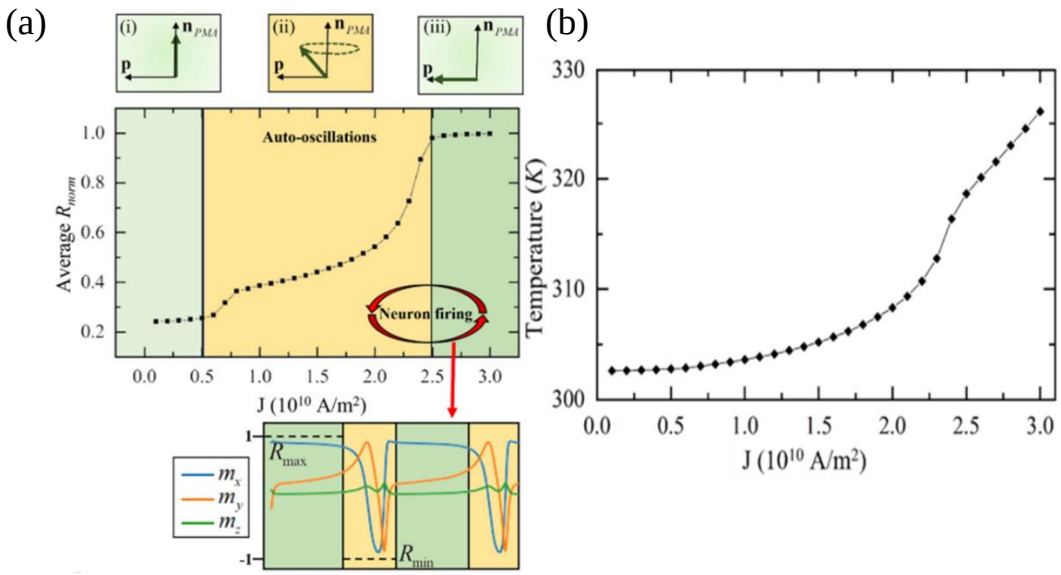

Figure 7.2 (a) and (b) show the dependence of the average normalized resistance and temperature as a function of the applied current density, respectively. On (a) we identify three regions where: (i) the magnetization is strongly biased towards the easy axis in the free layer (nPMA), (ii) there is an auto-oscillation around the easy-axis of the free layer (nPMA), (iii) the magnetization is strongly biased towards the direction of the magnetization in the polarizer (p).

7.3.2 Current-Controlled Frequency

Fig. 7.3(a) shows the spiking frequency as a function of the applied current density emulating the continuous firing under constant input. In **Fig. 7.3(a)** we selected two regions, the first region in **Fig. 7.3(b)** where one observes high frequency for low current densities, while lower frequency is observed for larger current densities as shown in **Fig. 7.3 (c)**. In ref.[39,258] this current-controlled frequency relation is justified as a result to the non-linear frequency shift linking the frequency and the power of the spintronics. Based on the parameters of **Table 7.2**, the range of firing frequencies is between 100 MHz and 3 GHz. Moreover, we notice in **Fig. 7.3(c)** that the period between spikes has small fluctuations associated with temperature induced noise, thus the time difference between spikes is not constant. This thermal induced stochasticity is essential for bio-realistic neural networks [4]. The other two thermal phenomena, i.e., the parameter scaling, and the resistance variation driven gain-loss, are responsible for another important feature of the observed dynamics: the characteristic refractory period. The lower output not only deters consecutive spikes as may also be used to tune the synapse weights.

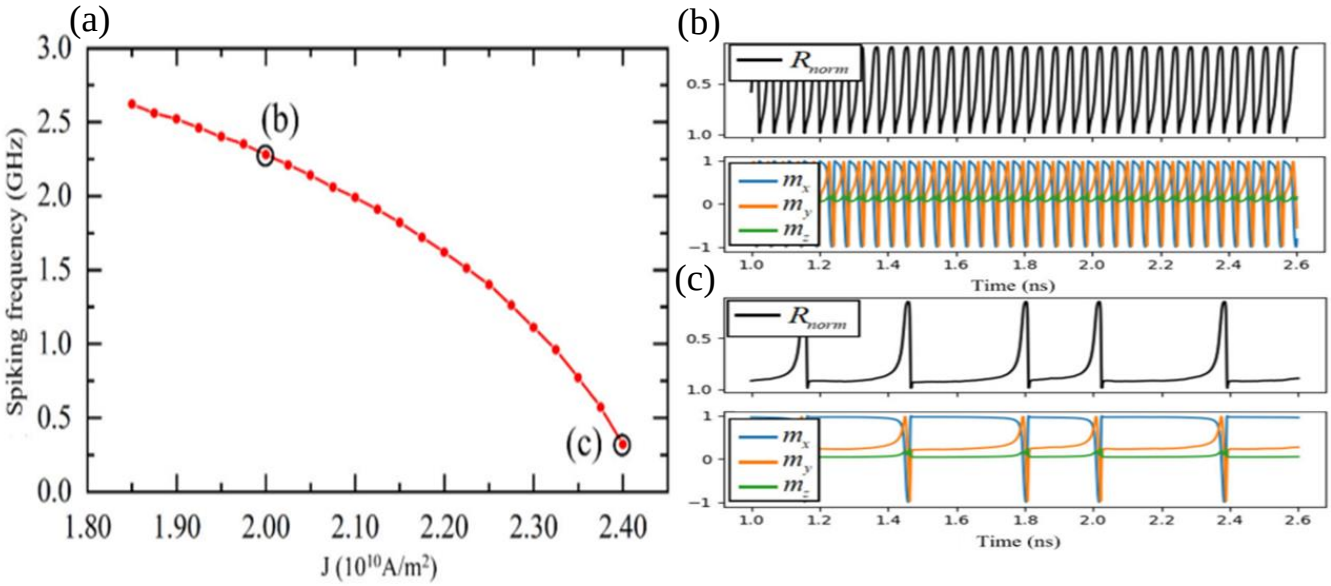

Figure 7.3 (a) Frequency of neuron firing as a function of the applied current density. (b) and (c) show the time domain behavior of the resistance (top), magnetization components and temperature (bottom) for low (2×10^{10} A/m^2) and high (2.4×10^{10} A/m^2) current density respectively.

7.3.3 Emulating LIF Neuron

Our proposed device works not only with the H-H model, but with current pulses within the LIF neuron model. In our simulations we considered a sequence of step current input characterized by size $\Delta\tau$ and amplitude $\Delta\iota$ that respect to higher bias current $J_0=2.5\times10^{10}$ A/m^2 showing no spikes **Fig. 7.4(a)-(b)**. As the size of the pulse $\Delta\tau$ increase from 0.1 ns to 1 ns it was verified that the time to first spike increase from about 1.5 ns to 5.5 ns (see **Fig. 7.4(c)**). However, at higher amplitudes $\Delta\iota$, the time to the first spike does not depend on the size of the pulses. To complement this analysis, we also show in **Fig. 7.4(d)** the time of the first spike for constant applied currents, corresponding to a pulse of infinite size. We notice that the time of the first pulse grows almost exponentially until a certain current where firings are no longer expected. Moreover, we notice that for high $\Delta\iota$, i.e. low currents, the time to the first spike becomes rather constant around 0.5 ns due to the existence of the refractory period. This spiking behavior, which does not require a resetting mechanism, is rather robust as a function of different parameters and the device properties can be tuned by designing the thickness of the free layer and of the tunnelling layer, which influence the temperature variations.

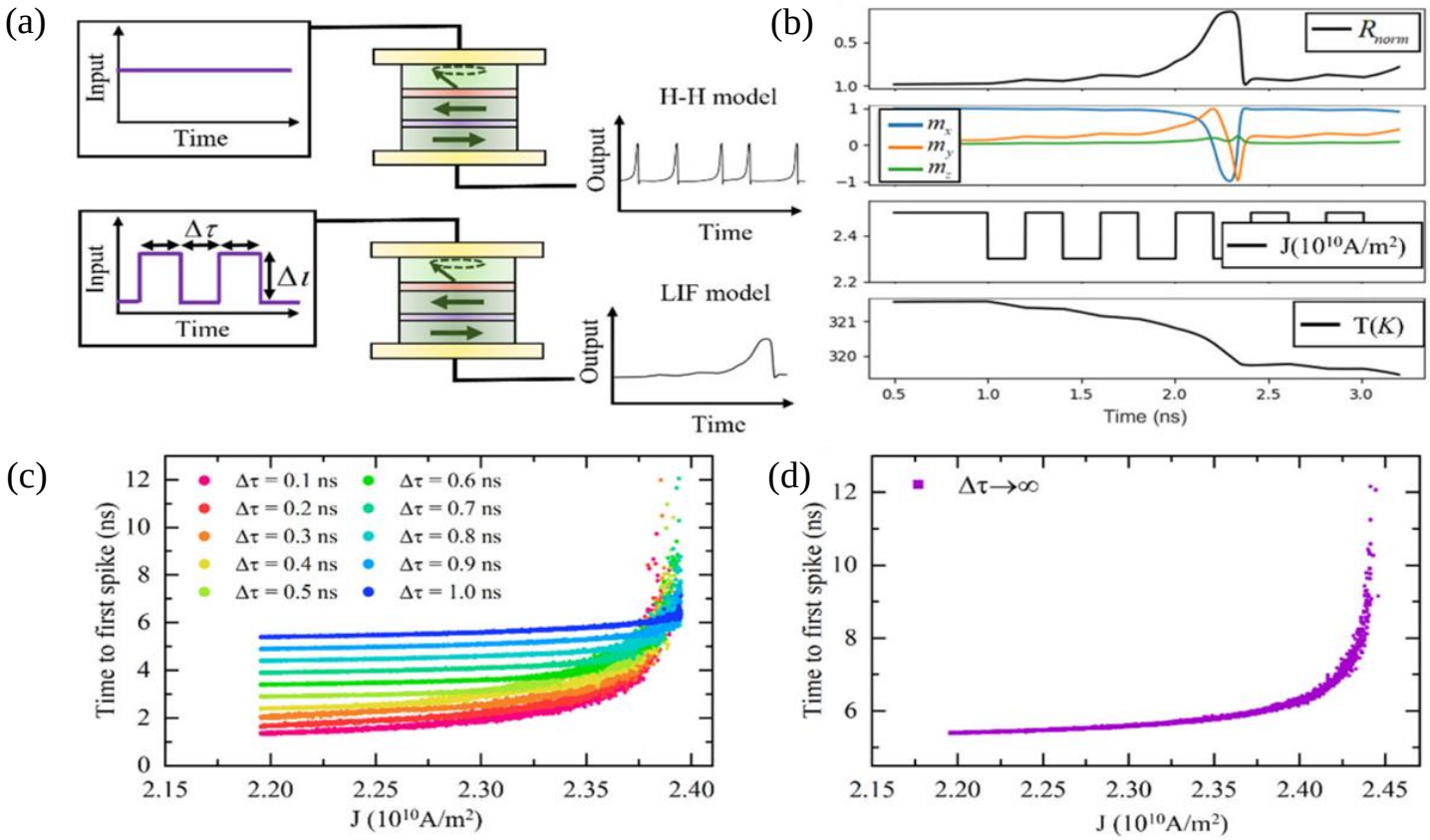

Figure 7.4 (a) Difference between the H-H model and the LIF model. In the LIF model, we consider pulses of amplitude Δι and period Δτ. (b) Evolution of the device properties under the presence of current pulses. From top to bottom panels, we show the normalized resistance, the evolution of the magnetization components, the profile of the applied current and the temperature of the device. (c) shows the time between the first pulse and the first synapse. Different colors represent different pulse sizes, while the x-axis represent the lowest current value in the pulse. To include thermal induced stochasticity, we simulated each pulse amplitude and size five times. (d) The time of the first synapse for a constant current.

7.4 Analogy between H-H & LLG Models

In the previous sections, we showed how the non-linear dynamics of the designed MTJ device combined with thermal effects can mimic the firing behavior of a Hodgkin-Huxley neuron.

Based on the summation of current over all ion channels given in **Eq. (6.7)** and on the activation functions of **Eq. (6.8)**, can be generalized into,

$$\frac{dx}{dt} = -\frac{1}{\tau_x}(x - x_0(V)) \qquad (7.7)$$

where *x* stands for m, l, and n (gating variables). Each ion channel in the H-H neuron is characterized by a different characteristic time, τ_x, the different timescales of which allow the model with four-time dependent channels to be reduced to only two. We emphasize that the H-H model is obtained phenomenologically to fit experimental data. The model described by **Eq. (6.7)** and **Eq. (7.7)** is highly nonlinear and cannot be easily simulated.

Our results confirm that the magnetization dynamics is equally complex and can emulate the H-H model to produce characteristic sharp spikes followed by the refractory period under constant input based on its own dynamics. We derive a minimal model based on the LLG **Eq. (2.20)** with some modifications to become,

$$\frac{d\mathbf{m}}{d\tau} = -\frac{\gamma}{1+\alpha^2}(\mathbf{m} \times (\mathbf{h}_{\text{eff}} + \mathbf{h}_{\mathbf{ther}}) + \alpha_G \mathbf{m} \times (\mathbf{m} \times \mathbf{h}_{\text{eff}})) - \tau_{\text{STT}} \mathbf{m} \times (\mathbf{m} \times \mathbf{p}) \qquad (7.8)$$

Where, the effective magnetization is given by **Eq. (7.6)** and τ_{STT} in a simplified form of **Eq. (2.21)**. The form of **Eq. (7.8)** constrains the rich magnetization dynamics to the specific device configuration and allows for a clear understanding of the model comparability. The minimal model is also useful for reducing the computational cost of numerical simulations.

We consider magnetization in spherical coordinates, $\mathrm{m} = \cos\theta\,(\hat{\mathrm{x}}\cos\phi + \hat{\mathrm{y}}\sin\phi) + \hat{\mathrm{z}}\sin\theta$, and by restricting it to the dynamics in the self-oscillation regime, with small variations of polar angle θ, we obtain the following equation of motion:

$$\frac{d\varphi}{dt} = -G + \iota, \quad (7.9)$$

Where,

$$G = \frac{\iota_0}{1-P(t)^2 cos\varphi} sin\varphi - \frac{\gamma\mu_0 M_S(T)}{2}\left(D_x + D_y - 2D_z + \left(D_x - D_y\right)cos2\varphi\right)\theta - \gamma H_F cos\varphi\theta \qquad (7.10)$$

Here, $\iota_0 = \gamma\,\hbar\,PJ_0/M_s ed$ and $\iota = \gamma\,\hbar PJ\,/M_s ed$ are, respectively, the reference spin current, which biases the magnetization towards **p**, and the spin-current difference, which allows for the firing behavior, as described in the previous section (Section 7.3). We neglect damping because in the active region the magnetic losses are compensated for by the negative damping originating from the spin-transfer-torque.

Moreover, notice that the model above emulates the H-H behavior, even in the absence of the dipolar field, i.e., $H_F = 0$. However, the field is necessary to set the tilted configuration of magnetization to achieve a low critical current for excitation of the self-oscillation of magnetization. The parameters $M_s(T)$ and $P(T)$ depend on temperature, as shown in **Eqs. (7.3-7.4)**. The model from **Eqs. (7.9-7.10)** based on the LLG reproduces the firing behavior reported in **Figs. 7.1(b)** & **7.2(a)** emulating the H-H model.

7.5 Variation of Current

To derive the minimal model from **Eqs. (7.9-7.10)**, we consider the LLG **Eq. (7.8)** and substitute the unitary magnetization in the spherical coordinates. Notably, for **m** parallel to the easy axis, $\theta = \pi/2$, while, for **m** along **p**, $\theta = \phi = 0$. We expand the LLG equation to linear order in θ, to consider auto-oscillations at high input currents. Thermal effects are included in the minimal model, **Eqs. (7.9-7.10)**, as effective changes to the material parameter values in the LLG **Eq. (7.8)**, shown in **Eqs. (7.2),(7.5)**. Moreover, in the main text, we neglect the contribution of fieldlike torques. We can include such torques by adding the following term to the LLG **Eq. (7.8)**:

$$\tau_{FL} = \alpha_{FL}\tau_{STT}\mathbf{m} \times (\mathbf{m} \times \mathbf{p}) \quad (7.11)$$

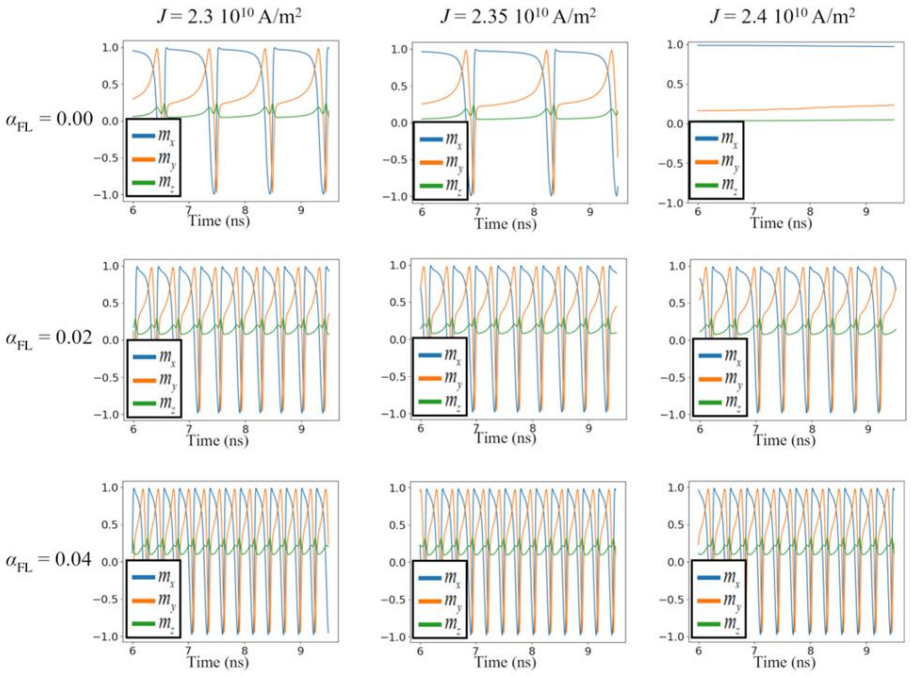

Figure 7.5 Behavior of magnetization dynamics for different currents and including the fieldlike torque. Material parameters are those given in **Table 7.2**.

where α_{FL} is a coefficient for the strength of the fieldlike torque and is often assumed to be small (i.e., $\alpha_{FL} << 1$). **Fig. 7.5** shows the spiking behavior for different currents and α_{FL}. We notice that the fieldlike torque qualitatively increases the frequency of the spikes, requiring a higher current for a lower spiking frequency.

7.6 Designing an Unsupervised SNN

To test the device concept in a simple SNN, we considered a rate-based information encoding (discussed in **Section 6.5.1**). We employed SNN to perform the classification of binarized images, where pixels can assume values "0" and "1". The SNN is given by two layers, an input and output layer, where the MTJs correspond to the firing neurons. For the current input of the first layer, we considered that "0" corresponds to a high current where spikes are not observed, and "1" corresponds to a lower current with a high frequency of spikes. The input current of output neurons I_{out} is given in terms of weighted voltage of the input neurons V_{in},

$$I_m(t) = \sum_{n=input} \chi_m(t) g(W_{mn} V_n(t)) \, , where \; \frac{dg(V)}{dt} = \rho_g \left(V - V_{ref}\right) + \frac{g(V) - g(V_{ref})}{\tau_g} \tag{7.12}$$

Here the function g(V) is an exponential function that allows to integrate spikes over time and maintain the input current for the output neurons rather constant, and the parameters ρ_g and τ_g were chosen according to the range of currents and frequency of spikes desired. The parameters $\chi_m(t)$ = {0.1,1} emulates the lateral inhibition, i.e., if an output neuron spikes the parameter $\chi_m(t)$is decreased for all other neurons for a period given by the characteristic time interval between two spikes of the input neurons.

Fig. 7.6(a), shows the behavior of a simple SNN with 4 firing neurons, two input and two output. For the learning process, we considered an unsupervised mechanism where the weights were updated according to the Hebbian and anti-Hebbian rule [259]. If an output neuron fired, the weight associated to the input neurons that had just spiked increase while the weight associated to the input neurons that haven't spiked recently decreased.

Furthermore, we let the SNN weights evolve until an output neuron has a considerably higher frequency compared to the other neurons. To strengthen the learning, after this process we fix the input currents of the output neurons according to the following algorithm: if the frequency of the output neuron is similar or higher than the frequency obtained with other input images for that same output neuron, the input current is set to the lowest value of the current achieved; else, if the frequency is significantly lower than the frequency obtained with other input images for that same output neuron, the neuron with second highest frequency is set with the lowest current achieved; the input of all other output neurons is fixed not to fire (i.e. the current associated to "0"). With these fixed input currents on inputs and output neurons, the weights then evolve normally according to the Hebbian and anti-Hebbian learning.

The SNN was tested on two different input sets of three patterns with 3 × 3 pixels as shown in **Fig. 7.6(b)**. The tested net shown in **Fig. 7.6(c)** is composed of nine input neurons, one for each pixel, and three output neurons. The pixels assumed values "0" or "1", which was uniquely identified to two different currents with different firing rates (0 – low frequency;1 – high frequency). The tests were performed by initiating the SNN with random weight matrices. After repeating in a temporal sequency each pattern from three to five times, the final weight matrix uniquely identified each of the input patterns, see **Fig. 7.6(d)** for an example.

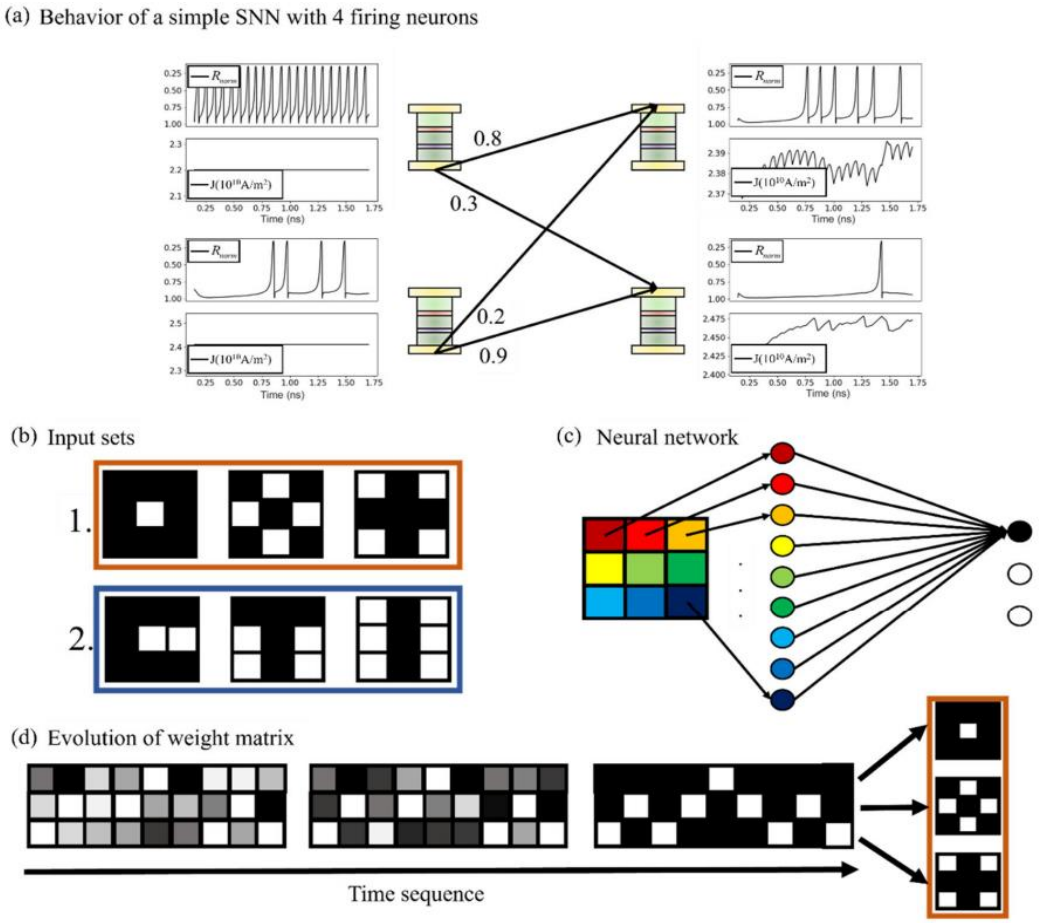

Figure 7.6 An example of SNN built with the proposed MTJ device. (a) Shows the behavior of an SNN with 4 neurons. The current of the two input neurons is set as constants. For each MTJ we show the behavior of the resistance (upper panel) and the input current (lower panel). The input currents of the output neurons are generated according to **Eq. 7.12**, with the respective weights W_{mn} shown. (b) shows the two sets considered for verifying the learning process and (c) shows a sketch of the Feed-forward All-connected SNN. Each pixel is associated with a single input neuron. (d) shows the evolution of the weight matrix. Starting from a random distribution of weights, after the training process, each figure can be represented by a single output neuron which has the highest frequency.

7.7 Summary

In this chapter we showed how the single MTJ device mimics the bio-realistic spiking neurons. Our device succeeded in emulating both the simpler LIF model as well as the more realistic H-H model without the need for a resetting mechanism. The proposed device works at room temperature and leverages two physics to produce constant firing at constant input. We demonstrate the frequency dependence on the applied current, as well as a firing

mechanism based on the amplitude and length of input pulses. The rate of spikes is in the range from MHz to GHz. The device presents several properties expected for the hardware implementation of bio-realistic neurons, which include: (i) highly scalable, reproducible, and robust; (ii) the characteristic refractory period, showing a depression of the potential after the spike; (ii) a small but non vanishing stochasticity, which allows for random fluctuations without significantly increasing the error rate.

We verified the behavior of the device by simulating a spiking neural network to recognize different figures. The information was encoded in the spiking ratio. The neural network was successfully able to classify the figures. The largest set we considered was 3x3 pixels, due to computational limitations. It is important to emphasize that while these calculations are usually computationally expensive, requiring a significant amount of memory and calculation time, the device's inherent nonlinear and time non-local dynamics can realize the calculation fast at low power input. Overall, the proposed device corresponds to a low-input, highly reproducible, scalable, robust, CMOS-compatible single MTJ working at room temperature, that emulates the bio-realistic H-H model. The device properties can be engineered to fit the network requirements by modifying the temperature gain/loss of a previously experimentally realized MTJ concept. This proposal allows for an easy drop-in replacement in current SNN CMOS-based hardware implementations to increase area, energy, and memory efficiency.

Chapter 8 Journal Articles

8.1 Published Articles

1. Davi Rohe Rodrigues, **Rayan Moukhader**, Yanxiang Lou, Bin Fang, Adrien Pontlevy, Abbas Hamadeh, Zhongming Zeng, Mario Carpentieri and Giovanni Finocchio

   "Spintronic Hodgkin-Huxley-Analogue Neuron Implemented with a Single Magnetic Tunnel Junction" in Physical Review Applied, vol 19, no. 6 (2023): 064010, doi:/10.1103/PhysRevApplied.19.064010

2. Davi Rohe Rodrigues, Eleonora Raimondo, Puliafito, **Rayan Moukhadder**, Bruno Azzerboni, Abbass Hamadeh, Philipp Pirro, Mario Carpentieri, and Giovanni Finocchio.

   "Dynamical neural network based on spin transfer nano-oscillators" in IEEE Transactions on Nanotechnology, vol 22 (2023), pp.800-805, doi: /10.1109/TNANO.2023.3330535

3. Abbas Hamadeh, Denys Slobodianiuk, **Rayan Moukhader**, Gennadiy Melkov, Vladyslav Borynskyi, Morteza Mohseni, Giovanni Finocchio, Vitaly Lomakin, Roman Verba , Grégoire de Loubens , Philipp Pirro , Olivier Klein .

   "Simultaneous multitone microwave emission by dc-driven spintronic nano-element".in Science Advances, vol 9, no 50 (2023) p.eadk1430, doi:/10.1126/sciadv.adk1430

8.2 Submitted Articles

4. **Rayan Moukhader**, Davi Rodrigues, Eleonora Raimondo, Vito Puliafito, Bruno Azzerboni, Mario Carpentieri, Abbass Hamadeh, Giovanni Finocchio, and Riccardo Tomasello.

   "Manipulation of magnetic solitons under the influence of DMI gradients".in IEEE Transactions on Nanotechnology is the journal, (2023) doi: /10.48550/arXiv.2305.15052

List of References

[1] Roy, Kaushik, Akhilesh Jaiswal, and Priyadarshini Panda. "Towards spike-based machine intelligence with neuromorphic computing." *Nature* 575.7784 (2019): 607-617.

[2] Merolla, Paul A., et al. "A million spiking-neuron integrated circuit with a scalable communication network and interface." *Science* 345.6197 (2014): 668-673.

[3] Davies, Mike, et al. "Loihi: A neuromorphic manycore processor with on-chip learning." *Ieee Micro* 38.1 (2018): 82-99.

[4] Marković, Danijela, et al. "Physics for neuromorphic computing." *Nature Reviews Physics* 2.9 (2020): 499-510.

[5] Yang, Jia-Qin, et al. "Leaky integrate-and-fire neurons based on perovskite memristor for spiking neural networks." *Nano Energy* 74 (2020): 104828.

[6] Natarajan, Aishwarya, and Jennifer Hasler. "Hodgkin–huxley neuron and fpaa dynamics." *IEEE transactions on biomedical circuits and systems* 12.4 (2018): 918-926.

[7] Afifi, Ahmad, Ahmad Ayatollahi, and Farshid Raissi. "Implementation of biologically plausible spiking neural network models on the memristor crossbar-based CMOS/nano circuits." *2009 European Conference on Circuit Theory and Design*. IEEE, 2009.

[8] Querlioz, Damien, et al. "Bioinspired networks with nanoscale memristive devices that combine the unsupervised and supervised learning approaches." Proceedings of the 2012 IEEE/ACM International Symposium on Nanoscale Architectures. 2012.

[9] Chua, Leon. "Memristor, Hodgkin–Huxley, and edge of chaos." Nanotechnology 24.38 (2013): 383001.

[10] Sengupta, Abhronil, et al. "Magnetic tunnel junction mimics stochastic cortical spiking neurons." Scientific reports 6.1 (2016): 30039.

[11] Tuma, Tomas, et al. "Stochastic phase-change neurons." Nature nanotechnology 11.8 (2016): 693-699.

[12] Sengupta, Abhronil, Aparajita Banerjee, and Kaushik Roy. "Hybrid spintronic-CMOS spiking neural network with on-chip learning: Devices, circuits, and systems." Physical Review Applied 6.6 (2016): 064003.

[13] Sengupta, Abhronil, et al. "Spin-orbit torque induced spike-timing dependent plasticity." Applied Physics Letters 106.9 (2015).

[14] Suri, Manan, et al. "Phase change memory as synapse for ultra-dense neuromorphic systems: Application to complex visual pattern extraction." 2011 International Electron Devices Meeting. IEEE, 2011.

[15] Jo, Sung Hyun, et al. "Nanoscale memristor device as synapse in neuromorphic systems." Nano letters 10.4 (2010): 1297-1301.

[16] Tomasello, Riccardo, et al. "A strategy for the design of skyrmion racetrack memories." Scientific reports 4.1 (2014): 1-7.

[17] Geng, Liwei D., and Yongmei M. Jin. "Magnetic vortex racetrack memory." Journal of Magnetism and Magnetic Materials 423 (2017): 84-89.
[18] Parkin, Stuart SP, Masamitsu Hayashi, and Luc Thomas. "Magnetic domain-wall racetrack memory." Science 320.5873 (2008): 190-194.
[19] Song, Kyung Mee, et al. "Skyrmion-based artificial synapses for neuromorphic computing." Nature Electronics 3.3 (2020): 148-155.
[20] Yokouchi, Tomoyuki, et al. "Pattern recognition with neuromorphic computing using magnetic field–induced dynamics of skyrmions." Science Advances 8.39 (2022): eabq5652.
[21] Yun, Chao, et al. "Magnetic anisotropy-controlled vortex nano-oscillator for neuromorphic computing." Frontiers in Physics 10 (2022): 1019881.
[22] Sengupta, Abhronil, and Kaushik Roy. "Short-term plasticity and long-term potentiation in magnetic tunnel junctions: Towards volatile synapses." Physical Review Applied 5.2 (2016): 024012.
[23] Grollier, Julie, Damien Querlioz, and Mark D. Stiles. "Spintronic nanodevices for bioinspired computing." Proceedings of the IEEE 104.10 (2016): 2024-2039.
[24] Bertotti, Giorgio. Hysteresis in magnetism: for physicists, materials scientists, and engineers. Gulf Professional Publishing, 1998.
[25] Hillebrands, Burkard, and Kamel Ounadjela, eds. Spin dynamics in confined magnetic structures I. Vol. 83. Springer Science & Business Media, 2003.
[26] Thiaville, André, and Yoshinobu Nakatani. "Domain-wall dynamics in nanowiresand nanostrips." Spin dynamics in confined magnetic structures III (2006): 161-205.
[27] Varonov, ALBERT MAKSIMOV. "The Theory of Heating of the Solar Corona and Launching of the Solar Wind by Alfven Waves." arXiv preprint arXiv:1903.07688 (2019).
[28] Scholz, Erhard. "Introducing groups into quantum theory (1926–1930)." Historia mathematica 33.4 (2006): 440-490.
[29] Brown Jr, William Fuller. "Micromagnetics, domains, and resonance." Journal of Applied Physics 30.4 (1959): S62-S69.
[30] Jackson, John David. "Classical electrodynamics." (1999): 841-842.
[31] Landau, L. A. L. E., and Evgeny Lifshitz. "On the theory of the dispersion of magnetic permeability in ferromagnetic bodies." Perspectives in Theoretical Physics. Pergamon, 1992. 51-65.
[32] Gilbert, Thomas L. "A Lagrangian formulation of the gyromagnetic equation of the magnetization field." Phys. Rev. 100 (1955): 1243.
[33] Gilbert, Thomas L. "A phenomenological theory of damping in ferromagnetic materials." IEEE transactions on magnetics 40.6 (2004): 3443-3449.
[34] Landé, Alfred. "Über den anomalen zeemaneffekt (teil i)." Zeitschrift für Physik 5.4 (1921): 231-241.
[35] Slonczewski, John C. "Current-driven excitation of magnetic multilayers." Journal of Magnetism and Magnetic Materials 159.1-2 (1996): L1-L7.
[36] Berger, Luc. "Emission of spin waves by a magnetic multilayer traversed by a current." Physical Review B 54.13 (1996): 9353.

[37] Ralph, Daniel C., and Mark D. Stiles. "Spin transfer torques." Journal of Magnetism and Magnetic Materials 320.7 (2008): 1190-1216.
[38] Slonczewski, John C. "Currents, torques, and polarization factors in magnetic tunnel junctions." *Physical Review* B 71.2 (2005): 024411.
[39] Slavin, Andrei, and Vasil Tiberkevich. "Nonlinear auto-oscillator theory of microwave generation by spin-polarized current." *IEEE Transactions on Magnetics* 45.4 (2009): 1875-1918.
[40] Zhang, Sh, and Z. Li. "Roles of nonequilibrium conduction electrons on the magnetization dynamics of ferromagnets." *Physical review letters* 93.12 (2004): 127204.
[41] Xue, Fen, et al. "Large voltage control of magnetic anisotropy in CoFeB/MgO/OX structures at room temperature." *APL Materials* 7.10 (2019).
[42] Wen, Zhenchao, et al. "Voltage control of magnetic anisotropy in epitaxial Ru/Co2FeAl/MgO heterostructures." *Scientific reports* 7.1 (2017): 45026.
[43] Shao, Yixin, et al. "Sub-volt switching of nanoscale voltage-controlled perpendicular magnetic tunnel junctions." *Communications Materials* 3.1 (2022): 87.
[44] Shukla, Amit Kumar, et al. "Voltage-Controlled Magnetic Anisotropy in Fe1− x Co x/Pd/MgO system." *Scientific Reports* 8.1 (2018): 10362.
[45] Zhao, Weisheng, and Guillaume Prenat, eds. *Spintronics-based computing*. Berlin, Germany:: Springer, 2015.
[46] Go, Dongwook, et al. "Orbitronics: Orbital currents in solids." *Europhysics Letters* 135.3 (2021): 37001.
[47] Trier, Felix, et al. "Oxide spin-orbitronics: spin–charge interconversion and topological spin textures." *Nature Reviews Materials* 7.4 (2022): 258-274.
[48] Zhang, Wei, and Kannan M. Krishnan. "Epitaxial exchange-bias systems: From fundamentals to future spin-orbitronics." *Materials Science and Engineering: R: Reports* 105 (2016): 1-20.
[49] Hankiewicz, Ewelina, Giovanni Vignale, and Michael Flatté. "What is intrinsic and what is extrinsic in the spin Hall effect?" *APS March Meeting Abstracts*. 2006.
[50] Dyakonov, Mikhail I. "Possibility of orienting electron spins with current." *JETP Lett. USSR* 13 (1971): 467.
[51] Dyakonov, Mikhail I., and V. I. Perel. "Current-induced spin orientation of electrons in semiconductors." *Physics Letters* A 35.6 (1971): 459-460.
[52] Gieniusz, R., et al. "Dzyaloshinskii-Moriya interaction and magnetic anisotropy in Pt/Co/Au trilayers modified by Ga+ ion irradiation." *Journal of Magnetism and Magnetic Materials* 537 (2021): 168160.
[53] Fert, Albert, Vincent Cros, and Joao Sampaio. "Skyrmions on the track." *Nature nanotechnology* 8.3 (2013): 152-156.
[54] Rohart, S., and A. Thiaville. "Skyrmion confinement in ultrathin film nanostructures in the presence of Dzyaloshinskii-Moriya interaction." *Physical Review B* 88.18 (2013): 184422.
[55] Abert, Claas. "Micromagnetics and spintronics: models and numerical methods." *The European Physical Journal* B 92 (2019): 1-45.

[56] Miltat, Jacques E., and Michael J. Donahue. "Numerical micromagnetics: Finite difference methods." *Handbook of magnetism and advanced magnetic materials* 2 (2007): 742-764.
[57] Fidler, Josef, and Thomas Schrefl. "Micromagnetic modelling-the current state of the art." *Journal of Physics D: Applied Physics* 33.15 (2000): R135.
[58] Berkov, D. V., K. Ramstöcck, and A. Hubert. "Solving micromagnetic problems. Towards an optimal numerical method." *physica status solidi* (a) 137.1 (1993): 207-225.
[59] Donahue, Michael Joseph, and Donald G. Porter. "OOMMF user's guide, version 1.0." (1999).
[60] D. V. Berkov and N. L. Gorn, [http://www.micromagus.de].
[61] Leliaert, Jonathan, et al. "Fast micromagnetic simulations on gpu—recent advances made with." *Journal of Physics D: Applied Physics* 51.12 (2018): 123002.
[62] Vansteenkiste, Arne, et al. "The design and verification of MuMax3." *AIP advances* 4.10 (2014).
[63] Anon μMAG Standard Problem #4 results.
[64] Giordano, Anna, et al. "Semi-implicit integration scheme for Landau–Lifshitz–Gilbert-Slonczewski equation." *Journal of Applied Physics* 111.7 (2012).
[65] Tomasello, R., M. Carpentieri, and Giovanni Finocchio. "Influence of the Dzyaloshinskii-Moriya interaction on the spin-torque diode effect." *Journal of Applied Physics* 115.17 (2014): 17C730.
[66] Zahed, I., and G. E. Brown. "The Skyrme Model." *Selected Papers, With Commentary, Of Tony Hilton Royle Skyrme*. 1994. 338-438.
[67] Bogdanov, A., and A. Hubert. "Thermodynamically stable magnetic vortex states in magnetic crystals." *Journal of magnetism and magnetic materials* 138.3 (1994): 255-269.
[68] Hrabec, Aleš, et al. "Synthetic chiral magnets promoted by the Dzyaloshinskii–Moriya interaction." *Applied Physics Letters* 117.13 (2020).
[69] Neubauer, A., et al. "Topological Hall effect in the A phase of MnSi." *Physical review letters* 102.18 (2009): 186602.
[70] Yu, X. Z., et al. "Real-space observation of a two-dimensional skyrmion crystal." *Nature* 465.7300 (2010): 901-904.
[71] Huang, S. X., and C. L. Chien. "Extended skyrmion phase in epitaxial FeGe (111) thin films." *Physical review letters* 108.26 (2012): 267201.
[72] Ritz, R., et al. "Giant generic topological Hall resistivity of MnSi under pressure." *Physical Review B* 87.13 (2013): 134424.
[73] Chacon, A., et al. "Uniaxial pressure dependence of magnetic order in MnSi." *Physical review letters* 115.26 (2015): 267202.
[74] Yokouchi, Tomoyuki, et al. "Formation of in-plane skyrmions in epitaxial MnSi thin films as revealed by planar Hall effect." *journal of the physical society of japan* 84.10 (2015): 104708.
[75] Yu, Xiuzhen, et al. "Variation of skyrmion forms and their stability in MnSi thin plates." *Physical Review B* 91.5 (2015): 054411.

[76] Yamasaki, Y., et al. "Dynamical process of skyrmion-helical magnetic transformation of the chiral-lattice magnet FeGe probed by small-angle resonant soft x-ray scattering." *Physical Review B* 92.22 (2015): 220421.
[77] Ahmed, Adam S., et al. "Chiral bobbers and skyrmions in epitaxial FeGe/Si (111) films." *Physical Review Materials* 2.4 (2018): 041401.
[78] Zheng, Fengshan, et al. "Experimental observation of chiral magnetic bobbers in B20-type FeGe." *Nature nanotechnology* 13.6 (2018): 451-455.
[79] Kanazawa, N., et al. "Possible skyrmion-lattice ground state in the B 20 chiral-lattice magnet MnGe as seen via small-angle neutron scattering." *Physical Review B* 86.13 (2012): 134425.
[80] Fujishiro, Yukako, et al. "Large magneto-thermopower in MnGe with topological spin texture." *Nature communications* 9.1 (2018): 408.
[81] Milde, Peter, et al. "Surface pinning and triggered unwinding of skyrmions in a cubic chiral magnet." *Physical Review B* 100.2 (2019): 024408.
[82] Adams, T., et al. "Skyrmion lattice domains in Fe1− xCoxSi." Journal of Physics: Conference Series. Vol. 200. No. 3. *IOP Publishing*, 2010.
[83] Balasubramanian, Balamurugan, et al. "Chiral magnetism and high-temperature skyrmions in B20-ordered Co-Si." *Physical Review Letters* 124.5 (2020): 057201.
[84] Franz, C., et al. "Real-space and reciprocal-space Berry phases in the Hall effect of Mn 1− x Fe x Si." *Physical review letters* 112.18 (2014): 186601.
[85] Yokouchi, T., et al. "Stability of two-dimensional skyrmions in thin films of Mn 1− x Fe x Si investigated by the topological Hall effect." *Physical Review B* 89.6 (2014): 064416.
[86] Tokunaga, Y., et al. "A new class of chiral materials hosting magnetic skyrmions beyond room temperature." *Nature communications* 6.1 (2015): 7638.
[87] Leonov, A. O., and István Kézsmárki. "Asymmetric isolated skyrmions in polar magnets with easy-plane anisotropy." *Physical Review B* 96.1 (2017): 014423.
[88] Moreau-Luchaire, Constance, et al. "Additive interfacial chiral interaction in multilayers for stabilization of small individual skyrmions at room temperature." *Nature nanotechnology* 11.5 (2016): 444-448.
[89] Soumyanarayanan, Anjan, et al. "Tunable room-temperature magnetic skyrmions in Ir/Fe/Co/Pt multilayers." *Nature materials* 16.9 (2017): 898-904.
[90] Heinze, Stefan, et al. "Spontaneous atomic-scale magnetic skyrmion lattice in two dimensions." *nature physics* 7.9 (2011): 713-718.
[91] Jiang, Wanjun, et al. "Blowing magnetic skyrmion bubbles." *Science* 349.6245 (2015): 283-286.
[92] Boulle, Olivier, et al. "Room-temperature chiral magnetic skyrmions in ultrathin magnetic nanostructures." *Nature nanotechnology* 11.5 (2016): 449-454.
[93] Soumyanarayanan, Anjan, et al. "Emergent phenomena induced by spin–orbit coupling at surfaces and interfaces." *Nature* 539.7630 (2016): 509-517.
[94] Quessab, Yassine, et al. "Zero-field nucleation and fast motion of skyrmions induced by nanosecond current pulses in a ferrimagnetic thin film." *Nano Letters* 22.15 (2022): 6091-6097.

[95] Woo, Seonghoon, et al. "Current-driven dynamics and inhibition of the skyrmion Hall effect of ferrimagnetic skyrmions in GdFeCo films." *Nature communications* 9.1 (2018): 959.
[96] Mandru, Andrada-Oana, et al. "Coexistence of distinct skyrmion phases observed in hybrid ferromagnetic/ferrimagnetic multilayers." *Nature communications* 11.1 (2020): 6365.
[97] Yıldırım, Oğuz, et al. "Tuning the Coexistence Regime of Incomplete and Tubular Skyrmions in Ferromagnetic/Ferrimagnetic/Ferromagnetic Trilayers." *ACS Applied Materials & Interfaces* 14.29 (2022): 34002-34010.
[98] Dohi, Takaaki, et al. "Formation and current-induced motion of synthetic antiferromagnetic skyrmion bubbles." *Nature communications* 10.1 (2019): 5153.
[99] Legrand, William, et al. "Room-temperature stabilization of antiferromagnetic skyrmions in synthetic antiferromagnets." *Nature materials* 19.1 (2020): 34-42.
[100] Juge, Roméo, et al. "Skyrmions in synthetic antiferromagnets and their nucleation via electrical current and ultra-fast laser illumination." *Nature Communications* 13.1 (2022): 4807.
[101] Gupta, Ankur, Tamilselvan Sakthivel, and Sudipta Seal. "Recent development in 2D materials beyond graphene." *Progress in Materials Science* 73 (2015): 44-126.
[102] Huang, Bevin, et al. "Electrical control of 2D magnetism in bilayer CrI 3." *Nature nanotechnology* 13.7 (2018): 544-548.
[103] Ding, Bei, et al. "Observation of magnetic skyrmion bubbles in a van der Waals ferromagnet Fe3GeTe2." *Nano letters* 20.2 (2019): 868-873.
[104] Bonilla, Manuel, et al. "Strong room-temperature ferromagnetism in VSe2 monolayers on van der Waals substrates." *Nature nanotechnology* 13.4 (2018): 289-293.
[105] Liu, Jie, et al. "Analysis of electrical-field-dependent Dzyaloshinskii-Moriya interaction and magnetocrystalline anisotropy in a two-dimensional ferromagnetic monolayer." *Physical Review B* 97.5 (2018): 054416.
[106] Liang, Jinghua, Qirui Cui, and Hongxin Yang. "Electrically switchable Rashba-type Dzyaloshinskii-Moriya interaction and skyrmion in two-dimensional magnetoelectric multiferroics." *Physical Review B* 102.22 (2020): 220409.
[107] Shen, Zhong, et al. "Strain-tunable Dzyaloshinskii-Moriya interaction and skyrmions in two-dimensional Janus Cr 2 X 3 Y 3 (X, Y= Cl, Br, I, X≠ Y) trihalide monolayers." *Physical Review B* 106.9 (2022): 094403.
[108] Zhou, Y., et al. "Dynamically stabilized magnetic skyrmions." *Nature communications* 6.1 (2015): 8193.
[109] Carpentieri, Mario, et al. "Topological, non-topological and instanton droplets driven by spin-transfer torque in materials with perpendicular magnetic anisotropy and Dzyaloshinskii–Moriya Interaction." *Scientific Reports* 5.1 (2015): 16184.
[110] Zhang, Senfu, et al. "Current-induced magnetic skyrmions oscillator." *New Journal of Physics* 17.2 (2015): 023061.
[111] Garcia-Sanchez, F., et al. "A skyrmion-based spin-torque nano-oscillator." *New Journal of Physics* 18.7 (2016): 075011.

[112] Finocchio, G., et al. "Skyrmion based microwave detectors and harvesting." *Applied Physics Letters* 107.26 (2015).
[113] Medlej, Israa, Abbass Hamadeh, and Fouad El Haj Hassan. "Skyrmion based random bit generator." *Physica B: Condensed Matter* 579 (2020): 411900.
[114] Luo, Shijiang, et al. "Reconfigurable skyrmion logic gates." *Nano letters* 18.2 (2018): 1180-1184.
[115] Pinna, Daniele, et al. "Skyrmion gas manipulation for probabilistic computing." *Physical Review Applied* 9.6 (2018): 064018.
[116] Raab, Klaus, et al. "Brownian reservoir computing realized using geometrically confined skyrmion dynamics." *Nature Communications* 13.1 (2022): 6982.
[117] Song, Kyung Mee, et al. "Skyrmion-based artificial synapses for neuromorphic computing." *Nature Electronics* 3.3 (2020): 148-155.
[118] Moutafis, C., S. Komineas, and J. A. C. Bland. "Dynamics and switching processes for magnetic bubbles in nanoelements." *Physical Review B* 79.22 (2009): 224429.
[119] Braun, Hans-Benjamin. "Topological effects in nanomagnetism: from superparamagnetism to chiral quantum solitons." *Advances in Physics* 61.1 (2012): 1-116.
[120] Romming, Niklas, et al. "Field-dependent size and shape of single magnetic skyrmions." *Physical review letters* 114.17 (2015): 177203.
[121] Zhang, Xichao, et al. "Skyrmion-electronics: writing, deleting, reading and processing magnetic skyrmions toward spintronic applications." *Journal of Physics: Condensed Matter* 32.14 (2020): 143001.
[122] Woo, Seonghoon, et al. "Observation of room-temperature magnetic skyrmions and their current-driven dynamics in ultrathin metallic ferromagnets." *Nature materials* 15.5 (2016): 501-506.
[123] Casiraghi, Arianna, et al. "Individual skyrmion manipulation by local magnetic field gradients." *Communications Physics* 2.1 (2019): 145.
[124] Zhang, S. L., et al. "Manipulation of skyrmion motion by magnetic field gradients." *Nature communications* 9.1 (2018): 2115.
[125] Raimondo, Eleonora, et al. "Temperature-gradient-driven magnetic skyrmion motion." *Physical Review Applied* 18.2 (2022): 024062.
[126] Kong, Lingyao, and Jiadong Zang. "Dynamics of an insulating skyrmion under a temperature gradient." *Physical review letters* 111.6 (2013): 067203.
[127] Wang, Zidong, et al. "Thermal generation, manipulation and thermoelectric detection of skyrmions." *Nature Electronics* 3.11 (2020): 672-679.
[128] Siracusano, Giulio, et al. "Magnetic radial vortex stabilization and efficient manipulation driven by the Dzyaloshinskii-Moriya interaction and spin-transfer torque." *Physical Review Letters* 117.8 (2016): 087204.
[129] McGuire, Michael A., et al. "Coupling of crystal structure and magnetism in the layered, ferromagnetic insulator CrI3." *Chemistry of Materials* 27.2 (2015): 612-620.
[130] Jiang, Shengwei, Jie Shan, and Kin Fai Mak. "Electric-field switching of two-dimensional van der Waals magnets." *Nature materials* 17.5 (2018): 406-410.

[131] Xu, Yang, et al. "Coexisting ferromagnetic–antiferromagnetic state in twisted bilayer CrI3." *Nature Nanotechnology* 17.2 (2022): 143-147.
[132] Tomasello, R., et al. "Performance of synthetic antiferromagnetic racetrack memory: domain wall versus skyrmion." *Journal of Physics D: Applied Physics* 50.32 (2017): 325302.
[133] Thiele, A. A. "Steady-state motion of magnetic domains." *Physical Review Letters* 30.6 (1973): 230.
[134] Clarke, D. J., et al. "Dynamics of a vortex domain wall in a magnetic nanostrip: Application of the collective-coordinate approach." *Physical Review B* 78.13 (2008): 134412.
[135] Gorshkov, Ilya O., et al. "DMI-gradient-driven skyrmion motion." *ACS Applied Electronic Materials* 4.7 (2022): 3205-3211.
[136] Tomasello, Riccardo, et al. "Chiral skyrmions in an anisotropy gradient." *Physical Review B* 98.2 (2018): 024421.
[137] Ladak, Sam, Amalio Fernández-Pacheco, and Peter Fischer. "Science and technology of 3D magnetic nanostructures." *APL Materials* 10.12 (2022).
[138] Rybakov, Filipp N., et al. "Magnetic hopfions in solids." *APL materials* 10.11 (2022).
[139] Faddeev, L. D. "Some comments on the many-dimensional solitons." *Letters in Mathematical Physics* 1 (1976): 289-293.
[140] Skyrme, Tony Hilton Royle. "A non-linear field theory." *Proceedings of the Royal Society of London. Series A. Mathematical and Physical Sciences* 260.1300 (1961): 127-138.
[141] Kent, Noah, et al. "Creation and observation of Hopfions in magnetic multilayer systems." *Nature communications* 12.1 (2021): 1562.
[142] Sugic, Danica, et al. "Particle-like topologies in light." *Nature communications* 12.1 (2021): 6785.
[143] Voinescu, Robert, Jung-Shen B. Tai, and Ivan I. Smalyukh. "Hopf solitons in helical and conical backgrounds of chiral magnetic solids." *Physical Review Letters* 125.5 (2020): 057201.
[144] Sutcliffe, Paul. "Hopfions in chiral magnets." *Journal of Physics A: Mathematical and Theoretical* 51.37 (2018): 375401.
[145] Liu, Yizhou, Roger K. Lake, and Jiadong Zang. "Binding a hopfion in a chiral magnet nanodisk." *Physical Review B* 98.17 (2018): 174437.
[146] Ackerman, Paul J., and Ivan I. Smalyukh. "Static three-dimensional topological solitons in fluid chiral ferromagnets and colloids." *Nature materials* 16.4 (2017): 426-432.
[147] Tai, Jung-Shen B., and Ivan I. Smalyukh. "Static Hopf solitons and knotted emergent fields in solid-state noncentrosymmetric magnetic nanostructures." *Physical Review Letters* 121.18 (2018): 187201.
[148] Wang, X. S., Alireza Qaiumzadeh, and Arne Brataas. "Current-driven dynamics of magnetic hopfions." *Physical review letters* 123.14 (2019): 147203.
[149] Raftrey, David, and Peter Fischer. "Field-driven dynamics of magnetic hopfions." *Physical review letters* 127.25 (2021): 257201.

[150] Zhang, Sh, and Z. Li. "Roles of nonequilibrium conduction electrons on the magnetization dynamics of ferromagnets." *Physical review letters* 93.12 (2004): 127204.
[151] Zagorodny, Juan Pablo. *Dynamics of vortices in the two-dimensional anisotropic Heisenberg model with magnetic fields*. Diss. 2003.
[152] Donnay, G., et al. "Symmetry of magnetic structures: magnetic structure of chalcopyrite." *Physical Review* 112.6 (1958): 1917.
[153] Karakas, Vedat, et al. "Observation of magnetic radial vortex nucleation in a multilayer stack with tunable anisotropy." *Scientific Reports* 8.1 (2018): 7180.
[154] Wachowiak, A., et al. "Direct observation of internal spin structure of magnetic vortex cores." *science* 298.5593 (2002): 577-580.
[155] Shinjo, T., et al. "Magnetic vortex core observation in circular dots of permalloy." *science* 289.5481 (2000): 930-932.
[156] Zuo, Shulan, et al. "In situ observation of magnetic vortex manipulation by external fields in amorphous CeFeB ribbon." *Acta Materialia* 140 (2017): 465-471.
[157] Nakano, K., et al. "All-electrical operation of magnetic vortex core memory cell." *Applied Physics Letters* 99.26 (2011).
[158] Jenkins, A. S., et al. "Spin-torque resonant expulsion of the vortex core for an efficient radiofrequency detection scheme." *Nature nanotechnology* 11.4 (2016): 360-364.
[159] Leulmi, Selma, et al. "Triggering the apoptosis of targeted human renal cancer cells by the vibration of anisotropic magnetic particles attached to the cell membrane." *Nanoscale* 7.38 (2015): 15904-15914.
[160] Peixoto, L., et al. "Magnetic nanostructures for emerging biomedical applications." *Applied Physics Reviews* 7.1 (2020).
[161] Yun, Chao, et al. "Magnetic anisotropy-controlled vortex nano-oscillator for neuromorphic computing." Frontiers in Physics 10 (2022): 1019881.
[162] Tretiakov, O. A., and O. Tchernyshyov. "Vortices in thin ferromagnetic films and the skyrmion number." *Physical Review* B 75.1 (2007): 012408.
[163] Skirdkov, Petr N., and Konstatin A. Zvezdin. "Spin-Torque Diodes: From Fundamental Research to Applications." *Annalen der Physik* 532.6 (2020): 1900460.
[164] Finocchio, Giovanni, et al. "Perspectives on spintronic diodes." *Applied Physics Letters* 118.16 (2021).
[165] Kong, Lingyao, and Jiadong Zang. "Dynamics of an insulating skyrmion under a temperature gradient." *Physical review letters* 111.6 (2013): 067203.
[166] Tacchi, Silvia, et al. "Interfacial Dzyaloshinskii-Moriya interaction in Pt/CoFeB films: effect of the heavy-metal thickness." *Physical review letters* 118.14 (2017): 147201.
[167] Gusev, Sadonikov, et al. "Manipulation of the Dzyaloshinskii–Moriya interaction in Co/Pt multilayers with strain." *Physical review letters* 124.15 (2020): 157202.

[168] Lungu, Anita, et al. "Dynamic power gating with quality guarantees." *Proceedings of the 2009 ACM/IEEE international symposium on Low power electronics and design*. 2009.
[169] Yakout, Saad Mabrouk. "Spintronics: future technology for new data storage and communication devices." *Journal of superconductivity and novel magnetism* 33.9 (2020): 2557-2580.
[170] Chang, Chun-Yen. "The highlights in the nano world." *Proceedings of the IEEE* 91.11 (2003): 1756-1764.
[171] Johnson, Mark, and Robert H. Silsbee. "Interfacial charge-spin coupling: Injection and detection of spin magnetization in metals." *Physical review letters* 55.17 (1985): 1790.
[172] Baibich, Mario Norberto, et al. "Giant magnetoresistance of (001) Fe/(001) Cr magnetic superlattices." *Physical review letters* 61.21 (1988): 2472.
[173] Binasch, Grünberg, et al. "Enhanced magnetoresistance in layered magnetic structures with antiferromagnetic interlayer exchange." *Physical review B* 39.7 (1989): 4828.
[174] Dieny, Bernard, et al. "Opportunities and challenges for spintronics in the microelectronics industry." *Nature Electronics* 3.8 (2020): 446-459.
[175] Puebla, Jorge, et al. "Spintronic devices for energy-efficient data storage and energy harvesting." *Communications Materials* 1.1 (2020): 24.
[176] Vedmedenko, Elena Yu, et al. "The 2020 magnetism roadmap." Journal of Physics D: Applied Physics 53.45 (2020): 453001.
[177] Joshi, Vinod Kumar, et al. "From MTJ device to hybrid CMOS/MTJ circuits: A review." *IEEE Access* 8 (2020): 194105-194146.
[178] Khymyn, Roman, et al. "Ultra-fast artificial neuron: generation of picosecond-duration spikes in a current-driven antiferromagnetic auto-oscillator." *Scientific reports* 8.1 (2018): 15727.
[179] Kurenkov, Aleksandr, et al. "Artificial neuron and synapse realized in an antiferromagnet/ferromagnet heterostructure using dynamics of spin–orbit torque switching." Advanced Materials 31.23 (2019): 1900636.
[180] Vincent, Adrien F., et al. "Spin-transfer torque magnetic memory as a stochastic memristive synapse for neuromorphic systems." *IEEE transactions on biomedical circuits and systems* 9.2 (2015): 166-174.
[181] Peng, S. Z., et al. "Magnetic tunnel junctions for spintronics: Principles and applications." *Wiley Encyclopedia of Electrical and Electronics Engineering* (1999): 1-16.
[182] Huai, Yiming. "Spin-transfer torque MRAM (STT-MRAM): Challenges and prospects." *AAPPS bulletin* 18.6 (2008): 33-40.
[183] Julliere, Michel. "Tunneling between ferromagnetic films." *Physics letters A* 54.3 (1975): 225-226.
[184] Butler, W. H., et al. "Spin-dependent tunneling conductance of Fe| MgO| Fe sandwiches." *Physical Review B* 63.5 (2001): 054416.
[185] Mathon, J., and A. Umerski. "Theory of tunneling magnetoresistance of an epitaxial Fe/MgO/Fe (001) junction." *Physical Review B* 63.22 (2001): 220403.

[186] Gallagher, William J., and Stuart SP Parkin. "Development of the magnetic tunnel junction MRAM at IBM: From first junctions to a 16-Mb MRAM demonstrator chip." *IBM Journal of Research and Development* 50.1 (2006): 5-23.
[187] Wolf, S. A., et al. "Spintronics: a spin-based electronics vision for the future." *science* 294.5546 (2001): 1488-1495.
[188] Wang, Zhaohao. "Compact modeling and circuit design based on ferroelectric tunnel junction and spin-Hall-assisted spin-transfer torque." (2015).
[189] El Baraji, M., et al. "Dynamic compact model of thermally assisted switching magnetic tunnel junctions." *Journal of Applied Physics* 106.12 (2009).
[190] Faber, Louis-Barthelemy, et al. "Dynamic compact model of spin-transfer torque based magnetic tunnel junction (MTJ)." *2009 4th International Conference on Design & Technology of Integrated Systems in Nanoscal Era.* IEEE, 2009.
[191] Chen, E., et al. "Advances and future prospects of spin-transfer torque random access memory." *IEEE Transactions on Magnetics* 46.6 (2010): 1873-1878.
[192] Liu, Luqiao, et al. "Current-induced switching of perpendicularly magnetized magnetic layers using spin torque from the spin Hall effect." *Physical review letters* 109.9 (2012): 096602.
[193] Alzate, Juan G., et al. "Temperature dependence of the voltage-controlled perpendicular anisotropy in nanoscale MgO| CoFeB| Ta magnetic tunnel junctions." *Applied physics letters* 104.11 (2014).
[194] Midya, Rivu, et al. "Artificial neural network (ANN) to spiking neural network (SNN) converters based on diffusive memristors." *Advanced Electronic Materials* 5.9 (2019): 1900060.
[195] Tavanaei, Amirhossein, et al. "Deep learning in spiking neural networks." *Neural networks* 111 (2019): 47-63.
[196] Bair, Wyeth, and Christof Koch. "Temporal precision of spike trains in extrastriate cortex of the behaving macaque monkey." *Neural computation* 8.6 (1996): 1185-1202.
[197] Gerstner, Wulfram, et al. Neuronal dynamics: From single neurons to networks and models of cognition. *Cambridge University Press*, 2014.
[198] Bohte, Sander M. "The evidence for neural information processing with precise spike-times: A survey." *Natural Computing* 3 (2004): 195-206.
[199] Bohte, Sander M., Han La Poutré, and Joost N. Kok. "Unsupervised clustering with spiking neurons by sparse temporal coding and multilayer RBF networks." *IEEE Transactions on neural networks* 13.2 (2002): 426-435.
[200] Thorpe, Simon J. "Spike arrival times: A highly efficient coding scheme for neural networks." *Parallel processing in neural systems* (1990): 91-94.
[201] Kayser, Christoph, et al. "Spike-phase coding boosts and stabilizes information carried by spatial and temporal spike patterns." *Neuron*61.4 (2009): 597-608.
[202] Hodgkin, Alan L., and Andrew F. Huxley. "A quantitative description of membrane current and its application to conduction and excitation in nerve." *The Journal of physiology* 117.4 (1952): 500.
[203] Izhikevich, Eugene M. "Simple model of spiking neurons." *IEEE Transactions on neural networks*14.6 (2003): 1569-1572.

[204] Stone, James V. "Principles of neural information theory." *Computational Neuroscience and Metabolic Efficiency* (2018).
[205] Pfeiffer, Michael, and Thomas Pfeil. "Deep learning with spiking neurons: Opportunities and challenges." *Frontiers in neuroscience* 12 (2018): 774.
[206] Kasabov, Nikola K. Time-space, spiking neural networks and brain-inspired artificial intelligence. Berlin, Heidelberg: *Springer Berlin Heidelberg*, 2019.
[207] Escobar, Maria-Jose, et al. "Action recognition using a bio-inspired feedforward spiking network." *International journal of computer vision*82 (2009): 284-301.
[208] Gupta, Ankur, and Lyle N. Long. "Character recognition using spiking neural networks." *2007 International Joint Conference on Neural Networks*. IEEE, 2007.
[209] Meftah, Boudjelal, Olivier Lezoray, and Abdelkader Benyettou. "Segmentation and edge detection based on spiking neural network model." Neural Processing Letters 32 (2010): 131-146.
[210] Kröger, BERND J., et al. "Phonetotopy within a neurocomputational model of speech production and speech acquisition." Some aspects of speech and the brain (2009): 59-90.
[211] Wade, John J., et al. "SWAT: A spiking neural network training algorithm for classification problems." IEEE Transactions on neural networks 21.11 (2010): 1817-1830.
[212] Ghosh-Dastidar, Samanwoy, and Hojjat Adeli. "Improved spiking neural networks for EEG classification and epilepsy and seizure detection." Integrated Computer-Aided Engineering 14.3 (2007): 187-212.
[213] Kasabov, Nikola, et al. "Evolving spiking neural networks for personalised modelling, classification and prediction of spatio-temporal patterns with a case study on stroke." Neurocomputing 134 (2014): 269-279.
[214] Huh, Dongsung, and Terrence J. Sejnowski. "Gradient descent for spiking neural networks." Advances in neural information processing systems 31 (2018).
[215] Caporale, Natalia, and Yang Dan. "Spike timing–dependent plasticity: a Hebbian learning rule." Annu. Rev. *Neurosci*. 31 (2008): 25-46.
[216] Saxena, Vishal, et al. "Towards neuromorphic learning machines using emerging memory devices with brain-like energy efficiency." *Journal of Low Power Electronics and Applications* 8.4 (2018): 34.
[217] Brunel, Nicolas, and Mark CW Van Rossum. "Lapicque's 1907 paper: from frogs to integrate-and-fire." *Biological cybernetics* 97.5-6 (2007): 337-339.
[218] Gerstner, Wulfram, and Werner M. Kistler. Spiking neuron models: Single neurons, populations, plasticity. *Cambridge university press*, 2002.
[219] Adrian, Edgar D. "The impulses produced by sensory nerve endings: Part I." *The Journal of physiology* 61.1 (1926): 49.
[220] Adrian, Edgar Douglas. "The basis of sensation." (1928).
[221] Buzsáki, Gyorgy, et al., eds. Temporal coding in the brain. *Springer Science & Business Media*, 2012.
[222] Gooler, David M., and Albert S. Feng. "Temporal coding in the frog auditory midbrain: the influence of duration and rise-fall time on the processing of complex amplitude-modulated stimuli." *Journal of Neurophysiology* 67.1 (1992): 1-22.

[223] AP, GEORGOPOULOS. "Neuronal population coding of movement direction." *Science* 233 (1986): 1416-1419.
[224] Park, Seongsik, Dongjin Lee, and Sungroh Yoon. "Noise-robust deep spiking neural networks with temporal information." *2021 58th ACM/IEEE Design Automation Conference (DAC)*. IEEE, 2021.
[225] Jiang, Chunming, and Yilei Zhang. "A Noise-Based Novel Strategy for Faster SNN Training." *Neural Computation* 35.9 (2023): 1593-1608.
[226] Schneidman, Elad, Barry Freedman, and Idan Segev. "Ion channel stochasticity may be critical in determining the reliability and precision of spike timing." Neural computation 10.7 (1998): 1679-1703.
[227] Manwani, Amit, and Christof Koch. "Detecting and estimating signals in noisy cable structures, I: Neuronal noise sources." Neural computation11.8 (1999): 1797-1829.
[228] Hessler, Neal A., Aneil M. Shirke, and Roberto Malinow. "The probability of transmitter release at a mammalian central synapse." Nature366.6455 (1993): 569-572.
[229] Bohte, Sander M., Joost N. Kok, and Han La Poutre. "Error-backpropagation in temporally encoded networks of spiking neurons." Neurocomputing 48.1-4 (2002): 17-37.
[230] McKennoch, Sam, Dingding Liu, and Linda G. Bushnell. "Fast modifications of the spikeprop algorithm." The 2006 IEEE International Joint Conference on Neural Network Proceedings. IEEE, 2006.
[231] Hamilton, Alister, and Leslie S. Smith. Neuromorphic Systems: Engineering Silicon From Neurobiology. Vol. 10. World Scientific, 1998.
[232] Stromatias, Evangelos, and John S. Marsland. "Supervised learning in spiking neural networks with limited precision: Snn/lp." 2015 International Joint Conference on Neural Networks (IJCNN). IEEE, 2015.
[233] Lee, Jun Haeng, Tobi Delbruck, and Michael Pfeiffer. "Training deep spiking neural networks using backpropagation." Frontiers in neuroscience 10 (2016): 508.
[234] Querlioz, Damien, et al. "Immunity to device variations in a spiking neural network with memristive nanodevices." IEEE transactions on nanotechnology 12.3 (2013): 288-295.
[235] Diehl, Peter U., and Matthew Cook. "Unsupervised learning of digit recognition using spike-timing-dependent plasticity." *Frontiers in computational neuroscience* 9 (2015): 99.
[236] Hebb, Donald Olding. "The organization of behavior: A neuropsychological theory. " *Psychology press*, 2005.
[237] Sejnowski, Terrence J., and Gerald Tesauro. "The Hebb rule for synaptic plasticity: algorithms and implementations." *Neural models of plasticity*. Academic Press, 1989. 94-103.
[238] Kohonen, Teuvo. Self-organization and associative memory. Vol. 8. *Springer Science & Business Media*, 2012.

[239] King, Charles, et al. "Hebbian modification of a hippocampal population pattern in the rat." *The Journal of physiology* 521.Pt 1 (1999): 159.
[240] Kistler, Werner M., and J. Leo van Hemmen. "Modeling synaptic plasticity in conjunction with the timing of pre-and postsynaptic action potentials." *Neural Computation* 12.2 (2000): 385-405.
[241] Brader, Joseph M., Walter Senn, and Stefano Fusi. "Learning real-world stimuli in a neural network with spike-driven synaptic dynamics." *Neural computation* 19.11 (2007): 2881-2912.
[242] Kheradpisheh, Saeed Reza, et al. "STDP-based spiking deep convolutional neural networks for object recognition." *Neural Networks* 99 (2018): 56-67.
[243] Fu, Qiang, and Hongbin Dong. "An ensemble unsupervised spiking neural network for objective recognition." *Neurocomputing* 419 (2021): 47-58.
[244] Srinivasan, Gopalakrishnan, Abhronil Sengupta, and Kaushik Roy. "Magnetic tunnel junction based long-term short-term stochastic synapse for a spiking neural network with on-chip STDP learning." *Scientific reports* 6.1 (2016): 29545.
[245] Lv, Wenxing, et al. "Stochastic artificial synapses based on nanoscale magnetic tunnel junction for neuromorphic applications." *Applied Physics Letters* 121.23 (2022).
[246] Jaiswal, Akhilesh, et al. "Proposal for a leaky-integrate-fire spiking neuron based on magnetoelectric switching of ferromagnets." *IEEE Transactions on Electron Devices* 64.4 (2017): 1818-1824.
[247] Liyanagedera, Chamika M., et al. "Stochastic spiking neural networks enabled by magnetic tunnel junctions: From nontelegraphic to telegraphic switching regimes." *Physical Review Applied* 8.6 (2017): 064017.
[248] Zink, Brandon R., Yang Lv, and Jian-Ping Wang. "Telegraphic switching signals by magnet tunnel junctions for neural spiking signals with high information capacity." *Journal of Applied Physics*124.15 (2018).
[249] Yang, Qu, et al. "Spintronic Integrate-Fire-Reset Neuron with Stochasticity for Neuromorphic Computing." *Nano Letters* 22.21 (2022): 8437-8444.
[250] Zeng, Zhongming, et al. "Ultralow-current-density and bias-field-free spin-transfer nano-oscillator." *Scientific reports* 3.1 (2013): 1426.
[251] Finocchio, G., et al. "Micromagnetic understanding of stochastic resonance driven by spin-transfer-torque." *Physical Review B* 83.13 (2011): 134402.
[252] Zeng, Z. M., et al. "Nanoscale magnetic tunnel junction sensors with perpendicular anisotropy sensing layer." *Applied Physics Letters* 101.6 (2012).
[253] Zeng, Zhongming, Giovanni Finocchio, and Hongwen Jiang. "Spin transfer nano-oscillators." *Nanoscale* 5.6 (2013): 2219-2231.
[254] Tomasello, R., et al. "Origin of temperature and field dependence of magnetic skyrmion size in ultrathin nanodots." *Physical Review* B 97.6 (2018): 060402.
[255] Shang, Chang He, et al. "Temperature dependence of magnetoresistance and surface magnetization in ferromagnetic tunnel junctions." *Physical Review B* 58.6 (1998): R2917.
[256] Davis, A. H., J. M. MacLaren, and P. LeClair. "Inherent temperature effects in magnetic tunnel junctions." *Journal of Applied Physics* 89.11 (2001): 7567-7569.

[257] Brown Jr, William Fuller. "Thermal fluctuations of a single-domain particle." *Physical review* 130.5 (1963): 1677.
[258] Hamadeh, A., et al. "Autonomous and forced dynamics in a spin-transfer nano-oscillator: Quantitative magnetic-resonance force microscopy." *Physical Review B* 85.14 (2012): 140408.
[259] Koch, Giacomo, et al. "Hebbian and anti-Hebbian spike-timing-dependent plasticity of human cortico-cortical connections." *Journal of Neuroscience* 33.23 (2013): 9725-9733.